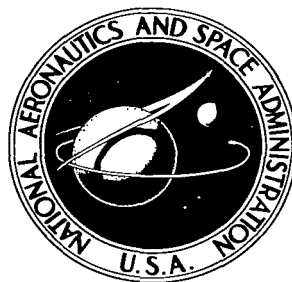


NASA TECHNICAL NOTE



NASA TN D-3804

C.1



LOAN COPY
AFWL (C) 11
KIRTLAND AFB, N.M.

NASA TN D-3804

INVESTIGATION OF TURBULENT SEPARATED FLOWS IN THE VICINITY OF FIN-TYPE PROTUBERANCES AT SUPERSONIC MACH NUMBERS

by Earl A. Price, Jr., and Robert L. Stallings, Jr.

Langley Research Center

Langley Station, Hampton, Va.



INVESTIGATION OF TURBULENT SEPARATED FLOWS IN THE VICINITY
OF FIN-TYPE PROTUBERANCES AT SUPERSONIC MACH NUMBERS

By Earl A. Price, Jr., and Robert L. Stallings, Jr.

Langley Research Center
Langley Station, Hampton, Va.

NATIONAL AERONAUTICS AND SPACE ADMINISTRATION

For sale by the Clearinghouse for Federal Scientific and Technical Information
Springfield, Virginia 22151 - Price \$2.50

INVESTIGATION OF TURBULENT SEPARATED FLOWS IN THE VICINITY
OF FIN-TYPE PROTUBERANCES AT SUPERSONIC MACH NUMBERS*

By Earl A. Price, Jr., and Robert L. Stallings, Jr.
Langley Research Center

SUMMARY

An experimental investigation has been conducted on the separated and associated disturbed flow region resulting from the presence of a fin-type protuberance in a turbulent boundary layer approximately 15.24 cm thick. Results were primarily obtained from pressure measurements over a Mach number range from 2.3 to 4.44 and Reynolds numbers per meter from 4.9×10^6 to 14.7×10^6 . The thickness, sweep, and height of the fin-type protuberances were varied.

Increasing the sweep of the protuberance was found to decrease sharply the upstream extent of disturbed flow. The extent of the upstream disturbed flow increased linearly with protuberance diameter. The disturbed flow region did not vary significantly in size as model height was varied from greater than boundary-layer thickness to only a fraction of the boundary-layer thickness. The first peak pressure coefficient was found to be significantly lower than values from two-dimensional separated flow. An irregular pressure distribution was found along that portion of the protuberance leading edge submerged within the boundary layer for certain models. Both the first peak and final peak pressure ratios increased with increasing Mach number for any given model. Varying the free-stream Reynolds number by a factor of three had no effect on the extent of upstream disturbed flow.

INTRODUCTION

The phenomenon of boundary-layer separation has been of considerable concern to the aerodynamicist throughout the history of aviation. Separation associated with such common devices as ailerons, flaps, and spoilers led to numerous experimental investigations and analytical studies to provide quantitative information pertaining to the flow variables within the separation region. The occurrence on flight vehicles of these two-dimensional objects plus the simplicity of

*The information presented herein was included in a thesis submitted by Earl A. Price, Jr., in partial fulfillment of the requirements for the degree of Master of Aerospace Engineering, University of Virginia, Charlottesville, Virginia, June 1966.

the two-dimensional flow field (compared with the three-dimensional flow field) has led most investigators to limit their studies to separation forced by two-dimensional objects. Extensive experimental information for the two-dimensional flow field has been obtained for both laminar and turbulent boundary layers up through the supersonic and low hypersonic Mach number region. Representative of the experimental work done on two-dimensional separation is that presented in references 1 to 4. The difficulties of describing two-dimensional turbulent separated flow theoretically are well known. The effort that has gone into the problem has produced some quasi-theoretical work (ref. 5, for example), which in terms of practical usefulness, has met with only moderate success.

The more complicated three-dimensional flow fields resulting from separation forced by simple protuberances have received little detailed study. Information pertaining to the three-dimensional separation phenomenon is of importance in determining not only the aerodynamic loads but also the aerodynamic heating in these regions. In fact, it is for the latter reason that most investigations on three-dimensional separation have been conducted. References 6 and 7 present aerodynamic heating data for three-dimensional turbulent separated regions in supersonic flow. These data are useful in defining the extent of the model effect and the magnitude of heating rates within the region for the specific configurations. Reference 6 also presents a number of excellent oil flow photographs of the separated region upstream of a variety of three-dimensional protuberances. A limited amount of pressure data is also presented in reference 6. A comparison is made in reference 8 of the pressure distributions in the regions of separation forced by two-dimensional steps and vertical three-dimensional protuberances of the same height. In view of this lack of information on separation forced by three-dimensional objects, the present tests were designed to gain some insight into the effect of protuberance geometry, Mach number, and Reynolds number on the extent and fluid properties of the separation region. In order to accomplish this, detailed static pressure distributions were obtained in the separated and associated disturbed flow region caused by the presence in the flow of a three-dimensional protuberance. To maintain the geometry of the model as simple as possible and yet have a basis for practical application, a fin-type model with a cylindrical leading edge was chosen. The fin thickness, sweep, and height were systematically varied in order to determine the effects of these basic geometric variables on the separation and disturbed flow regions. The free-stream Mach number was varied from 2.30 to 4.44 and the free-stream Reynolds number from 4.9×10^6 per meter to 14.7×10^6 per meter. The models were mounted on the tunnel access door flush with the tunnel sidewall. In this manner, the tunnel sidewall turbulent boundary layer (approximately 15.24 cm thick) was utilized to simulate the relatively thick boundary layers found over a large portion of most full-scale vehicles.

SYMBOLS

C_p pressure coefficient, $\frac{p - p_\infty}{q_\infty}$

d diameter of cylindrical leading edge of model, centimeters

h	height of model, centimeters
M	Mach number
p	pressure, newtons per centimeter ²
$p_{t,2}$	stagnation pressure behind normal shock, newtons per centimeter ²
q	dynamic pressure, newtons per centimeter ²
R	Reynolds number per meter
x	streamwise coordinate of plate measured from leading edge of model, centimeters (see fig. 4)
y	coordinate in plane of plate perpendicular to streamwise plate center line, centimeters (see fig. 4)
z	perpendicular distance from plate, centimeters (see fig. 2)
δ	boundary-layer thickness, centimeters
θ	meridian angle, degrees (see fig. 2)
Λ	sweep angle, degrees (see fig. 2)

Subscripts:

∞	free-stream conditions
l	local conditions
p	condition in region of first peak pressure

APPARATUS

Wind Tunnel

This investigation was conducted in the high Mach number test section of the Langley Unitary Plan wind tunnel. The locations of the basic elements of this facility are shown in figure 1. This is a continuous flow, variable-pressure tunnel with a 121.9- by 121.9-cm test section. The Mach number can be varied from 2.30 to 4.65 by means of an asymmetric sliding-block nozzle. A detailed description of the facility is given in reference 9.

Models

A total of 14 fin-type models with cylindrical leading edges were tested. A sketch showing the basic geometry of the models is presented as figure 2.

Each model had a constant thickness equal to the leading-edge diameter. Reference will be made throughout this paper to diameter rather than thickness. Table I presents the geometric parameters of each model. Leading-edge diameter was varied from 1.47 to 8.89 cm, sweep from 0° to 75° , and model height from 2.54 to 25.40 cm. Photographs of the models, grouped in such a way that only one of the geometric parameters is varied, are presented in figure 3. Models 1 and 2 were constructed of steel, model 12 was constructed of aluminum, and all other models were constructed of mahogany. Pressure orifices were installed on all the models except model 3. The locations of the orifices are given in table II. The orifices were formed by installing monel tubing flush with the model surface; this tubing had an inside diameter of 0.102 cm and an outside diameter of 0.152 cm. Each model was mounted on a circular plate containing 180 orifices which were formed by installing monel tubing flush with the plate surface; this tubing had an inside diameter of 0.127 cm and an outside diameter of 0.173 cm. The circular plate was designed to fit flush with the steel tunnel access door. The relative location of the orifices may be seen in figure 4. A photograph of model 13 mounted on the test plate and tunnel door is presented in figure 5.

Pressure Recording System

The pressures were recorded by using five 48-channel pressure sampling valves. Each valve sequentially transmits each channel of pressure information to a single electrical pressure transducer. This electrical information is fed to a strip chart recorder and an analog to digital converter. The data in digital form are then recorded on punch cards suitable for machine computation of final data. The tunnel stagnation pressure was measured on a precision mercury manometer. To determine p_∞ and $p_{t,2}$ the stagnation pressure and nominal free-stream Mach number were used.

Shadowgraph System

Previous investigators have found schlieren and/or shadowgraph pictures to be useful in analyzing results of separation studies. The present tests were conducted with the models mounted on a steel door which replaced the regular schlieren door. This arrangement prevented use of the regular tunnel schlieren flow visualization system. A special system for obtaining shadowgraph pictures was, therefore, devised and used to obtain a limited number of photographs. A sketch showing the basic components of the system is presented as figure 6. The flat mirrors were 30.48 cm by 40.64 cm in size and were mounted flush with the surface of a 45° triangular steel bracket which was bolted to the steel tunnel door. The brackets had sharp leading edges with the mirror side parallel to the flow. The mirrors and bracket can be seen in the model installation photograph (fig. 5). The mirrors used outside the test section were 30.5-cm-diameter concave mirrors having a focal length of 182.9 cm. Photographs were taken with a 70-mm camera at slow shutter speeds. High-speed motion pictures were also taken at 2,000 frames/sec with a 16-mm camera. The light source was a 25-W zirconium concentrated arc lamp.

TEST CONDITIONS

This investigation was conducted at Mach numbers of 2.3, 2.98, 3.71, and 4.44. With the tunnel block set to provide a given Mach number in the test section, the total pressure was varied to obtain Reynolds numbers per meter of approximately 4.9×10^6 , 9.8×10^6 , and 14.7×10^6 . The tunnel total temperature was held constant at approximately 339° K for the test at the three lower Mach numbers and 353° K for the test at the highest Mach number.

ACCURACY

Accuracy of the pressure sampling valves is better than 1 percent of the full-scale range of the gage; this includes all errors of linearity, hysteresis, and repeatability. Previous tests in this tunnel on separate days have shown that 85 percent of the data is repeatable to better than 0.5 percent. Gages having a maximum range of 5.17 N/cm^2 (7.5 lb/in^2) and 10.34 N/cm^2 (15 lb/in^2) were used for the plate and models, respectively. These gages were selected to accommodate the highest pressures expected. Because a wide range of pressures were encountered over the range of Mach numbers and Reynolds numbers of this investigation, no single accuracy can be given in terms of p_l/p_∞ or $p_l/p_{t,2}$. A 0.5-percent error in the full-scale gage reading could give errors in p_l/p_∞ that range from ± 0.03 for $M_\infty = 2.30$, $R_\infty = 9.8 \times 10^6$ to ± 0.41 for $M_\infty = 4.44$, $R_\infty = 4.9 \times 10^6$ and errors in $p_l/p_{t,2}$ that range from ± 0.006 for $M_\infty = 2.98$, $R_\infty = 14.7 \times 10^6$ to ± 0.032 for $M_\infty = 4.44$, $R_\infty = 4.9 \times 10^6$. The accuracy of the precision mercury manometer on which the stagnation pressure was measured is 0.0024 N/cm^2 (0.5 lb/ft^2).

The results of the test section calibration indicate the following accuracies for the free-stream Mach numbers of this investigation:

M_∞	$\pm \Delta M_\infty$
2.30	0.02
2.98	.02
3.71	.06
4.44	.06

PRESENTATION OF RESULTS

The results are presented in the following figures:

	Figure
Schematic drawing of a typical interaction for a two-dimensional step . .	7
Effect of sweep on the pressure distribution upstream of models.	
$R_\infty \approx 9.8 \times 10^6$	
$d = 5.08$ cm	8(a)
$d = 8.89$ cm	8(b)
Effect of diameter on the pressure distribution upstream of models.	
$h = 25.40$ cm; $R_\infty \approx 9.8 \times 10^6$	
$\Lambda = 12.9^\circ$	9(a)
$\Lambda = 30^\circ$	9(b)
Variation of the separation distance and the disturbed flow region with	
protuberance diameter. $\delta \approx 15.24$ cm; $R_\infty \approx 9.8 \times 10^6$	10
Effect of model height on the upstream distribution. $d = 5.08$ cm;	
$\Lambda = 30^\circ$; $R_\infty \approx 9.8 \times 10^6$	11
Effect of Mach number on the pressure distribution upstream of models.	
$R_\infty \approx 9.8 \times 10^6$	
Model 8; $\Lambda = 0^\circ$; $d = 5.08$ cm; $h = 25.40$ cm	12(a)
Model 9; $\Lambda = 12.9^\circ$; $d = 5.08$ cm; $h = 25.40$ cm	12(b)
Model 7; $\Lambda = 30^\circ$; $d = 5.08$ cm; $h = 25.40$ cm	12(c)
Model 10; $\Lambda = 45^\circ$; $d = 5.08$ cm; $h = 25.40$ cm	12(d)
Model 11; $\Lambda = 60^\circ$; $d = 5.08$ cm; $h = 25.40$ cm	12(e)
Model 12; $\Lambda = 75^\circ$; $d = 5.08$ cm; $h = 15.24$ cm	12(f)
Model 1; $\Lambda = 12.9^\circ$; $d = 1.47$ cm; $h = 25.40$ cm	12(g)
Model 2; $\Lambda = 12.9^\circ$; $d = 1.91$ cm; $h = 25.40$ cm	12(h)
Model 13; $\Lambda = 12.9^\circ$; $d = 8.89$ cm; $h = 25.40$ cm	12(i)
Model 14; $\Lambda = 30^\circ$; $d = 8.89$ cm; $h = 25.40$ cm	12(j)
Effect of Reynolds number on the pressure distribution upstream of	
models. $h = 25.40$ cm	
Model 2; $d = 1.91$ cm; $\Lambda = 12.9^\circ$	13(a)
Model 7; $d = 5.08$ cm; $\Lambda = 30^\circ$	13(b)
Model 9; $d = 5.08$ cm; $\Lambda = 12.9^\circ$	13(c)
Model 13; $d = 8.89$ cm, $\Lambda = 12.9^\circ$	13(d)
Variation of first peak pressure coefficient with Mach number	14
Pressure distribution (p_l/p_∞) in the vicinity of model 8.	
$d = 5.08$ cm; $h = 25.40$ cm; $\Lambda = 0^\circ$; $M_\infty = 4.44$; $R_\infty = 9.5 \times 10^6$. . .	15
Pressure distribution (p_l/p_∞) in the vicinity of model 9.	
$d = 5.08$ cm; $h = 25.40$ cm; $\Lambda = 12.9^\circ$; $M_\infty = 4.44$; $R_\infty = 9.5 \times 10^6$. .	16
Pressure distribution (p_l/p_∞) in the vicinity of model 7.	
$d = 5.08$ cm; $h = 25.40$ cm; $\Lambda = 30^\circ$; $M_\infty = 4.44$; $R_\infty = 9.5 \times 10^6$. . .	17
Pressure distribution (p_l/p_∞) in the vicinity of model 10.	
$d = 5.08$ cm; $h = 25.40$ cm; $\Lambda = 45^\circ$; $M_\infty = 4.44$; $R_\infty = 9.5 \times 10^6$. . .	18

Pressure distribution (p_l/p_∞) in the vicinity of model 11.	
$d = 5.08$ cm; $h = 25.40$ cm; $\Lambda = 60^\circ$; $M_\infty = 4.44$; $R_\infty = 9.5 \times 10^6$. . .	19
Pressure distribution (p_l/p_∞) in the vicinity of model 12.	
$d = 5.08$ cm; $h = 15.24$ cm; $\Lambda = 75^\circ$; $M_\infty = 4.44$; $R_\infty = 9.4 \times 10^6$. . .	20
Pressure distribution (p_l/p_∞) in the vicinity of model 1.	
$d = 1.47$ cm; $h = 25.40$ cm; $\Lambda = 12.9^\circ$; $M_\infty = 4.44$; $R_\infty = 14.2 \times 10^6$.	21
Pressure distribution (p_l/p_∞) in the vicinity of model 2.	
$d = 1.91$ cm; $h = 25.40$ cm; $\Lambda = 12.9^\circ$; $M_\infty = 4.44$; $R_\infty = 9.5 \times 10^6$. .	22
Pressure distribution (p_l/p_∞) in the vicinity of model 13.	
$d = 8.89$ cm; $h = 25.40$ cm; $\Lambda = 12.9^\circ$; $M_\infty = 4.44$; $R_\infty = 9.5 \times 10^6$. .	23
Pressure distribution (p_l/p_∞) in the vicinity of model 14.	
$d = 8.89$ cm; $h = 25.40$ cm; $\Lambda = 30^\circ$; $M_\infty = 4.44$; $R_\infty = 9.5 \times 10^6$. . .	24
Pressure distribution (p_l/p_∞) in the vicinity of model 3.	
$d = 5.08$ cm; $h = 2.54$ cm; $\Lambda = 30^\circ$; $M_\infty = 4.44$; $R_\infty = 9.5 \times 10^6$. . .	25
Pressure distribution (p_l/p_∞) in the vicinity of model 4.	
$d = 5.08$ cm; $h = 5.08$ cm; $\Lambda = 30^\circ$; $M_\infty = 4.44$; $R_\infty = 9.5 \times 10^6$. . .	26
Pressure distribution (p_l/p_∞) in the vicinity of model 5.	
$d = 5.08$ cm; $h = 10.16$ cm; $\Lambda = 30^\circ$; $M_\infty = 4.44$; $R_\infty = 9.5 \times 10^6$. . .	27
Pressure distribution (p_l/p_∞) in the vicinity of model 6.	
$d = 5.08$ cm; $h = 15.24$ cm; $\Lambda = 30^\circ$; $M_\infty = 4.44$; $R_\infty = 9.5 \times 10^6$. . .	28
Pressure distribution (p_l/p_∞) in the vicinity of model 9 for various	
Mach numbers. $d = 5.08$ cm; $h = 25.40$ cm; $\Lambda = 12.9^\circ$; $R_\infty \approx 9.8 \times 10^6$	
$M_\infty = 2.30$	29(a)
$M_\infty = 2.98$	29(b)
$M_\infty = 3.71$	29(c)
Pressure distribution (p_l/p_∞) in the vicinity of model 9 for various	
Reynolds numbers. $d = 5.08$ cm; $h = 25.40$ cm; $\Lambda = 12.9^\circ$; $M_\infty = 4.44$	
$R_\infty = 4.7 \times 10^6$	30(a)
$R_\infty = 14.2 \times 10^6$	30(b)
Comparison of the extent of disturbed flow for various models.	
$M_\infty = 4.44$; $R_\infty = 9.8 \times 10^6$	
Variation with sweep for $d = 5.08$ cm	31(a)
Variation with diameter for $\Lambda = 12.9^\circ$	31(b)
Variation with diameter for $\Lambda = 30^\circ$	31(c)
Shadowgraph of the interaction region for model 8.	
$M_\infty = 2.98$; $R_\infty \approx 9.8 \times 10^6$	32
Tuft study on model 13. $M_\infty = 3.71$; $R_\infty \approx 9.8 \times 10^6$	33
Effect of sweep on the model stagnation line pressure distribution.	
$R_\infty \approx 9.8 \times 10^6$; $d = 5.08$ cm	
$M_\infty = 2.30$	34(a)
$M_\infty = 2.98$	34(b)

	Figure
$M_\infty = 3.71$	34(c)
$M_\infty = 4.44$	34(d)
Effect of model height on the model stagnation line pressure distribution. $\Lambda = 30^\circ$; $d = 5.08$ cm; $R_\infty \approx 9.8 \times 10^6$	
$M_\infty = 3.71$	35(a)
$M_\infty = 4.44$	35(b)
Effect of Mach number on the model stagnation line pressure distribution. $\Lambda = 12.9^\circ$; $h = 25.40$ cm; $R_\infty \approx 9.8 \times 10^6$	
Model 1; $d = 1.47$ cm	36(a)
Model 2; $d = 1.91$ cm	36(b)
Model 9; $d = 5.08$ cm	36(c)
Model 13; $d = 8.89$ cm	36(d)
Effect of Reynolds number on the stagnation line pressure distribution of model 9. $\Lambda = 12.9^\circ$; $d = 5.08$ cm; $h = 25.40$ cm	
$M_\infty = 2.98$	37(a)
$M_\infty = 4.44$	37(b)
Pressure distributions around the model leading edge for various values of sweep. $d = 5.08$ cm; $M_\infty = 4.44$; $R_\infty \approx 9.8 \times 10^6$	
Model 8; $\Lambda = 0^\circ$; $h = 25.40$ cm	38(a)
Model 9; $\Lambda = 12.9^\circ$; $h = 25.40$ cm	38(b)
Model 7; $\Lambda = 30^\circ$; $h = 25.40$ cm	38(c)
Model 10; $\Lambda = 45^\circ$; $h = 25.40$ cm	38(d)
Model 11; $\Lambda = 60^\circ$; $h = 25.40$ cm	38(e)
Model 12; $\Lambda = 75^\circ$; $h = 15.24$ cm	38(f)
Effect of diameter on the pressure distribution around the model leading edge. $\Lambda = 12.9^\circ$; $h = 25.40$ cm; $R_\infty \approx 9.8 \times 10^6$; $M_\infty = 4.44$	
$z/\delta = 0.5$ at $\theta = 0^\circ$	39(a)
$z/\delta = 1.00$ at $\theta = 0^\circ$	39(b)
$z/\delta = 1.33$ at $\theta = 0^\circ$	39(c)
Effect of Mach number on the pressure distribution around the leading edge of model 9. $\Lambda = 12.9^\circ$; $d = 5.08$ cm; $h = 25.40$ cm; $R_\infty \approx 9.8 \times 10^6$	
$z/\delta = 0.5$ at $\theta = 0^\circ$	40(a)
$z/\delta = 1.00$ at $\theta = 0^\circ$	40(b)
$z/\delta = 1.33$ at $\theta = 0^\circ$	40(c)

RESULTS AND DISCUSSION

Plate Center Line Distributions

The general shape of the pressure distribution curve upstream of a forward-facing step in a turbulent boundary layer has been established satisfactorily. Presented in figure 7 is a schematic drawing of a typical interaction for a step along with the corresponding pressure distribution. Although the exact shape varies considerably with various step heights, boundary-layer thicknesses, and local flow properties, the distribution generally consists of a sudden increase

in the pressure to a peak value - normally called the first peak pressure - a leveling off and a possible dip in the level of pressure and, finally, a sharp increase to a maximum pressure at the upstream edge of the step. The location at which separation actually occurs lies somewhere between the initial increase in pressure and the first peak and has been determined by various means by different investigators. No attempt was made during this investigation to determine the exact location of separation. For this reason, reference is made throughout the present report to the disturbed flow region - that is, the entire region affected by the models - rather than the separation region only.

For three-dimensional protuberances the upstream extent of the model effect has been found to vary with diameter (ref. 7). A comparison of the three-dimensional results of references 6 and 8 with the results from two-dimensional steps (refs. 1 to 4) indicates, however, that the shape of the pressure distribution curve is similar for the two cases, with perhaps a more pronounced dip and a higher pressure at the upstream edge of the three-dimensional protuberance. Results of reference 8 indicate that in comparing two-dimensional steps and three-dimensional protuberances of the same height, the extent of the disturbed flow region is significantly less for the three-dimensional objects. This decrease is attributed to the lateral pressure relief and consequent circumferential flow around the three-dimensional object. The more pronounced dip in pressure for three-dimensional separation is probably also associated with these phenomena.

The effect of leading-edge sweep on the upstream pressure distribution along the center line is presented in figure 8 for the 5.08-cm- and 8.89-cm-diameter models. Data are presented in the form of plots of p_1/p_∞ against x/d where x is the upstream distance from the fin leading edge (fig. 4). As can be seen in figure 8(a) varying the sweep from 0° to 30° has a very pronounced effect on the extent of the upstream disturbed flow as well as the maximum pressure measured within the region (final peak). Only a very slight variation of the first-peak pressure was found for the same range of sweep. The extent of the upstream disturbed flow continued to decrease with increasing sweep, but at a more modest rate, until at $\Lambda = 75^\circ$ the effect of the model was barely perceptible. Similarly, the maximum pressure decreased with increasing sweep. For sweep angles of 45° and greater, no definite first peak pressure could be determined. Since separation of a turbulent boundary layer is characterized by such a peak, it was not established whether separation actually occurred. It should be noted that all models from which data presented in this figure were obtained were 25.40 cm high except for model 12 which was 15.24 cm high. Based on data shown subsequently on the effect of model height this difference in model height should not have any effect on the upstream pressure distribution. The decrease in the final peak pressure with sweep is as expected since this was located at the model leading edge and would, therefore, decrease as the model leading-edge pressure decreased. Similar trends in the overall pressure distribution were obtained for both Mach numbers presented. The same trends are shown in figure 8(b) for $d = 8.89$ cm at the two sweep angles available.

The effect of leading-edge diameter on the upstream pressure distribution for $\Lambda = 12.9^\circ$ is presented in figure 9(a) for $M_\infty = 2.98$ and 4.44. Although

the extent of the disturbed flow region varies considerably in terms of x for the different diameters, it correlates very well when presented plotted against x/d . The shape of the distribution for each model is somewhat similar at $M_\infty = 2.98$. At $M_\infty = 4.44$ the distributions are considerably different, however, especially for the two small diameter models. For both Mach numbers, the final peak pressure increases with increasing diameter; this is believed to be due to the fact that the smaller physical size of the separated region for the small models would not sustain a pressure gradient of the magnitude required to bring the pressure up to the value of the larger models. Presented in figure 9(b) is the effect of diameter on the upstream distribution for $\Lambda = 30^\circ$. Models were only constructed at this sweep angle for the two largest diameters. Excellent correlation was obtained for both Mach numbers at all locations except immediately upstream of the leading edge, where again an increase in the final peak pressure was obtained with increasing diameter.

Presented in figure 10 is the variation of the separation distance (from other experiments) and the disturbed flow region with protuberance diameter. All data were obtained at $R_\infty \approx 9.8 \times 10^6$ with $\delta \approx 15.24$ cm. Data shown for $d = 7.112$ cm were obtained from reference 6. Separation data for $\Lambda = 12.9^\circ$ were obtained from reference 7. All separation data were obtained from oil flow photographs. The data from references 6 and 7 were at $M_\infty = 3.51$ whereas those from the present investigation were obtained at $M_\infty = 3.71$. Based on data shown subsequently concerning the effect of Mach number, this Mach number difference is believed to have no significant effect on the results shown in figure 10. For $\Lambda = 12.9^\circ$ where the most data are available, it appears that both the separation and disturbed flow regions vary linearly with diameter. Straight lines were, therefore, drawn through the data for each of the other sweep angles. As diameter is increased beyond that of the present investigation, the variation would, of course, at some point cease to be linear and approach asymptotically, the two-dimensional step or wedge value.

The effect of model height on the upstream pressure distribution is presented in figure 11. Data were obtained on models having 30° sweep and 5.08-cm diameters for five different heights. The extent of the upstream effect appears to be invariant with model height. In fact, very little effect of model height is shown at all except at the instrumentation location adjacent to the model leading edge. A wide variation in results was obtained at this location, although no trend with model height was established. The same type distribution did occur here, however, for both Mach numbers.

The effects of model height found in this investigation are significantly different from those found previously for two-dimensional steps (e.g., refs. 2 and 3) where the extent of upstream effect increases with model height and the first peak pressure increases with model height up to the boundary-layer thickness and then levels off for higher models. It was somewhat surprising that for the present investigation the effect of the model extended upstream as far for the models submerged within the boundary layer as for those protruding through the boundary layer. Just how short the model could be before significant effects of height would occur was not established. It is quite probable that the minimum model height at which effects first appear will vary with sweep.

The effect of Mach number on the pressure distribution upstream of all the models of this investigation, with the exception of those which were used to determine the effect of h/δ is presented in figure 12. Since there were no appreciable effects from varying h/δ , the Mach number effects shown for model 7 are representative of the effects for the shorter models. In comparing the data for the different models, three basic types of pressure distributions can be noted. First, for the models where separation is believed to occur (based on the characteristic shape of the pressure distribution for separated flow) and yet is limited to a relatively small region (models 1, 2, 7, 9, and 14), the pressure distributions for each Mach number are similar; yet their locations are shifted relative to one another. As an example of this shift, consider model 2 (fig. 12(h)) where the first influence of the model for $M_\infty = 2.30$ occurs at $\frac{x}{d} \approx 2.3$, whereas for $M_\infty = 4.44$ it has moved downstream to $\frac{x}{d} \approx 1.8$. A corresponding downstream shift with increasing Mach number is noted in the first peak pressure. The magnitude of the first peak pressure ratio increases with increasing Mach number as has been the observed trend for two-dimensional separated flow (ref. 4). The pressure dip appears to be less pronounced as Mach number is increased for models 1, 2, and 7 but relatively unchanged for models 9 and 14. The final peak pressure ratio on the plate surface increases with increasing Mach number. The second type distribution noted is where, due to model geometry, a larger region of separation occurred (models 8 and 13, figs. 12(a) and 12(i)). For these models, no shift is noted in the distributions as Mach number is varied. The first peak pressure increases with increasing Mach number which, as was noted for model 8, is the same trend found for two-dimensional separated flow. The final pressure peak is seen to increase sharply from the dip and then decrease at the instrumentation location adjacent to the model for all but the lowest Mach number. A logical explanation for this decrease is not immediately apparent. The third type distribution found was one where the pressure increased steadily to a maximum at the upstream edge of the model and no dip occurred (models 10, 11, and 12). Whether or not separation actually occurred for any of these models was not established.

The effect of Reynolds number on the pressure distribution upstream of various models is presented in figure 13. Data are presented at $M_\infty = 2.98$, 3.71, and 4.44 for free-stream Reynolds numbers per meter of approximately 4.9×10^6 , 9.8×10^6 , and 14.7×10^6 . The models presented in this figure were chosen so that the Reynolds number effect for disturbed flow regions of various sizes could be determined. For all models the effects of Reynolds number were a minimum for $M_\infty = 2.98$ and increase with increasing Mach number. Varying the Reynolds number had no effect on the extent of the upstream disturbed flow for any of the models. The magnitude of the first peak pressure was not materially affected except for model 2 at $M_\infty = 4.44$ and $R_\infty = 4.9 \times 10^6$ where the occurrence of a peak could not be determined from the data. For model 9 the distribution appears to be skewed somewhat at the low Reynolds number and $M_\infty = 3.71$ and 4.44 with the first peak shifted downstream with a corresponding increase in the magnitude of the dip pressure. A similar trend was found for model 13 (fig. 13(d)) at $M_\infty = 4.44$. The pressure immediately upstream of the model leading edge increased with increasing Reynolds number for all models presented in figure 13.

First Peak Pressure Coefficient

Presented in figure 14 is the variation of the first peak pressure coefficient $C_{p,p}$ with Mach number for model 8. Also presented are data from reference 6 which were obtained with a 7.11-cm-diameter upright cylinder 31.75 cm in height. These data were obtained in the same facility as the present investigation and also in a 15.24-cm-thick boundary layer. Although the data were obtained approximately 1 diameter off the upstream center line, subsequent data (fig. 15) show that this has little, if any, effect on the magnitude of the data. An empirical equation which fits these data reasonably well is

$$C_{p,p} = \frac{0.682}{M_{\infty}^{1.44}}$$

Also presented in figure 14 are two empirical equations from reference 4 obtained from separation forced by two-dimensional objects over the Mach number range indicated for each. The data from which these equations were obtained were taken in relatively thin turbulent boundary layers ($\delta \approx 0.64$ cm). A direct comparison of the two- and three-dimensional data may be subject to question because of the difference in δ for the two sets of data. The effect of varying boundary-layer thickness by this magnitude is not known precisely but the data of reference 6 indicate that $C_{p,p}$ for three-dimensional separation decreases slightly with increasing boundary-layer thickness. The comparison is perhaps more meaningful if the triangular symbols are compared also. These data (from ref. 6) were obtained with a 10.16-cm-high by 60.96-cm-wide step also mounted on the sidewall of the same facility as in the present investigation. The fact that this model did not completely span the tunnel nor extend through the boundary layer would both tend to give lower results for $C_{p,p}$ than truly two-dimensional objects which extend through the boundary layer, although the magnitude of the difference is not known. In effect, therefore, the difference shown between the three-dimensional data and the triangular symbols would be a minimum difference anticipated between $C_{p,p}$ for two-dimensional and three-dimensional separation for relatively thick turbulent boundary layers.

Plate Spatial Distributions

Spatial plots of the pressure ratio p_t/p_{∞} obtained on the test plate in the vicinity of each of the models of this investigation are presented in figures 15 to 28 for $M_{\infty} = 4.44$ and $R \approx 9.8 \times 10^6$. Spatial plots for model 9 at the other Mach numbers and Reynolds numbers of this investigation are presented in figures 29 and 30, respectively. A line has been drawn on each plot illustrating the approximate extent of the effect of the model. Lack of instrumentation at certain locations necessitates a certain amount of arbitrariness as to where the line was drawn. It should be accurate enough, however, to determine basic trends. The effect of sweep on the spatial distributions can be determined by comparing figures 15 to 20. There is a decrease in the extent of

the disturbed flow region as well as the pressure ratio within the region with increasing sweep. A comparison of the extent of the disturbed flow region for models of different sweep angles is shown in figure 31(a).

The effect of fin diameter on the spatial distributions for $\Lambda = 12.9^\circ$ can be determined by comparing figures 21, 22, 16, and 23. The shape of the disturbed flow region appears to be similar for all four models for the region from $x = 0$ forward to the most upstream point. In general, the pressure ratios within the disturbed flow region increased with increasing diameter. A comparison of the overall extent of the model effects for the various diameters at $\Lambda = 12.9^\circ$ is shown in figure 31(b). The effect of fin diameter on the spatial distributions for $\Lambda = 30^\circ$ can be determined by comparing figures 17 and 24. As was found for $\Lambda = 12.9^\circ$, the shape of the region affected by the model forward of $x = 0$ appears to be similar for the two models. The extent of the entire region affected by these two models can be compared in figure 31(c).

The effect of varying model height for $d = 5.08$ cm and $\Lambda = 30^\circ$ can be determined by comparing figures 25 to 28, and 17. As was shown previously (fig. 11) the extent of the model effect along the upstream center line was independent of model height for the range of model heights of this investigation. Although a complete distribution was not obtained for a model height of 2.54 cm, it appears as though the extent of the model effect around and to the side was approximately the same for all model heights. A comparison of the magnitude of the pressure ratios indicates that, for the region upstream of the model leading edge, the ratios are approximately the same. There is a difference, however, in the pressure ratios downstream of the model leading edge. Pressure ratios approaching unity were measured over a large portion of the aft section of the plate for the 2.54-cm-high model (fig. 25). Apparently, the flow expansion over the top of the model spreads laterally and down to the plate surface; thus, the pressure is lowered in this region. This same trend was found for the 5.08-cm- and 10.16-cm-high models (figs. 26 and 27). The point at which the expansion reaches the plate moves downstream as model height is increased until for $h = 10.16$ cm only a small region adjacent to the model was affected. For the higher models, no such effects occurred within the instrumented region.

The effect of Mach number on the spatial distributions in the vicinity of model 9 can be obtained by comparing figure 16 with figure 29. There is an overall increase in the pressure ratio over the entire region affected by the model with increasing Mach number. This is the same trend shown in figure 12 for the distributions along the center line upstream of the model. In general, the effects move slightly downstream and wrap around closer to the model with increasing Mach number.

Comparison of the different Reynolds number data in the vicinity of model 9 at $M_\infty = 4.44$ can be made from figures 16 and 30. No significant effects of Reynolds number either on the magnitude of the pressures or the extent of the model effect could be determined.

Flow Visualization on Models

The special shadowgraph system described earlier was designed for the purpose of observing the shock formation in the interaction region of the model leading edge. An example of the photographs obtained by this method is shown in figure 32. For model 8, the major portion of the shock formation within the boundary layer was highly unsteady and, therefore, cannot be distinguished in the photograph which was taken at slow shutter speeds. However, high-speed motion pictures were taken at 2,000 frames/sec. Selected frames from the motion pictures were enlarged for analysis purposes but were not suitable for report reproduction. The location of the intersection of the model bow shock and the oblique shock from the separated region could be identified in certain cases from these. The investigators in references 1 and 2 found the shock formation from two-dimensional separation to be relatively steady. Although this method of obtaining shadowgraphs was successful, only a limited number of photographs were obtained due to a malfunction in the camera and the limited field of view of the system. It is believed, however, that a large number of quality photographs over a wide range of conditions could be obtained where a system of this nature is necessary using somewhat more refined components in the system.

An attempt was made to determine the direction of the flow along the model leading edge by using tufts. A special model 13 was constructed for this purpose. Five rows of tufts in 15° increments around the leading edge with the tufts 1.27 cm apart were installed on the model. The tufts were nylon strings approximately 1.27 cm in length. They were glued in small holes drilled in the model. Before a run the model leading edge and tufts were painted with oil containing a fluorescent dye. When flow was started in the tunnel, the oil on the wooden model washed off quite rapidly. However, enough oil and, consequently, fluorescent dye remained in the tufts to show up vividly under ultraviolet light. A photograph of the results is presented as figure 33. The relatively long exposure time for the picture prevented obtaining sharp pictures of the fluctuating tufts; however, the direction of the tufts and, consequently, the flow direction can be determined over much of the model. A sketch of the model leading edge showing the positions of the tufts based on photographs, as well as observations made during the test, is presented along with the photograph. The exact point on the stagnation line where flow reversal occurred could not be determined by this method, although it was in the same region as the peak pressure shown subsequently.

Model Pressure Distributions

The effect of sweep on the model leading-edge pressure distribution is shown in figure 34. Also presented by the symbols at $\frac{z}{\delta} = 0$ are the data obtained on the plate at $\frac{x}{d} = 0$. Data are presented for each Mach number along with a theoretical value calculated from modified Newtonian theory for free-stream conditions. In general, the agreement between theory and the experimental data outside the boundary layer $\frac{z}{\delta} > 1.0$ is considered excellent. The first tests conducted were with instrumentation located on the models as shown

by the data in figures 34(a) and (b). Certain anomalies were observed in the data for models 8 and 9 in the region subjected to the boundary-layer flow and where the instrumentation had been sparsely located. In order to obtain a more detailed pressure distribution, models 8 and 9 (as well as model 13, which is presented subsequently) were reinstrumented. Results obtained at $M_\infty = 3.71$ and $M_\infty = 4.44$ with the reinstrumented models are indicated in figures 34(c) and (d) by the symbols with ticks. These results indicate that an irregular pressure distribution does, in fact, occur and the location of peak pressure within the boundary layer is a function of sweep as well as Mach number. Lack of data in the region near the wall prevents identifying a peak for any of the other models with this diameter. A more complete experimental investigation would have to be performed to define, for a certainty, the flow model responsible for this irregular distribution. It is believed, however, that the peak that occurs within the boundary layer marks the location of impingement of the so-called dividing streamline (the streamline dividing the flow which is reversed from that which flows either up or around the fin leading edge) on the fin leading edge. The location of such an impingement would effectively be a stagnation point, similar to that indicated by the tuft studies presented in figure 33. Pressure distributions over the face of a two-dimensional step presented in reference 2 indicate stagnation regions at both the top and bottom of the step. A two-dimensional flow model that would give such a pressure distribution with the dividing streamline impinging on the top of the step has been proposed in reference 5. An oil flow photograph presented in reference 6 shows the location of impingement of the dividing streamline on the face of a 30° half-angle wedge.

The effect of model height on the leading-edge pressure distribution is shown in figure 35. As can readily be seen, no effect was found for the range of model heights for which data were obtained. A slight bulge in the pressure distribution occurred at $\frac{z}{\delta} = 0.2$. Although not as pronounced, it is possible that this bulge is associated with the dividing streamline phenomenon discussed previously for the models with lower sweep angles.

Presented in figure 36 is the effect of Mach number on the pressure distribution along the leading edge of models 1, 2, 9, and 13. The symbols at $\frac{z}{\delta} = 0$ again represent the data on the plates at $\frac{x}{d} = 0$ and the flagged symbols for models 9 and 13, the data obtained with the reinstrumented models. For a given value of z/δ the pressure ratio decreases with increasing Mach number. This is the same trend that is found experimentally with a pitot probe in a supersonic turbulent boundary layer. The peak pressure is seen to move closer to the wall as Mach number is increased (figs. 36(c) and 36(d)). This is perhaps a result of the increase in momentum of the air with Mach number, forcing the dividing streamline (indicative of the height of the separated region) closer to the plate. The effect of diameter can also be determined by comparing the various parts of figure 36.

The peak pressure in the boundary layer is seen to be a function of diameter, as well as sweep and Mach number mentioned previously. Apparently, if there is a peak it occurs closer to the wall than the nearest instrumentation

for models 1 and 2 since no irregularities were found. The extent of the upstream disturbed flow region of models 1, 2, 9, and 13 is apparently proportional to diameter as discussed previously. A comparison of the distance from the wall to the point of peak pressure on the model leading edge for models 9 and 13 indicates that this distance is proportional to diameter also. Based on the results from models 9 and 13, the peak would have occurred at $\frac{z}{\delta} = 0.09$ and 0.12 for models 1 and 2, respectively.

Typical results of the effect of Reynolds number on the leading-edge pressure distribution are shown in figure 37. These data are for model 9 and for Mach numbers of 2.98 and 4.44. Outboard of $\frac{z}{\delta} = 0.8$ there is no effect of the Reynolds number variation. Inboard of $\frac{z}{\delta} = 0.8$, there is a small effect with the pressure increasing with increasing Reynolds number.

Pressure distributions around the model leading edge for each sweep angle of this investigation are presented in figure 38. Data are presented for each of the three spanwise stations where peripheral instrumentation was located. Also presented for each sweep angle is a modified Newtonian theory curve based on the free-stream Mach number. The instrumentation was located in a plane perpendicular to the leading edge. The orifice on the stagnation line was located at the value of z/δ given in the figure. The data for the two outboard stations are in close agreement for all models. (The 75° sweep model had only one peripheral instrumentation location.) The lower values shown in figure 34 along that portion of the model within the boundary layer are shown in figure 38 to remain low around most of the leading edge for $\frac{z}{\delta} = 0.5$. The theory curves are in close agreement with most of the data from the two outboard stations. The only disagreement is in models 8, 9, and 7 for $\theta > 45^\circ$ where the theory is slightly lower than the data.

The effect of diameter on the pressure distribution around the model leading edge is presented in figure 39 for the three spanwise stations where peripheral instrumentation was located. The data for $\frac{z}{\delta} = 1.00$ and 1.33 indicated no effect of diameter as would have been expected after examining the stagnation line data. The data at $\frac{z}{\delta} = 0.5$ indicate no effect of diameter except for the large diameter model where the data at $\theta = 0^\circ$ coincide with the stagnation line peak shown in figure 36. The data for the large fin remain higher than those for the other fins up to $\theta = 60^\circ$.

The effect of Mach number on the pressure distribution around the leading edge of model 9 for the three spanwise stations is shown in figure 40. It can be seen from figure 36(c) that there is a considerable effect of Mach number on the pressure distribution along the stagnation line from the wall out to $\frac{z}{\delta} \approx 0.8$ with the pressure ratio $p_l/p_{t,2}$ decreasing with increasing Mach number. This figure shows that for $\frac{z}{\delta} = 0.5$ this trend also occurs around the model leading edge. For $\frac{z}{\delta} = 1.00$ and 1.33 no significant effects of Mach number were found.

CONCLUSIONS

An investigation of turbulent separated flows in the vicinity of fin-type protuberances has been conducted over a free-stream Mach number range from 2.30 to 4.44 and free-stream Reynolds numbers per meter from approximately 4.9×10^6 to 14.7×10^6 . The protuberances were mounted on a plate instrumented with pressure orifices which was in turn mounted flush with the tunnel sidewall to utilize the 15.24-cm turbulent sidewall boundary layer. Analysis of the experimental results yielded the following conclusions:

1. Varying the leading-edge sweep from 0° to 30° decreased sharply both the extent of the upstream disturbed flow and the final peak pressure but had only a very slight effect on the magnitude of the first peak pressure on the plate surface. The extent of upstream disturbed flow, as well as the final peak pressure, continued to decrease with increasing sweep until at 75° , the effect of the model was barely perceptible. No definite first peak pressure could be determined for sweep angles of 45° or greater.

2. For a given sweep angle the extent of the disturbed flow upstream of the model leading edge appears to vary linearly with diameter for the range of variables of this investigation.

3. For 5.08-cm diameter and 30° sweep models, varying the ratio of model height to boundary-layer thickness from 0.167 to 1.667 had no effect on the extent of disturbed flow.

4. Both the first peak and final peak pressure ratios increased with increasing Mach number for any given model.

5. Varying the free-stream Reynolds number by a factor of three had no effect on the extent of disturbed flow. The Reynolds number effects on the shape of the distributions were negligible for Mach number of 2.98 but increased slightly with increasing Mach number.

6. A comparison of first peak pressure coefficients for three-dimensional protuberances with those from two-dimensional protuberances indicates that the peak pressure coefficients from three-dimensional protuberances are significantly lower.

7. The data on the models outboard of the boundary layer are in good agreement with modified Newtonian theory.

8. Irregular pressure distributions were found along the model stagnation line of some of the models with a peak pressure occurring within the boundary layer.

Langley Research Center,
National Aeronautics and Space Administration,
Langley Station, Hampton, Va., August 3, 1966,
124-10-02-07-23.

REFERENCES

1. Chapman, Dean R.; Kuehn, Donald M.; and Larson, Howard K.: Investigation of Separated Flows in Supersonic and Subsonic Streams With Emphasis on the Effect of Transition. NACA Rept. 1356, 1958. (Supersedes NACA TN 3869.)
2. Kepler, C. E.; and Bogdonoff, S. M.: Interaction of a Turbulent Boundary Layer With a Step at $M_o = 3$. Rept. 238 (Contract No. N6-onr-270), Dept. Aeron. Eng., Princeton Univ., Sept. 1, 1953.
3. Vas, I. E.; and Bogdonoff, S. M.: Interaction of a Turbulent Boundary Layer With a Step at $M_o = 3.85$. Rept. 295 (AFOSR TN 55-200), Dept. Aeron. Eng., Princeton Univ., Apr. 1955.
4. Sterrett, James R.; and Emery, James C.: Extension of Boundary-Layer-Separation Criteria to a Mach Number of 6.5 by Utilizing Flat Plates With Forward-Facing Steps. NASA TN D-618, 1960.
5. Vasiliu, John: Pressure Distribution in Regions of Step-Induced Turbulent Separation. J. Aerospace Sci., vol. 29, no. 5, May 1962, pp. 596-601, 631.
6. Burbank, Paige B.; Newlander, Robert A.; and Collins, Ida K.: Heat-Transfer and Pressure Measurements on a Flat-Plate Surface and Heat-Transfer Measurements on Attached Protuberances in a Supersonic Turbulent Boundary Layer at Mach Numbers of 2.65, 3.51, and 4.44. NASA TN D-1372, 1962.
7. Price, Earl A.; Howard, Paul W.; and Stallings, Robert L., Jr.: Heat-Transfer Measurements on a Flat Plate and Attached Fins at Mach Numbers of 3.51 and 4.44. NASA TN D-2340, 1964.
8. Halprin, Robert W.: Step Induced Boundary-Layer Separation Phenomena. AIAA J. (Tech. Notes), vol. 3, no. 2, Feb. 1965, pp. 357-359.
9. Anon.: Manual for Users of the Unitary Plan Wind Tunnel Facilities of the National Advisory Committee for Aeronautics. NACA, 1956.

TABLE I.- GEOMETRIC PARAMETERS OF MODELS

Model	Diameter, d, cm	Height, h, cm	Sweep, Λ , deg
1	1.47	25.40	12.9
2	1.91	25.40	12.9
3	5.08	2.54	30.0
4	5.08	5.08	30.0
5	5.08	10.16	30.0
6	5.08	15.24	30.0
7	5.08	25.40	30.0
8	5.08	25.40	00.0
9	5.08	25.40	12.9
10	5.08	25.40	45.0
11	5.08	25.40	60.0
12	5.08	15.24	75.0
13	8.89	25.40	12.9
14	8.89	25.40	30.0

TABLE II.- LOCATION OF ORIFICES ON MODELS

z, cm	z/δ	θ, deg	Model													
			1	2	3	4	5	6	7	8	9	10	11	12	13	14
0.64	0.04	0								x	x				x	
1.27	.08	0				x	x	x		x	x			x	x	
1.91	.13	0								x	x				x	
2.54	.17	0	x	x		x	x	x	x	x	x	x	x	x	x	x
		30				x										
		60				x										
		90				x										
3.18	.21	0								x	x				x	
3.81	.25	0				x	x	x		x	x			x	x	
4.45	.29	0								x	x				x	
5.08	.33	0	x	x			x	x	x	x	x	x	x	x	x	x
		30					x									
		60					x									
		90					x									
5.72	.38	0								x	x				x	
6.35	.42	0					x	x		x	x			x	x	
6.99	.46	0								x	x				x	
7.62	.50	0	x	x			x	x	x	x	x	x	x	x	x	x
		15						x	x	x	x	x	x	x	x	x
		30	x	x				x	x	x	x	x	x	x	x	x
		45						x	x	x	x	x	x	x	x	x
		60	x	x				x	x	x	x	x	x	x	x	x
		75						x	x	x	x	x	x	x	x	x
		90	x	x				x	x	x	x	x	x	x	x	x
8.26	.54	0								x	x				x	
8.89	.58	0					x	x		x	x			x	x	
9.53	.63	0								x	x				x	
10.16	.67	0	x	x				x	x	x	x	x	x	x	x	x
10.80	.71	0								x	x				x	
11.43	.75	0	x	x				x	x	x	x	x	x	x	x	x
12.07	.79	0								x	x				x	
12.70	.83	0	x	x				x	x	x	x	x	x	x	x	x
13.97	.92	0	x	x				x	x	x	x	x	x	x	x	x
15.24	1.00	0	x	x						x	x	x	x	x	x	x
		15								x	x	x	x	x	x	x
		30	x	x						x	x	x	x	x	x	x
		45								x	x	x	x	x	x	x
		60	x	x						x	x	x	x	x	x	x
		75								x	x	x	x	x	x	x
		90	x	x						x	x	x	x	x	x	x
16.51	1.08	0	x	x						x	x	x	x	x	x	x
17.78	1.17	0	x	x						x	x	x	x	x	x	x
19.05	1.25	0	x	x						x	x	x	x	x	x	x
20.32	1.33	0	x	x						x	x	x	x	x	x	x
		15								x	x	x	x	x	x	x
		30	x	x						x	x	x	x	x	x	x
		45								x	x	x	x	x	x	x
		60	x	x						x	x	x	x	x	x	x
		75								x	x	x	x	x	x	x
		90	x	x						x	x	x	x	x	x	x
21.59	1.42	0	x	x						x	x	x	x	x	x	x
22.86	1.50	0	x	x						x	x	x	x	x	x	x
24.13	1.58	0	x	x						x	x	x	x	x	x	x

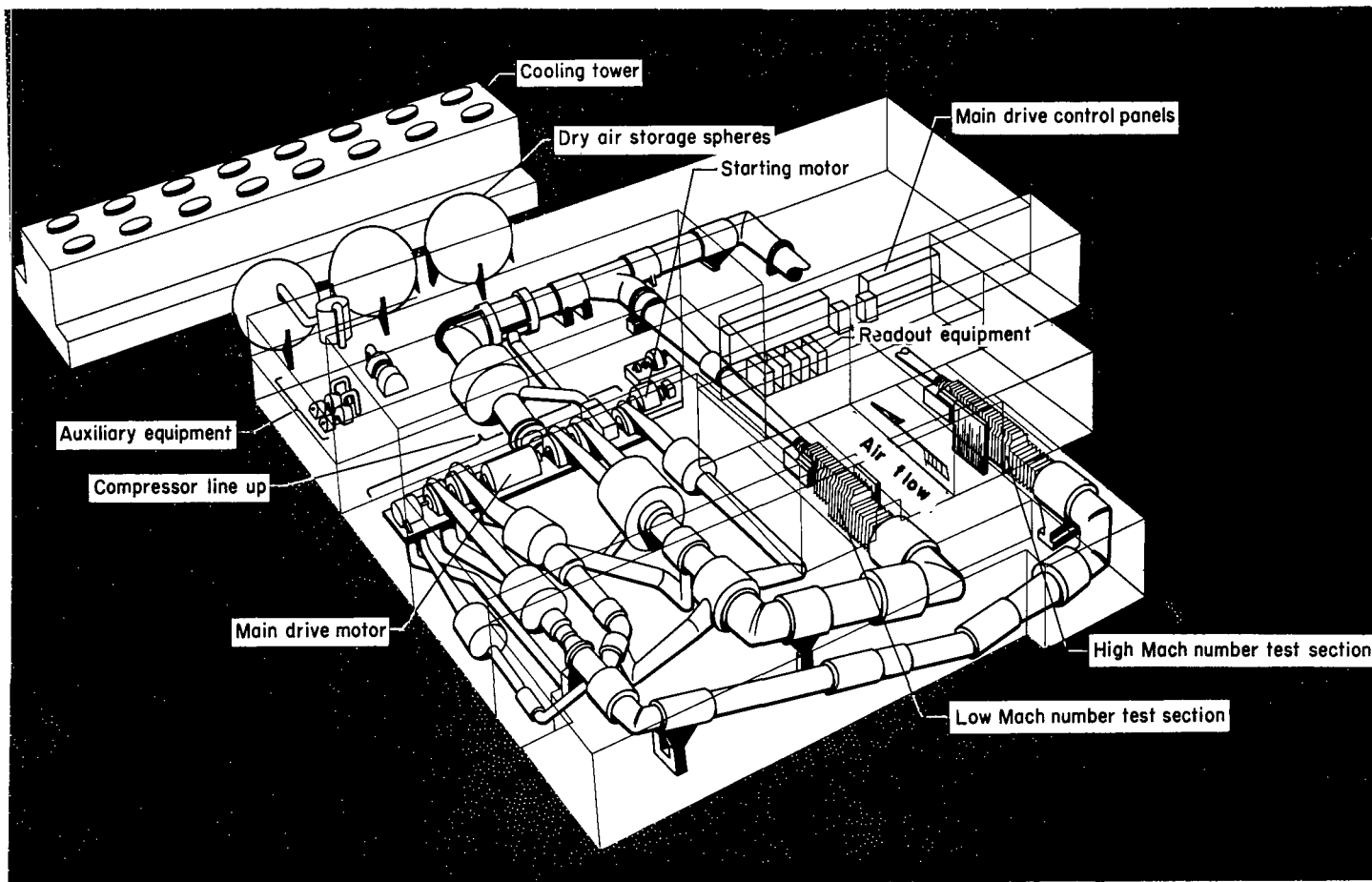


Figure 1.- Schematic of the Langley Unitary Plan wind tunnel.

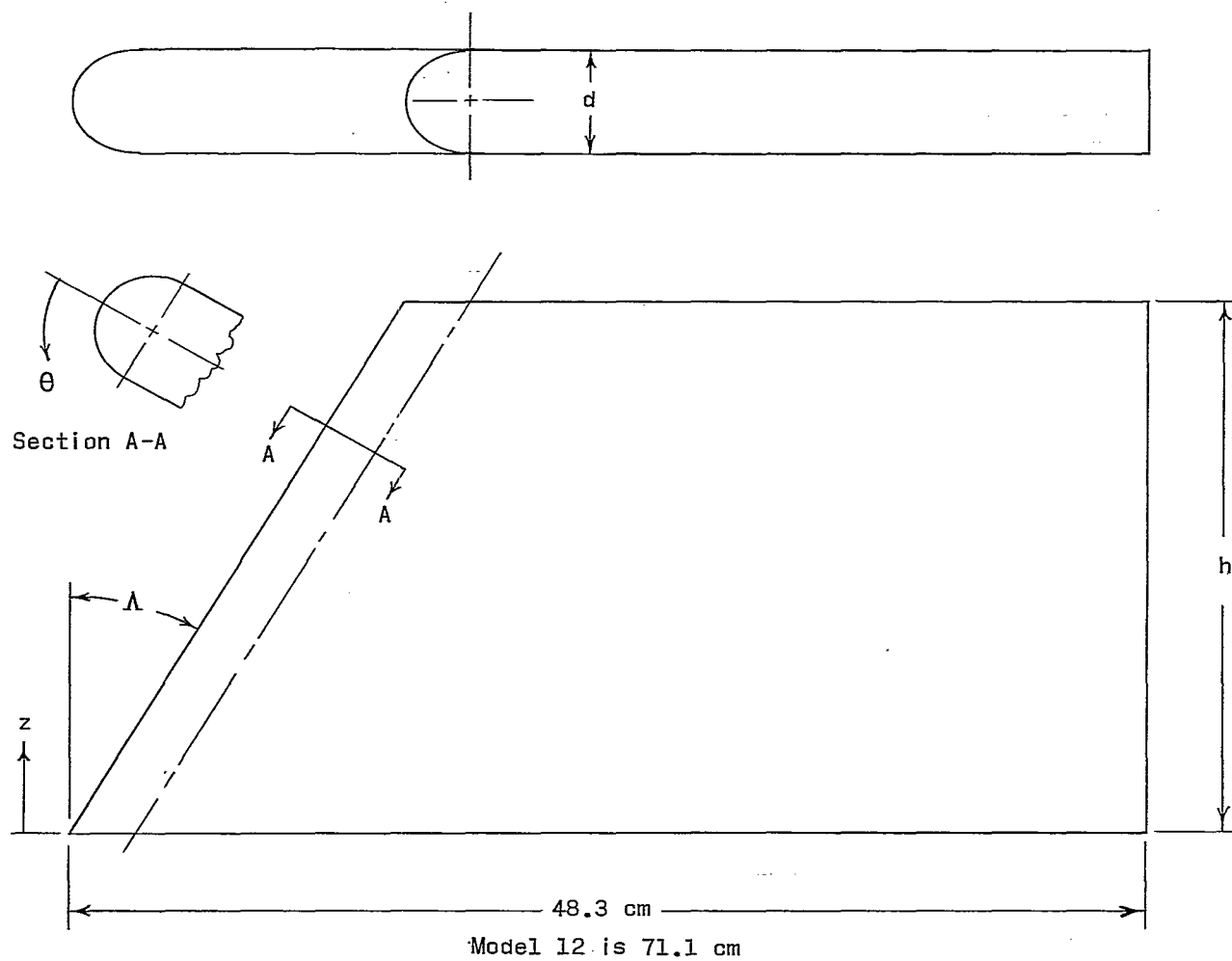
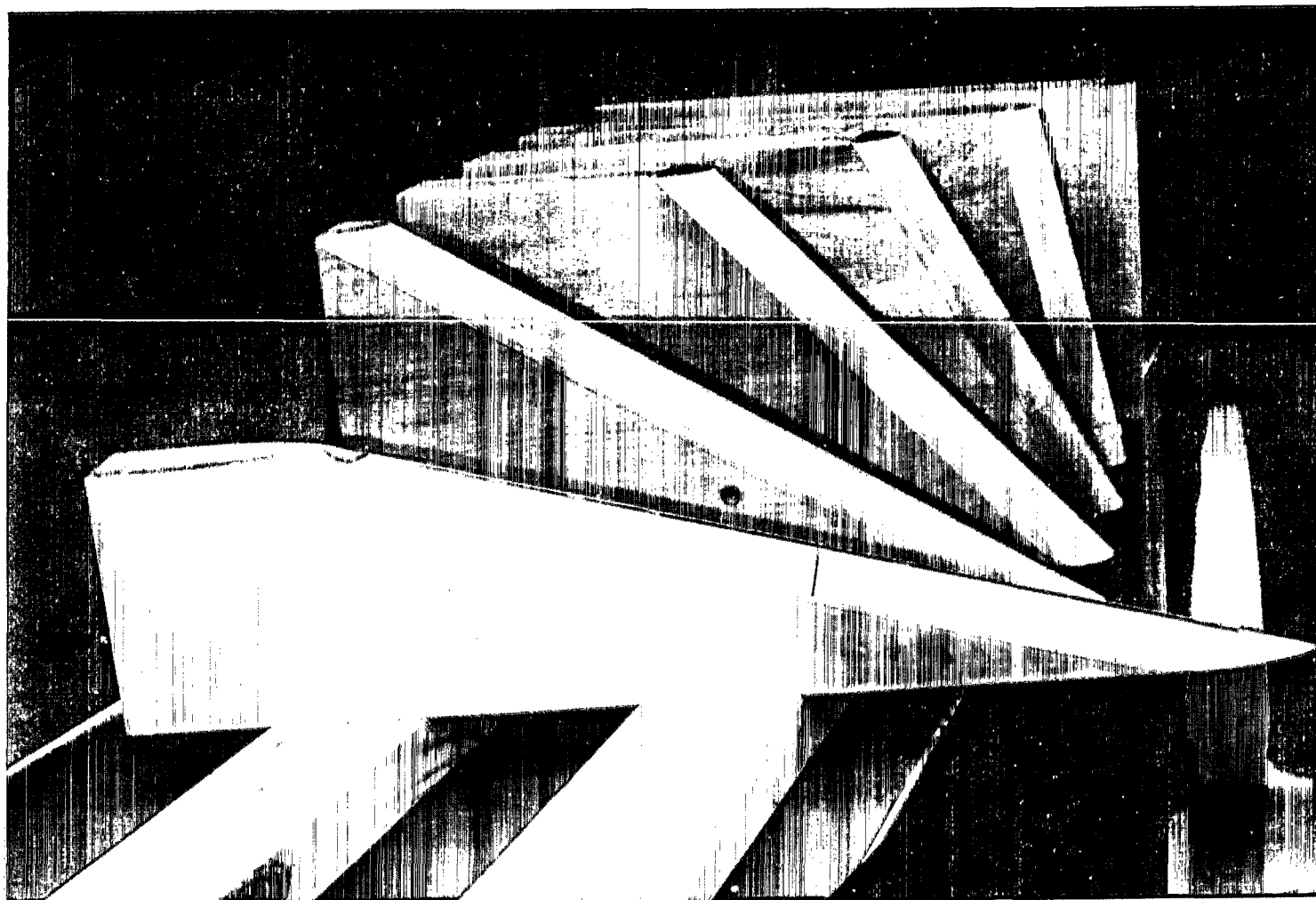


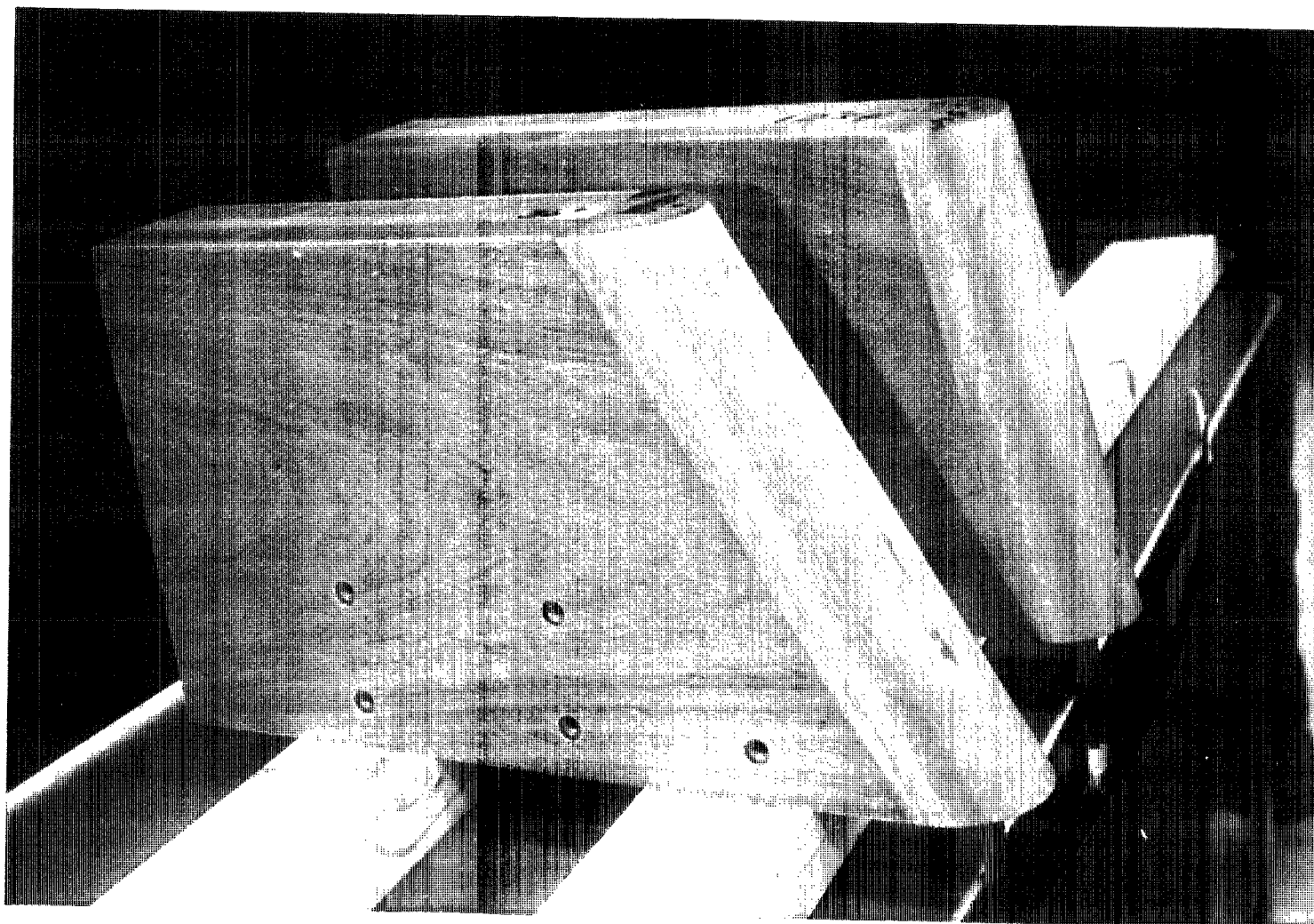
Figure 2.- Sketch of basic model geometry.



(a) Variation in sweep; $d = 5.08$ cm.

L-64-8764

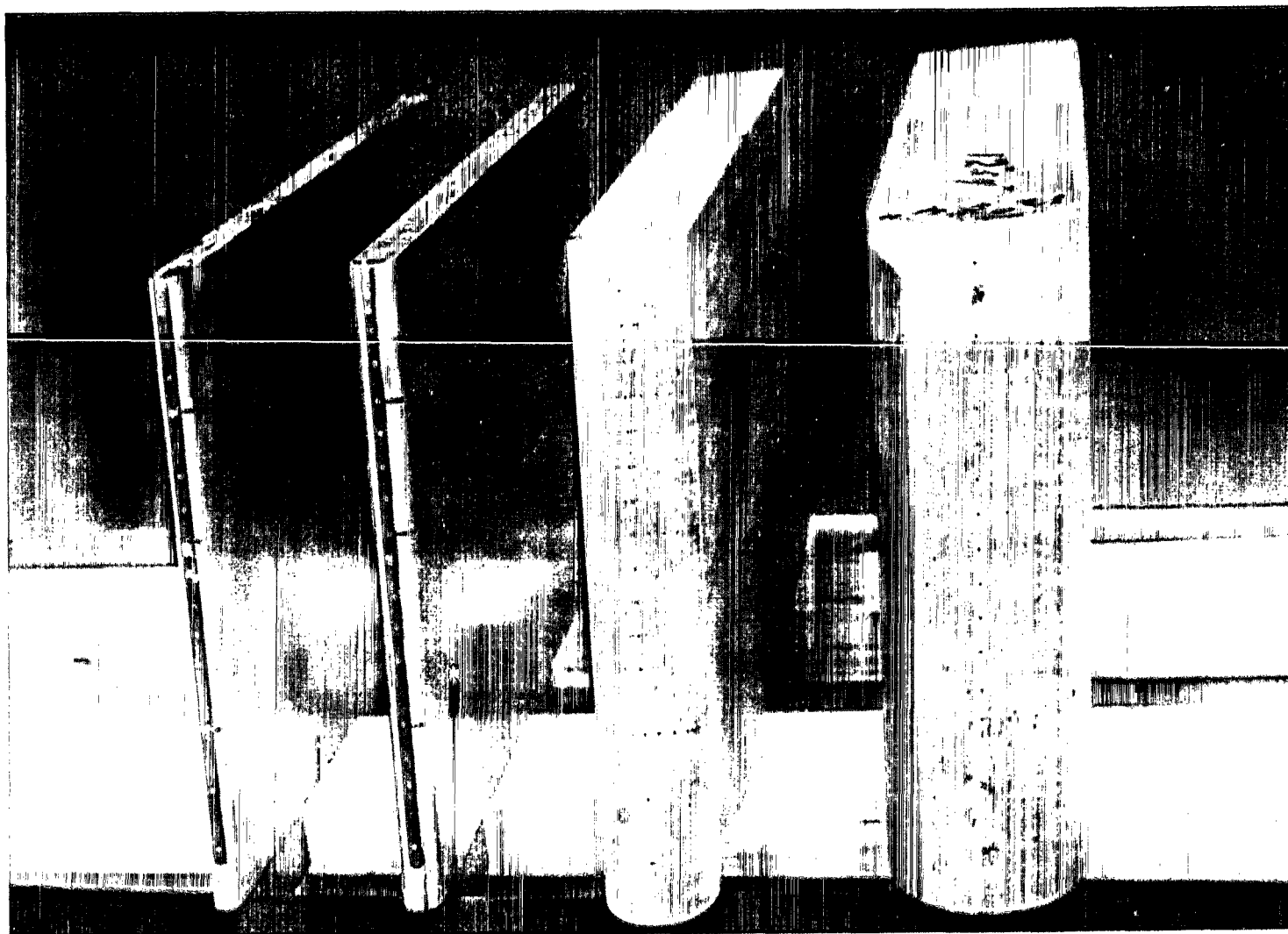
Figure 3.- Model photographs.



(b) Variation in sweep; $d = 8.89$ cm.

L-64-3767

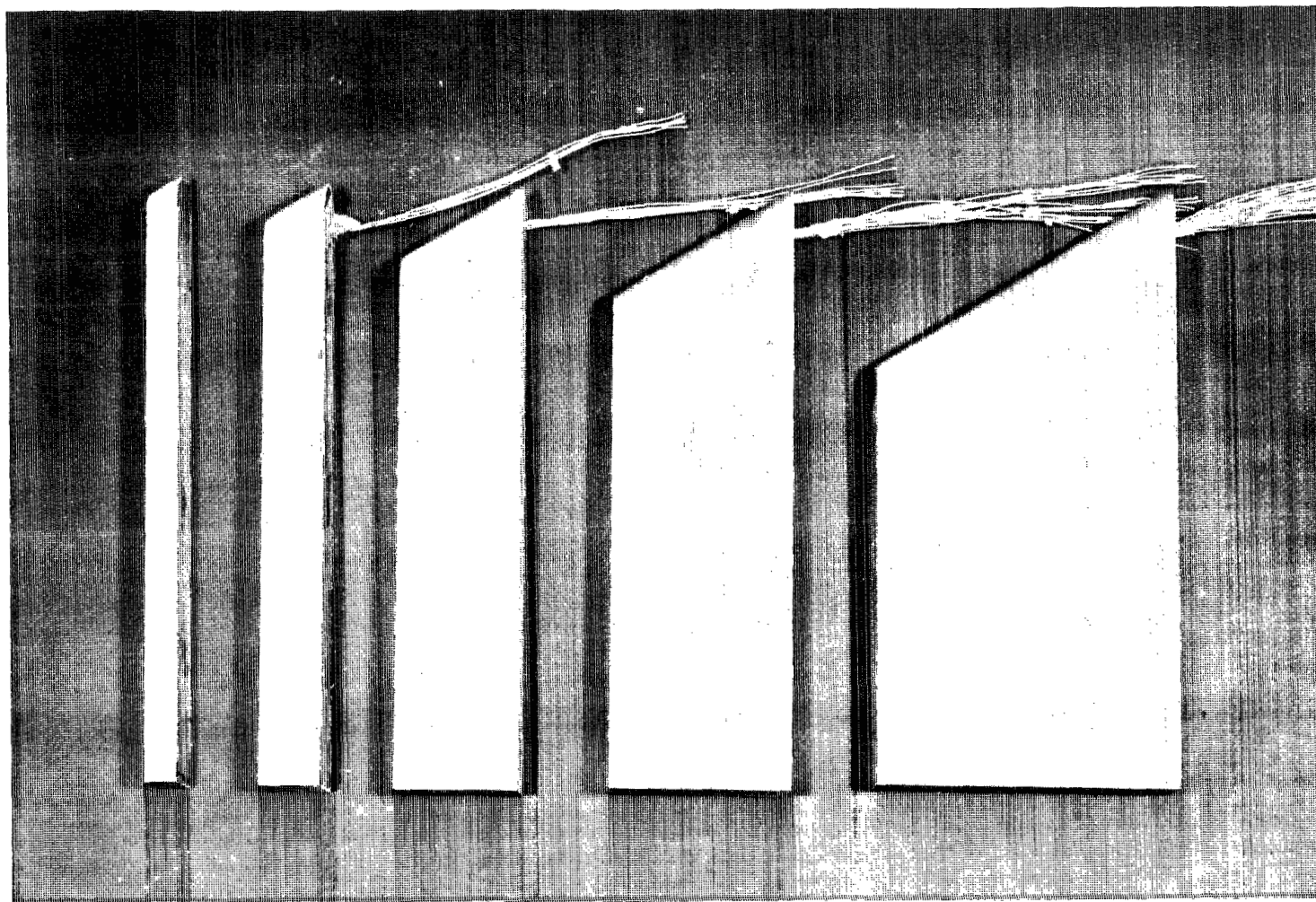
Figure 3.- Continued.



(c) Variation in diameter; $\Lambda = 12.9^\circ$.

L-64-8763

Figure 3.- Continued.



(d) Variation in height; $d = 5.08$ cm; $\Lambda = 30^\circ$.

L-65-5337

Figure 3.- Concluded.

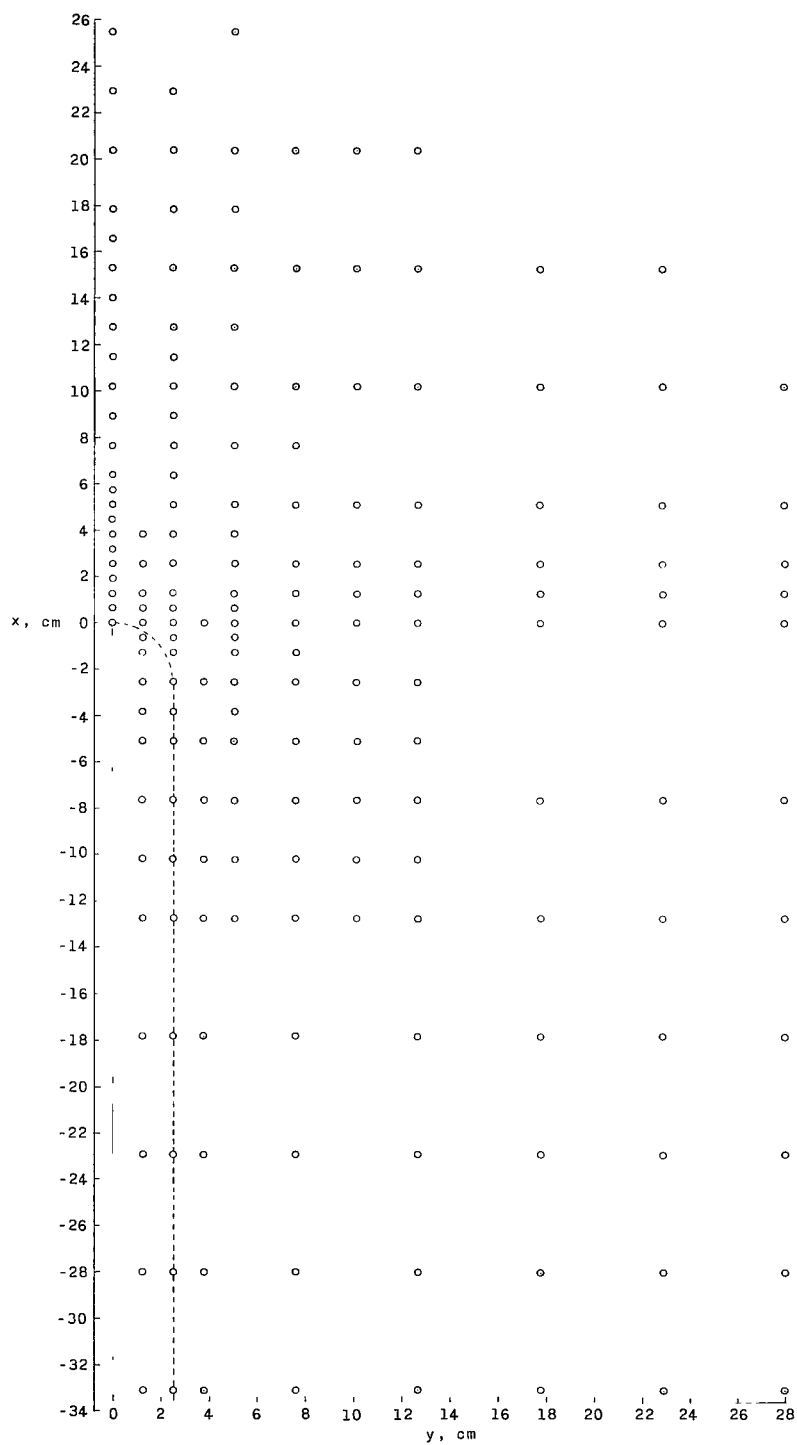


Figure 4.- Location of orifices on plate.

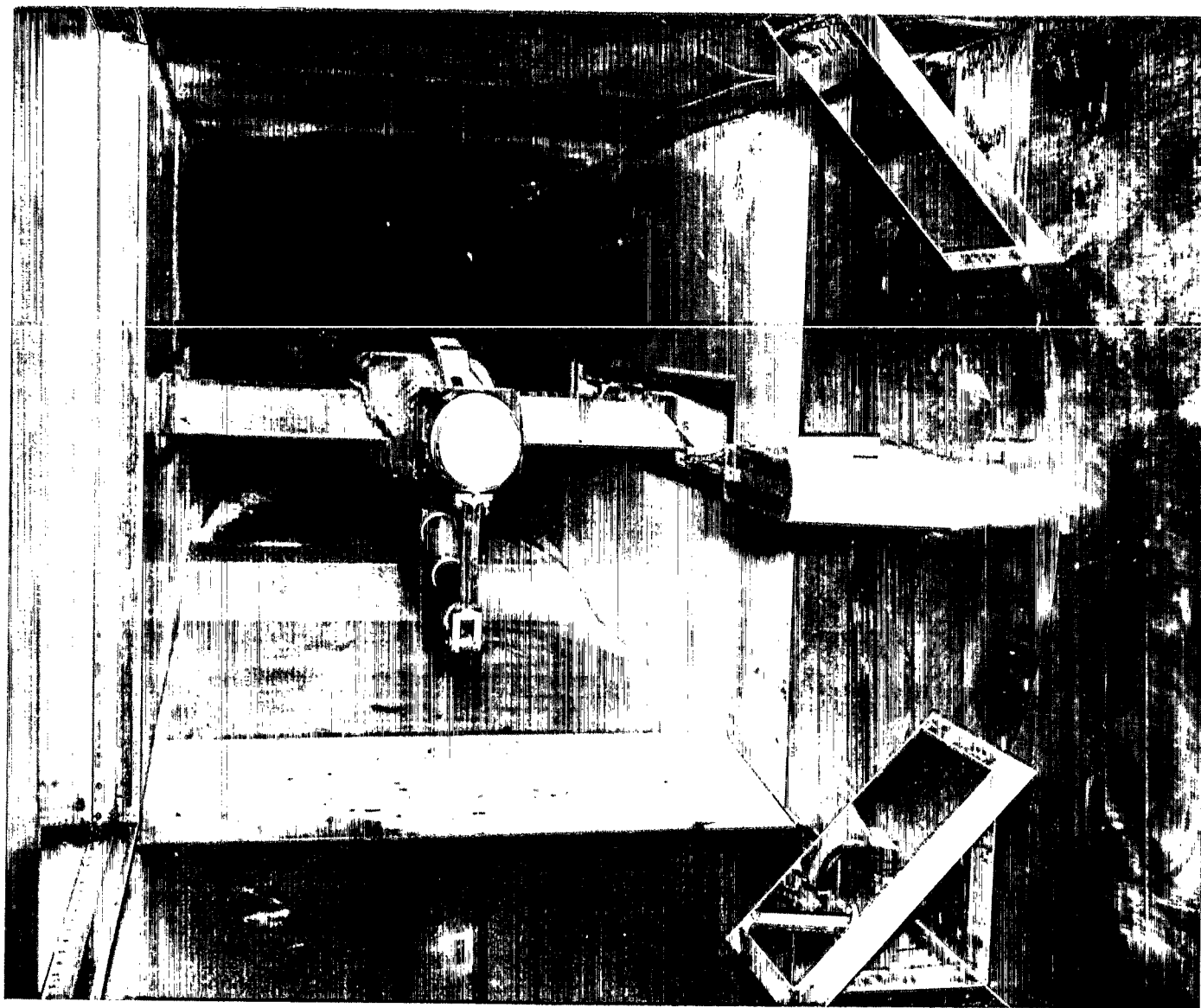


Figure 5.- Model 13 mounted on test plate in test section.

L-65-4841

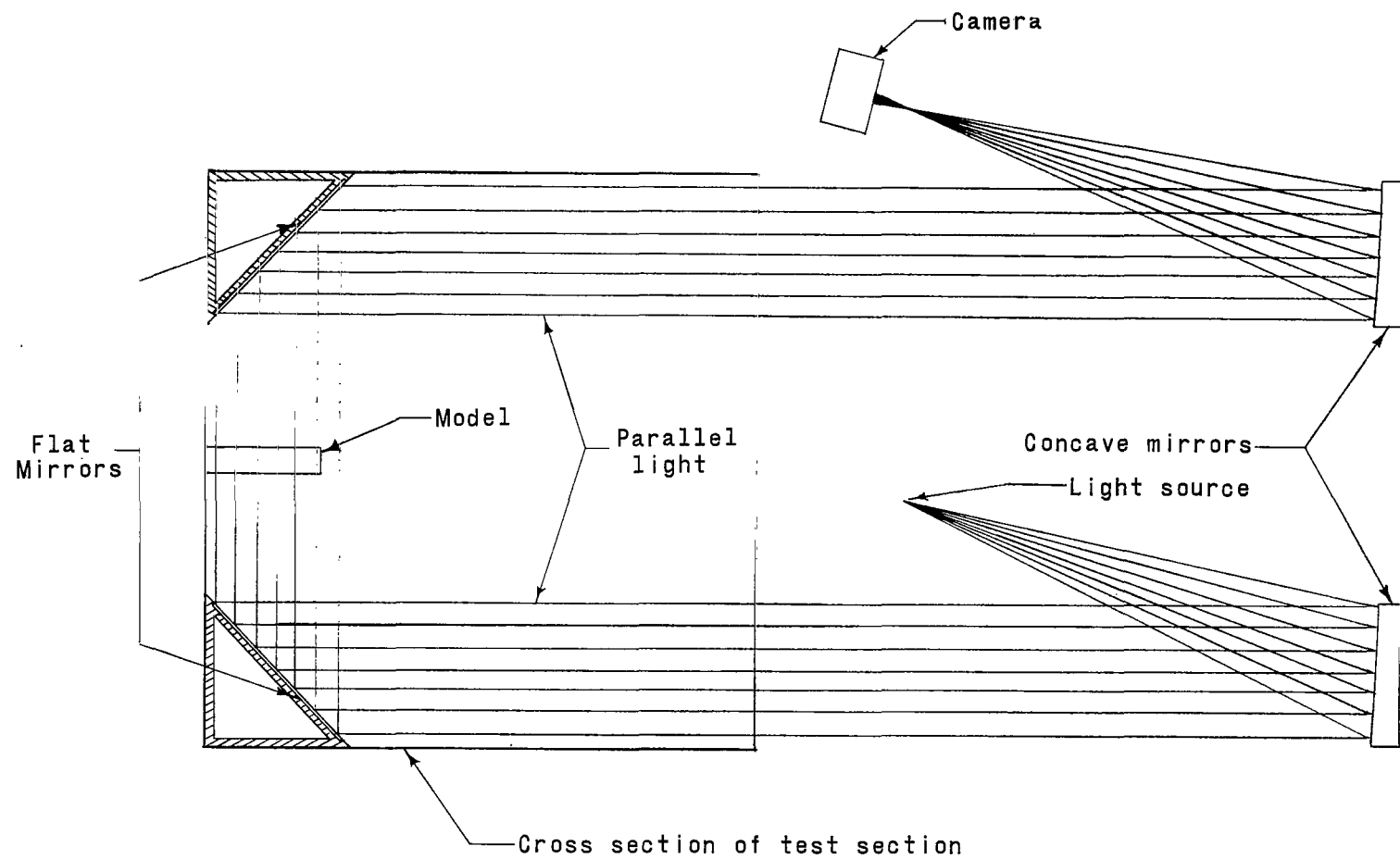


Figure 6.- Sketch of system used for shadowgraphs.

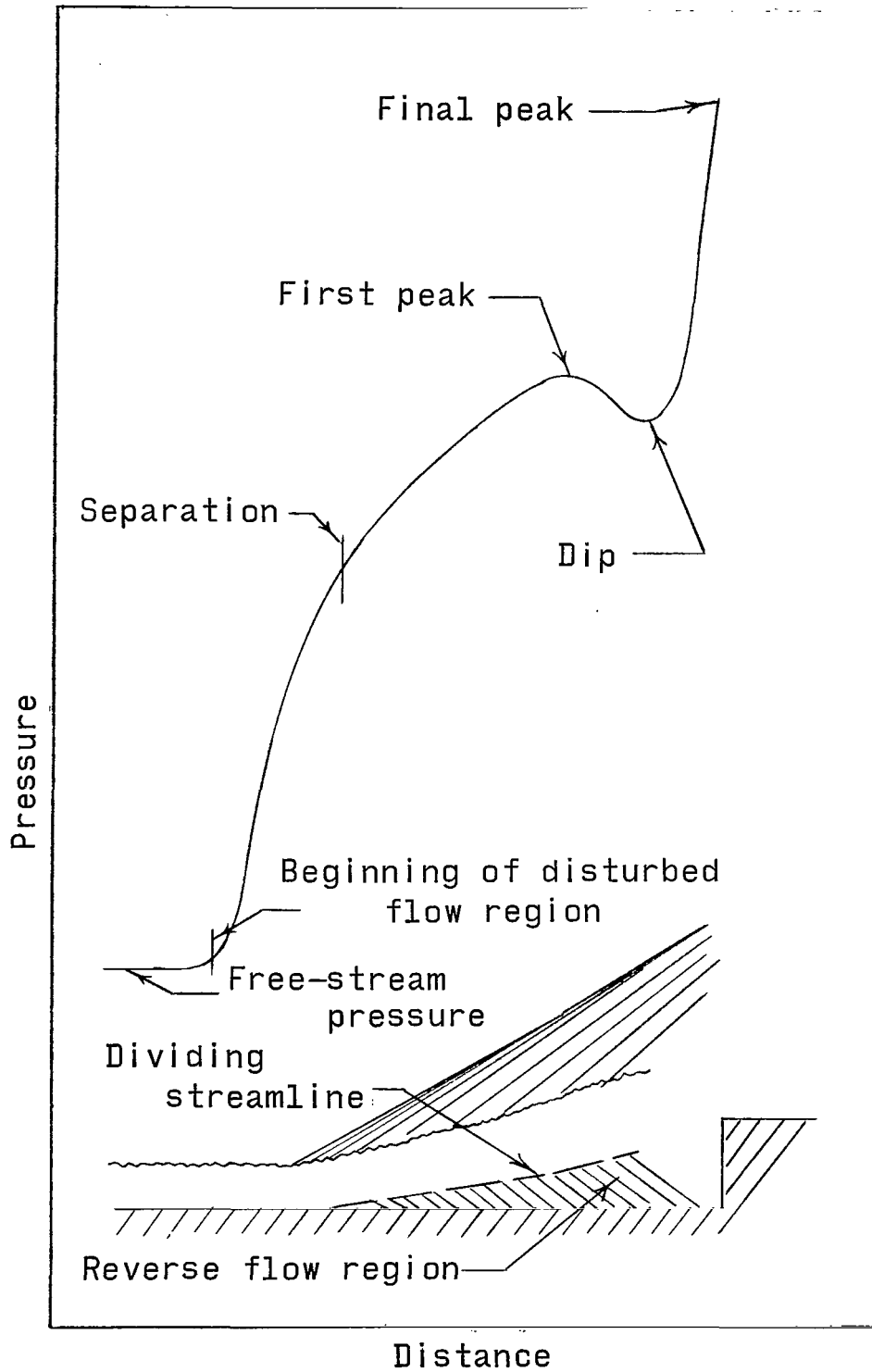
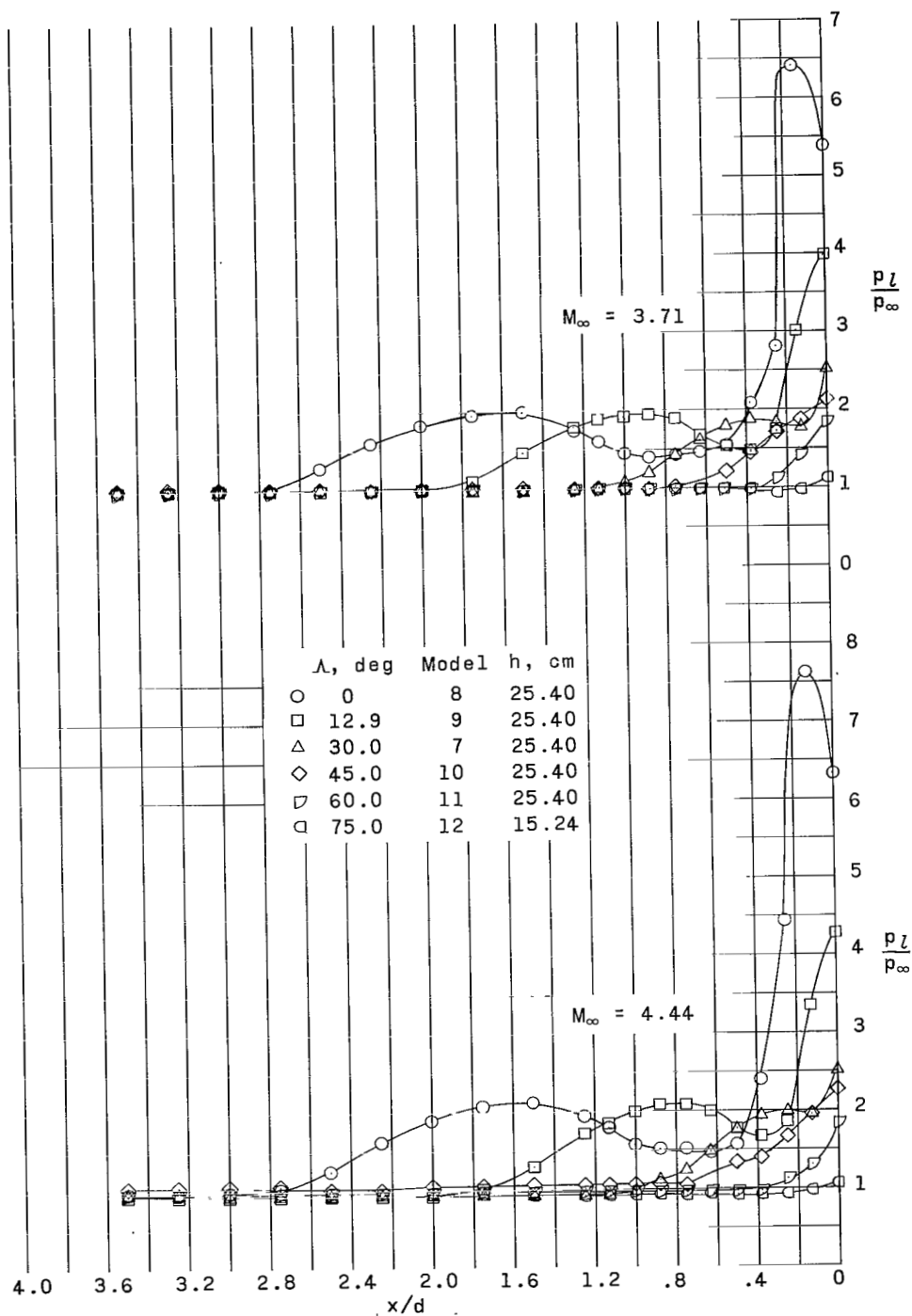
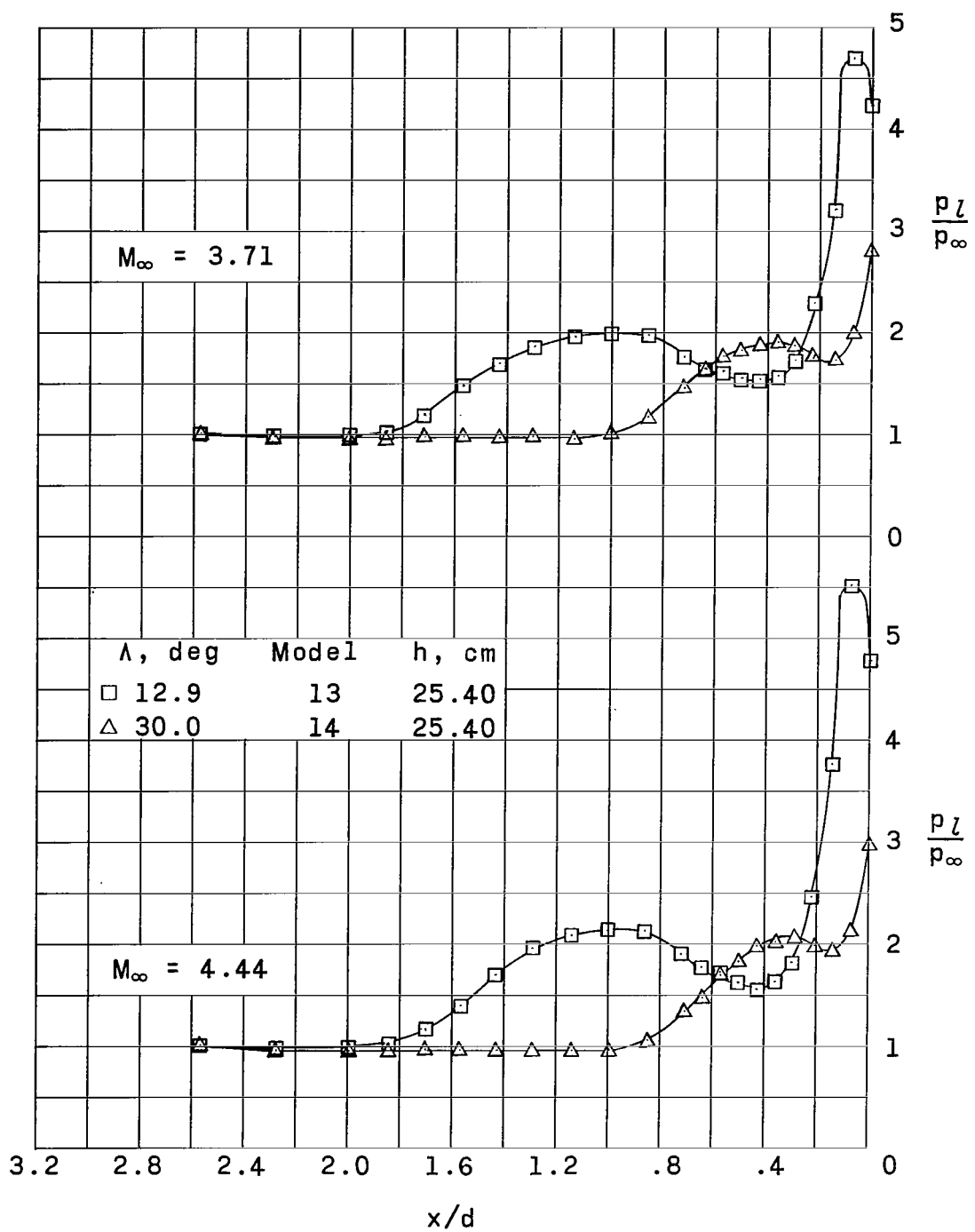


Figure 7.- Schematic drawing of a typical interaction for a two-dimensional step.



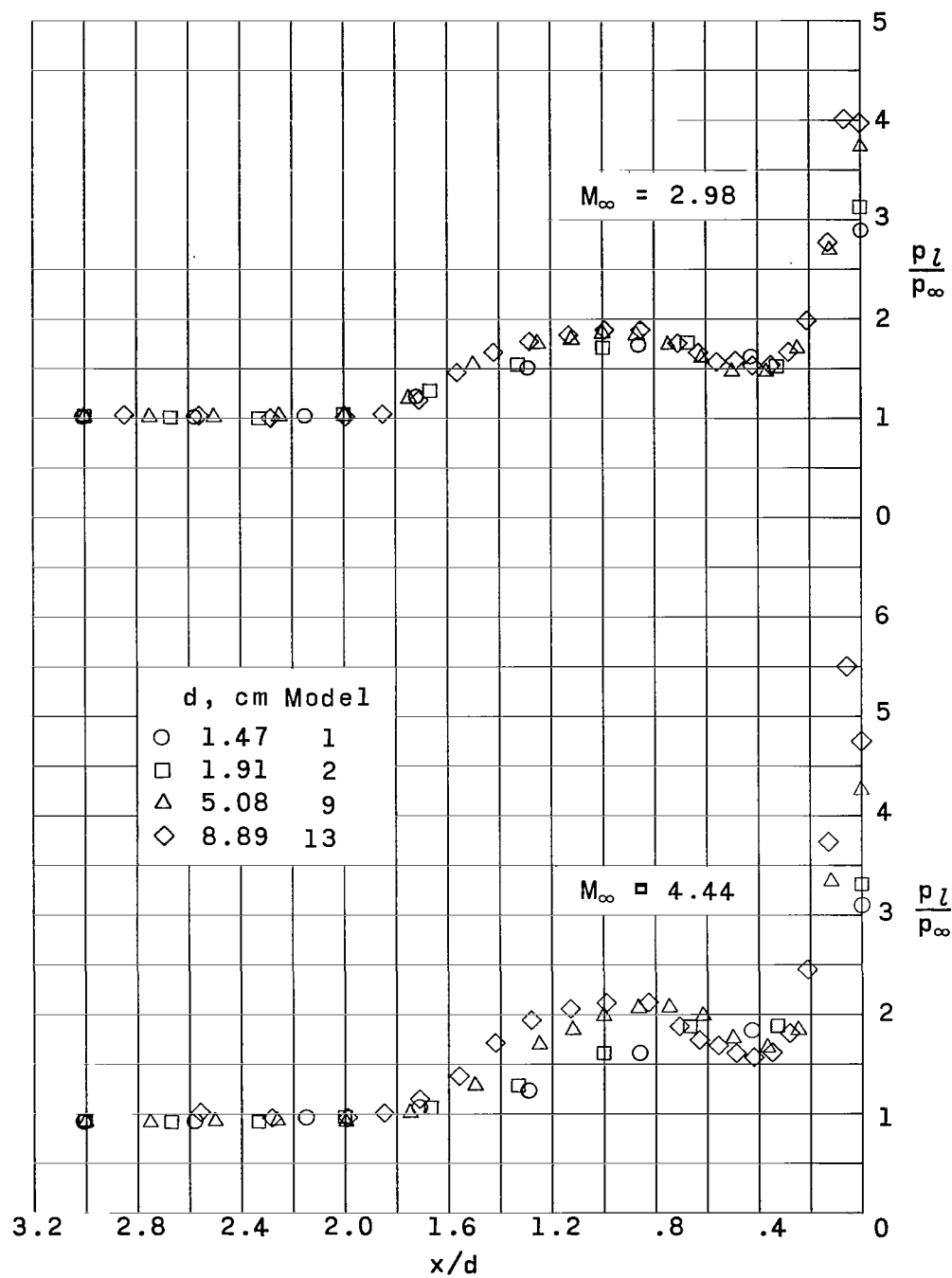
(a) $d = 5.08$ cm.

Figure 8.- Effect of sweep on the pressure distribution upstream of models. $R_\infty \approx 9.8 \times 10^6$.



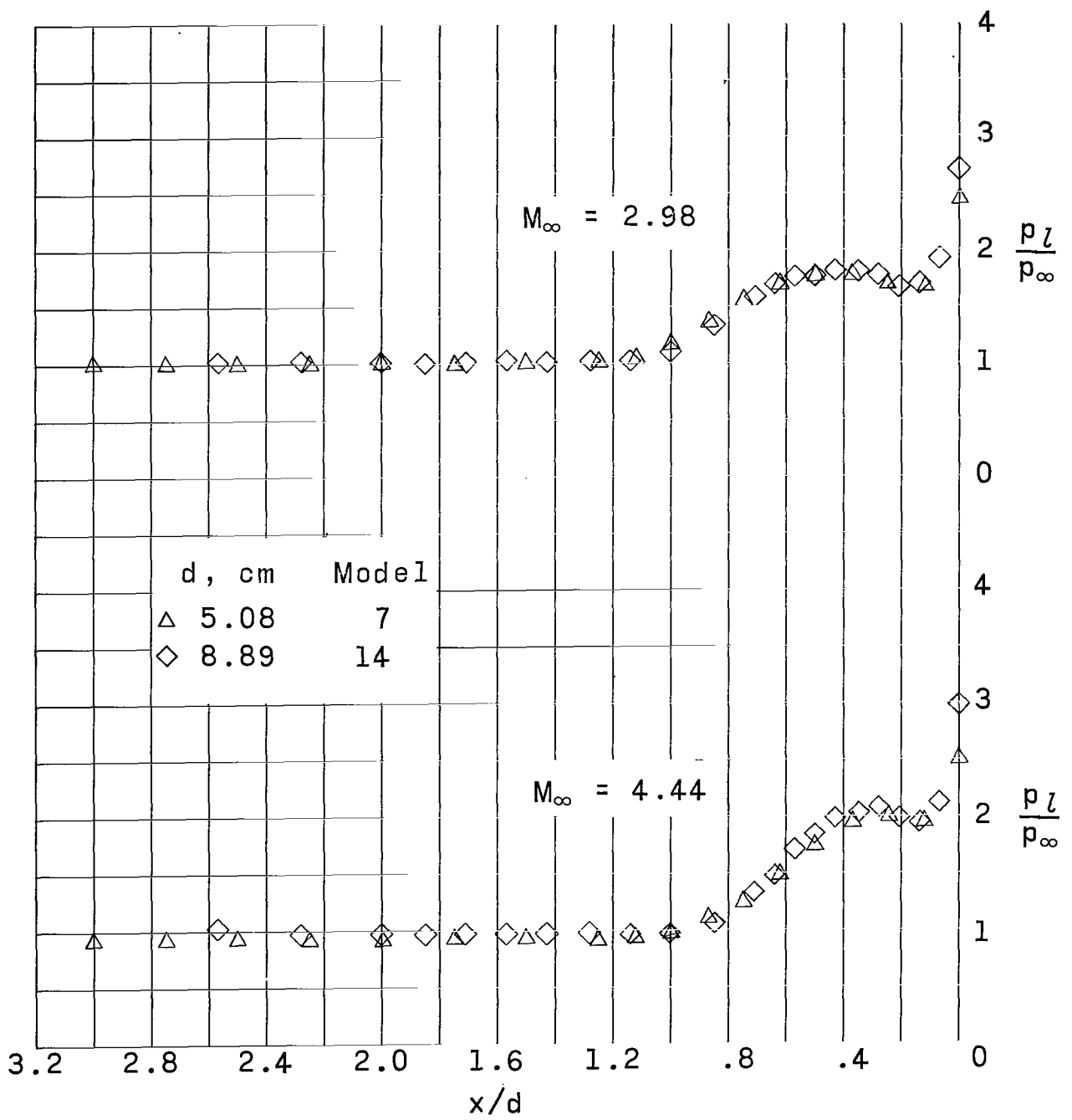
(b) $d = 8.89$ cm.

Figure 8.- Concluded.



(a) $\Lambda = 12.9^\circ$.

Figure 9.- Effect of diameter on the pressure distribution upstream of models. $h = 25.40$ cm; $R_\infty \approx 9.8 \times 10^6$.



(b) $\Lambda = 30^\circ$.

Figure 9.- Concluded.

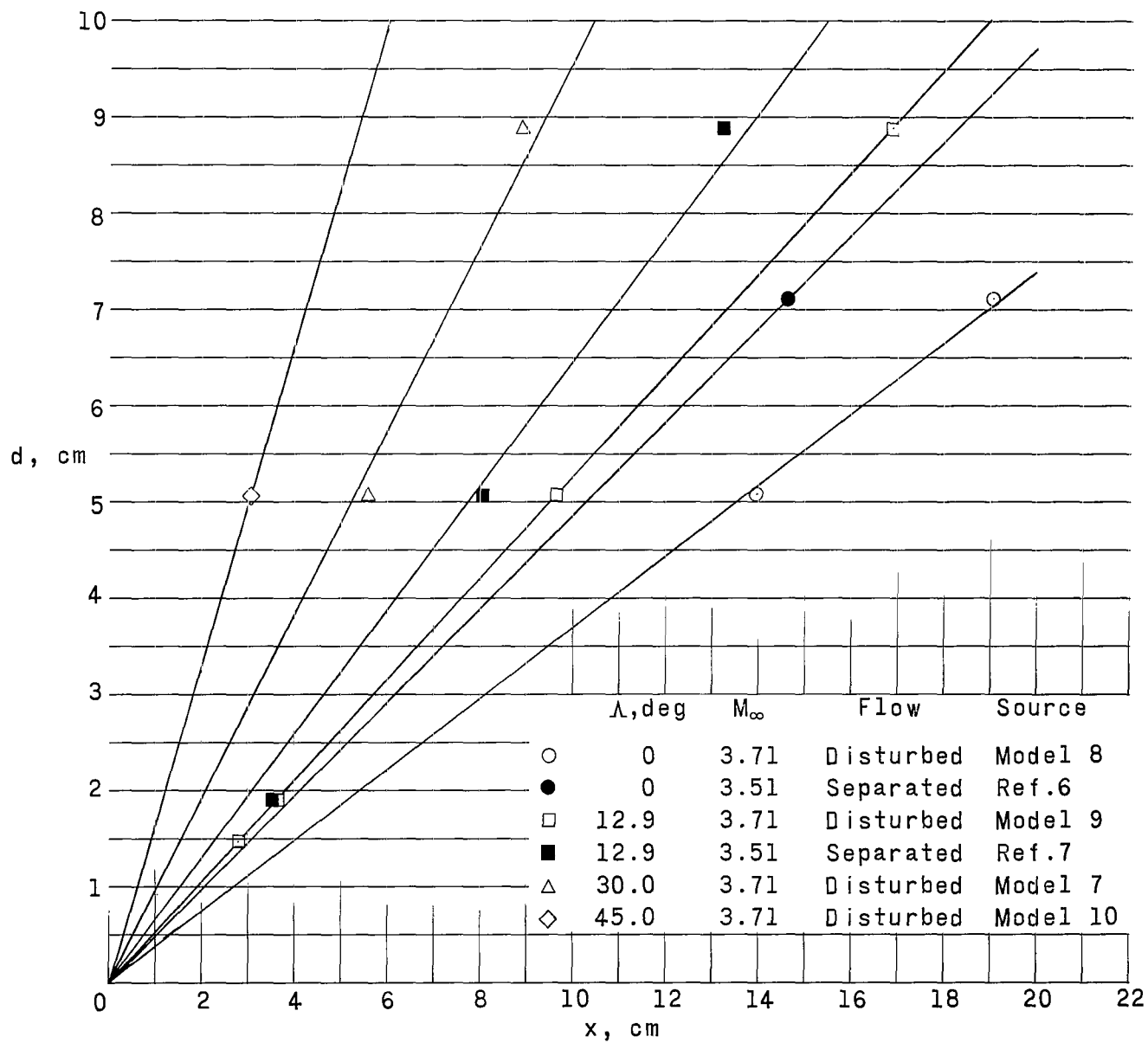


Figure 10.- Variation of the separation distance and the disturbed flow region with protuberance diameter, $\delta \approx 15.24$ cm; $R_\infty \approx 9.8 \times 10^6$.

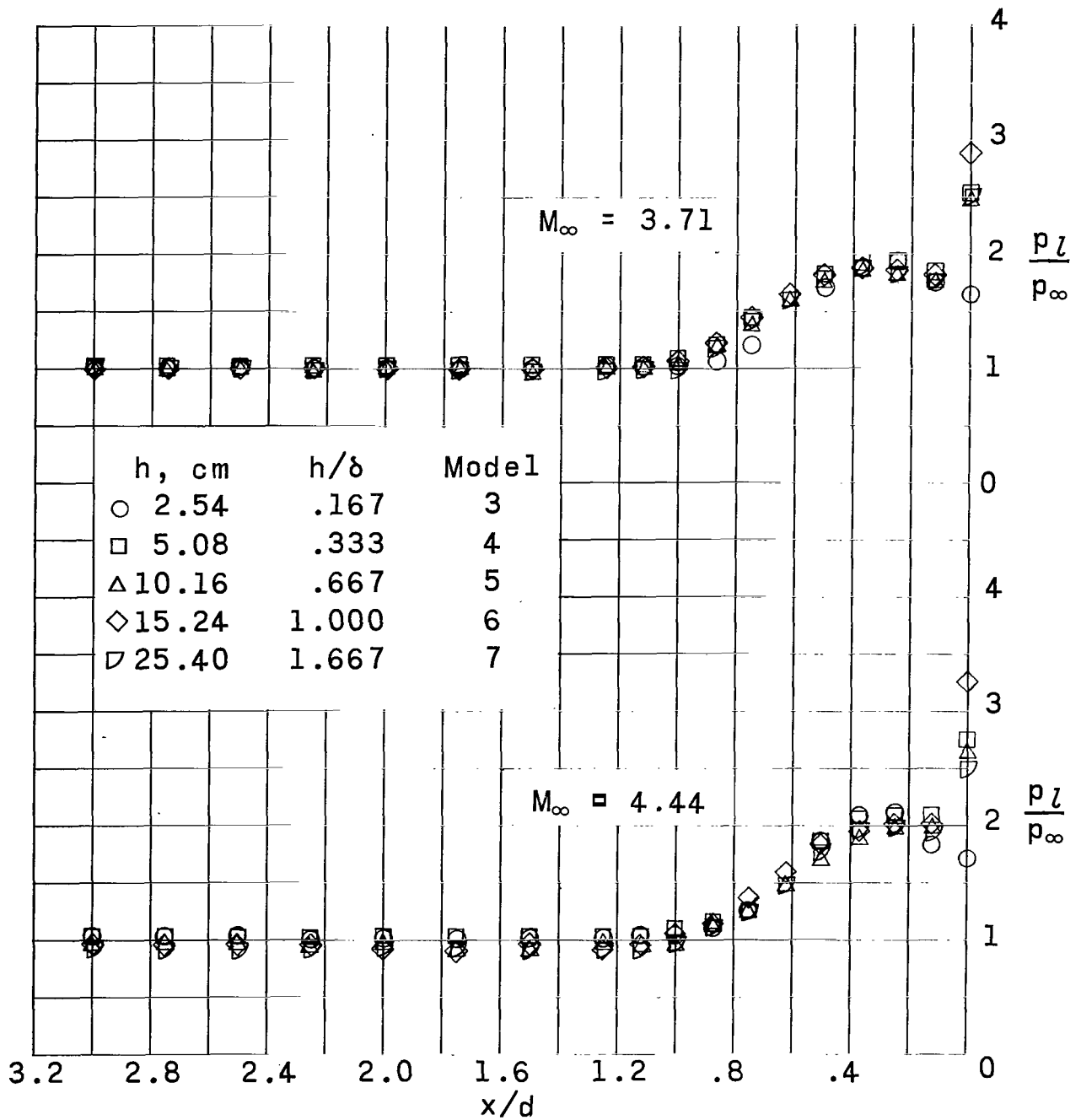
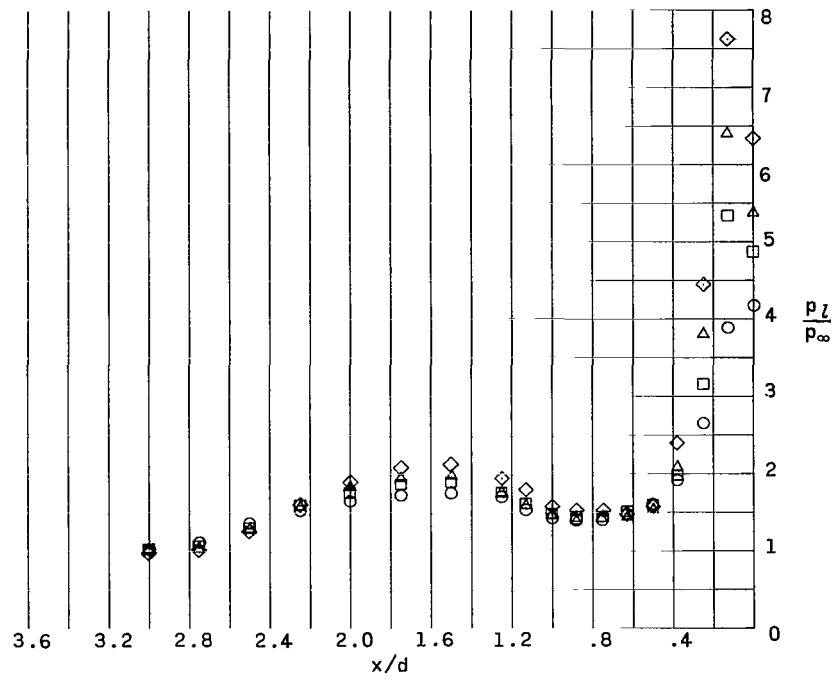
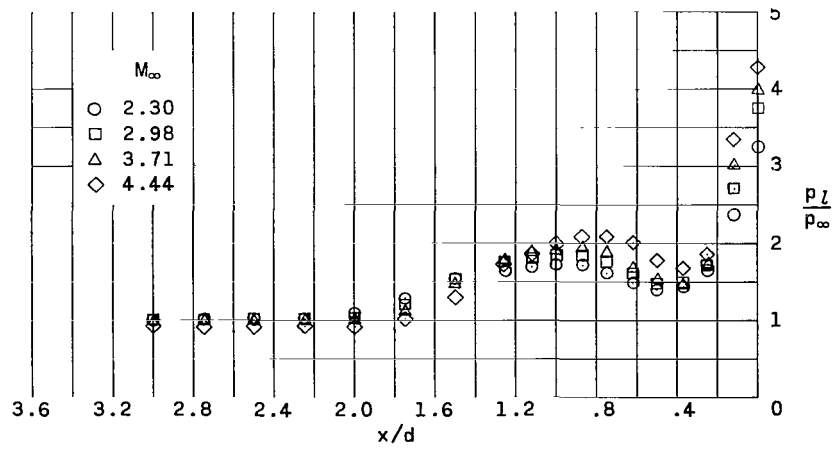


Figure 11.- Effect of model height on the upstream distribution. $d = 5.08$ cm; $\Lambda = 30^\circ$; $R_\infty \approx 9.8 \times 10^6$.

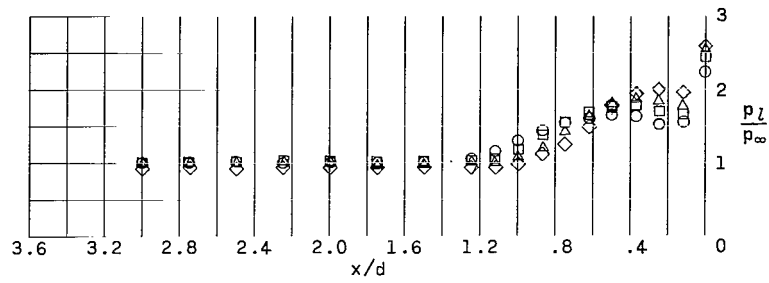


(a) Model 8; $\Lambda = 0^\circ$; $d = 5.08$ cm; $h = 25.40$ cm.

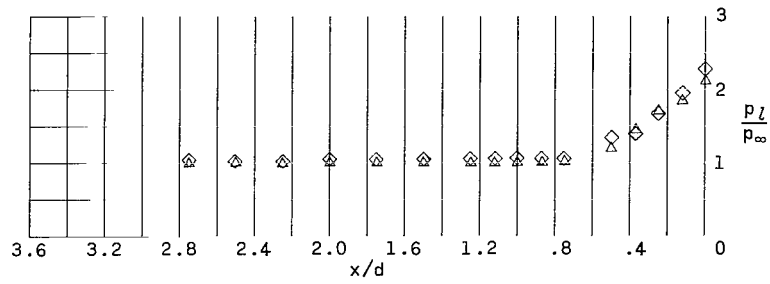


(b) Model 9; $\Lambda = 12.9^\circ$; $d = 5.08$ cm; $h = 25.40$ cm.

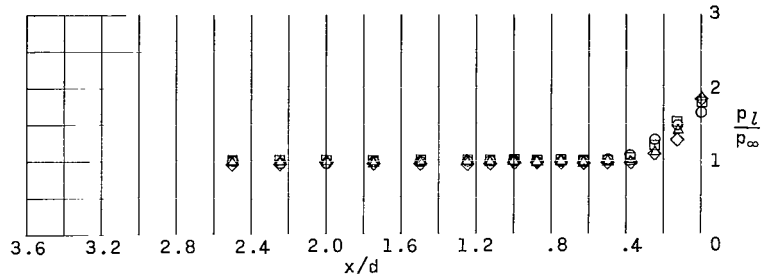
Figure 12.- Effect of Mach number on the pressure distribution upstream of models. $R_\infty \approx 9.8 \times 10^6$.



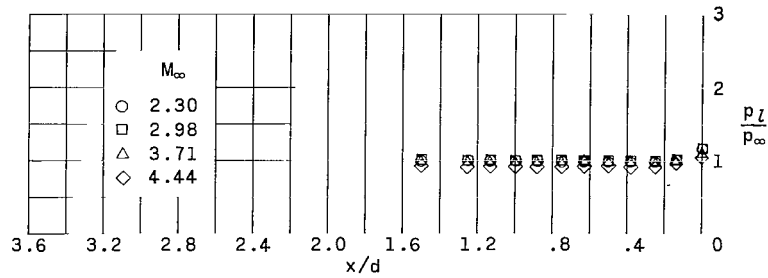
(c) Model 7; $\Lambda = 30^\circ$; $d = 5.08$ cm; $h = 25.40$ cm.



(d) Model 10; $\Lambda = 45^\circ$; $d = 5.08$ cm; $h = 25.40$ cm.

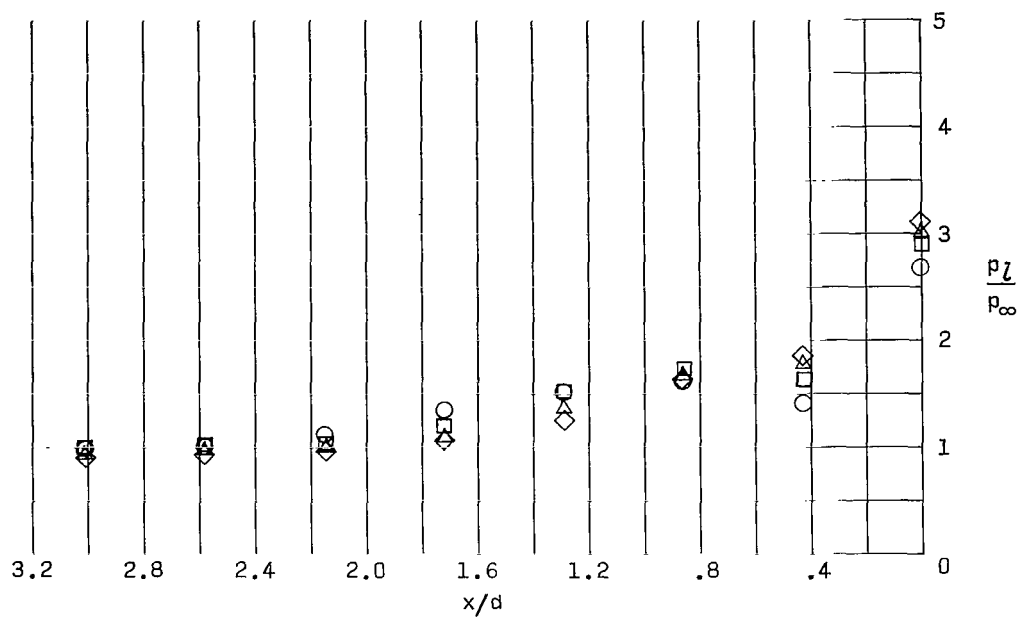


(e) Model 11; $\Lambda = 60^\circ$; $d = 5.08$ cm; $h = 25.40$ cm.

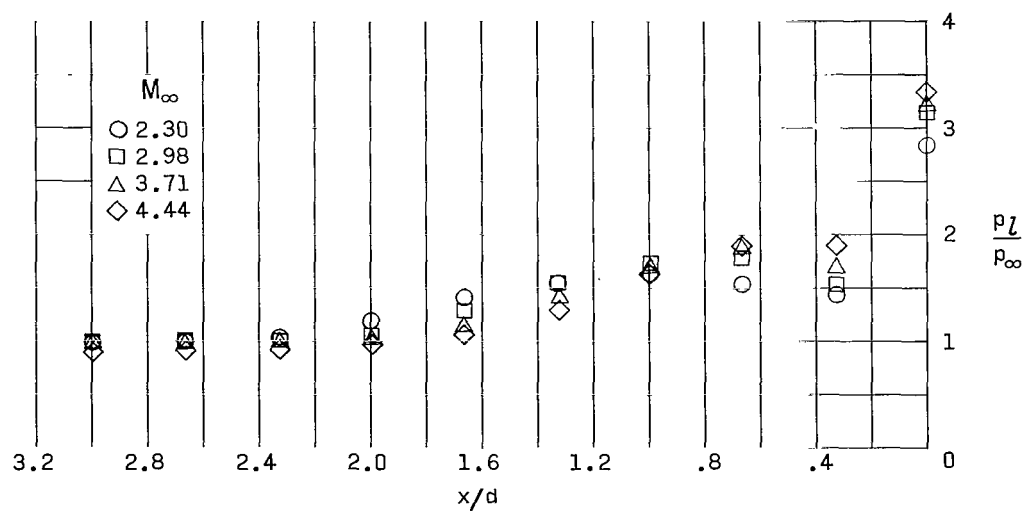


(f) Model 12; $\Lambda = 75^\circ$; $d = 5.08$ cm; $h = 15.24$ cm.

Figure 12.- Continued.

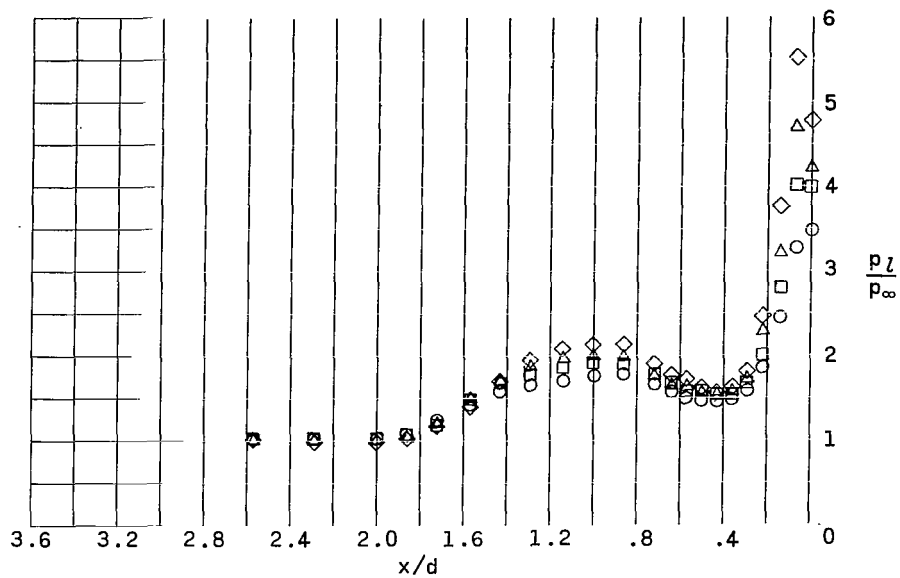


(g) Model 1; $\Lambda = 12.9^\circ$; $d = 1.47$ cm; $h = 25.40$ cm.

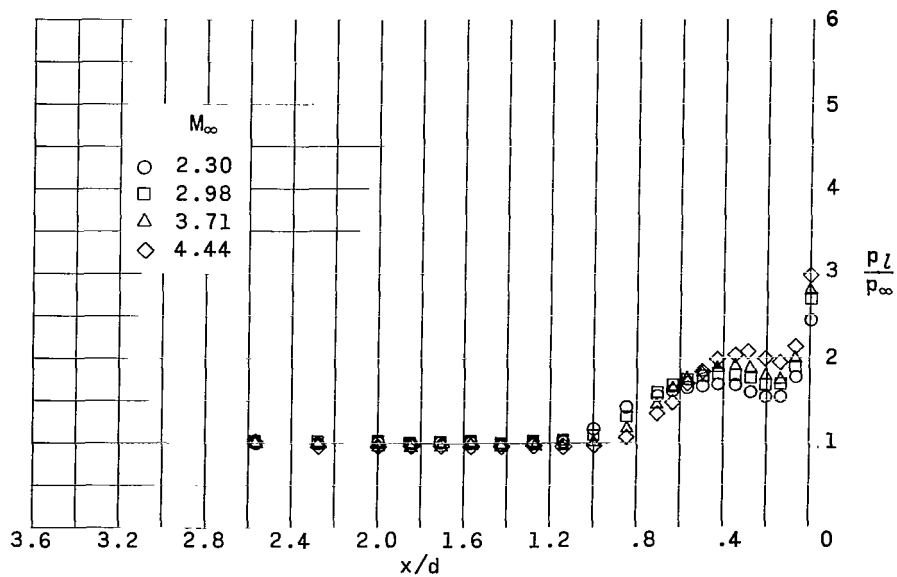


(h) Model 2; $\Lambda = 12.9^\circ$; $d = 1.91$ cm; $h = 25.40$ cm.

Figure 12.- Continued.

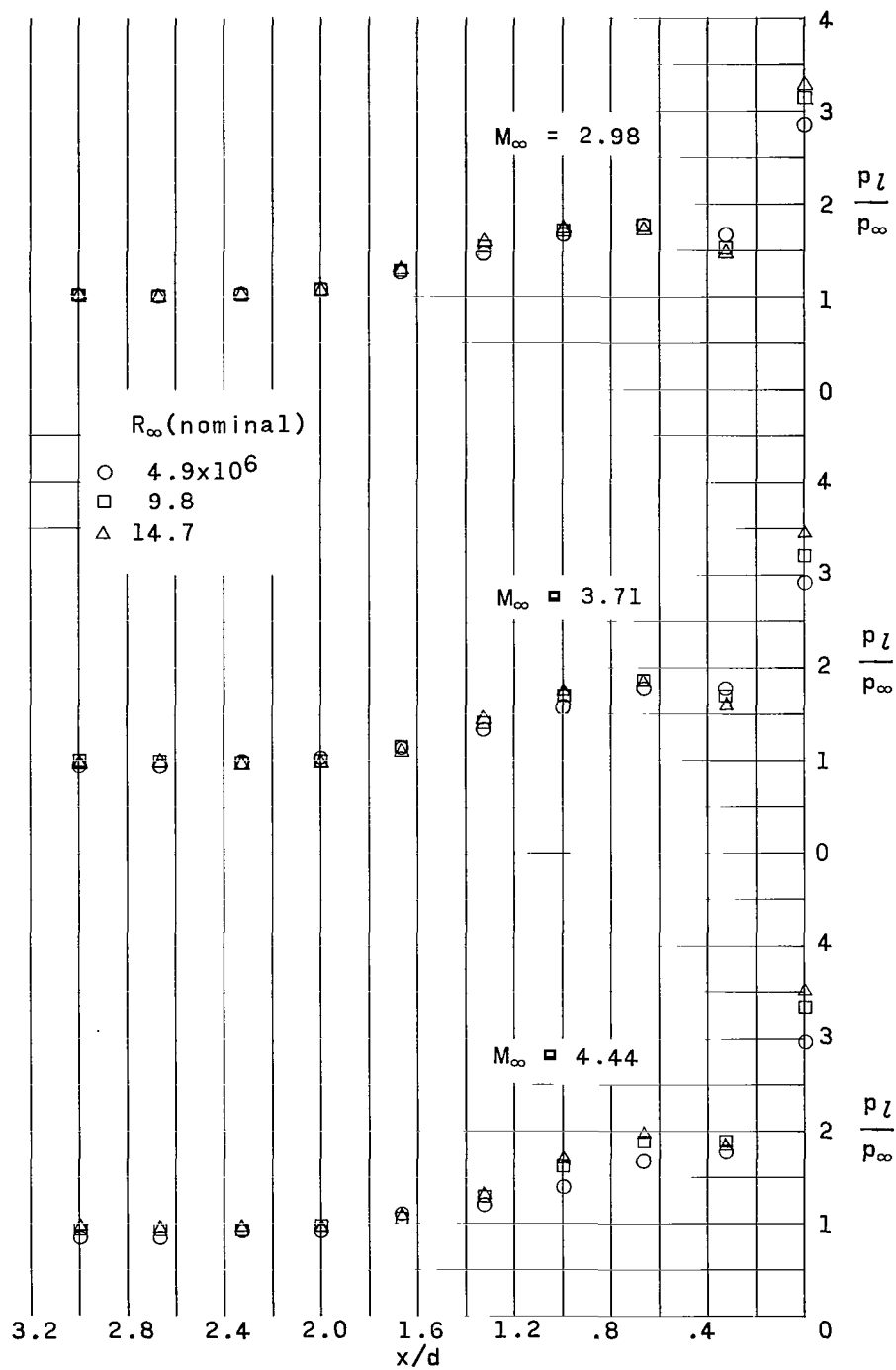


(i) Model 13; $\Lambda = 12.9^\circ$; $d = 8.89$ cm; $h = 25.40$ cm.



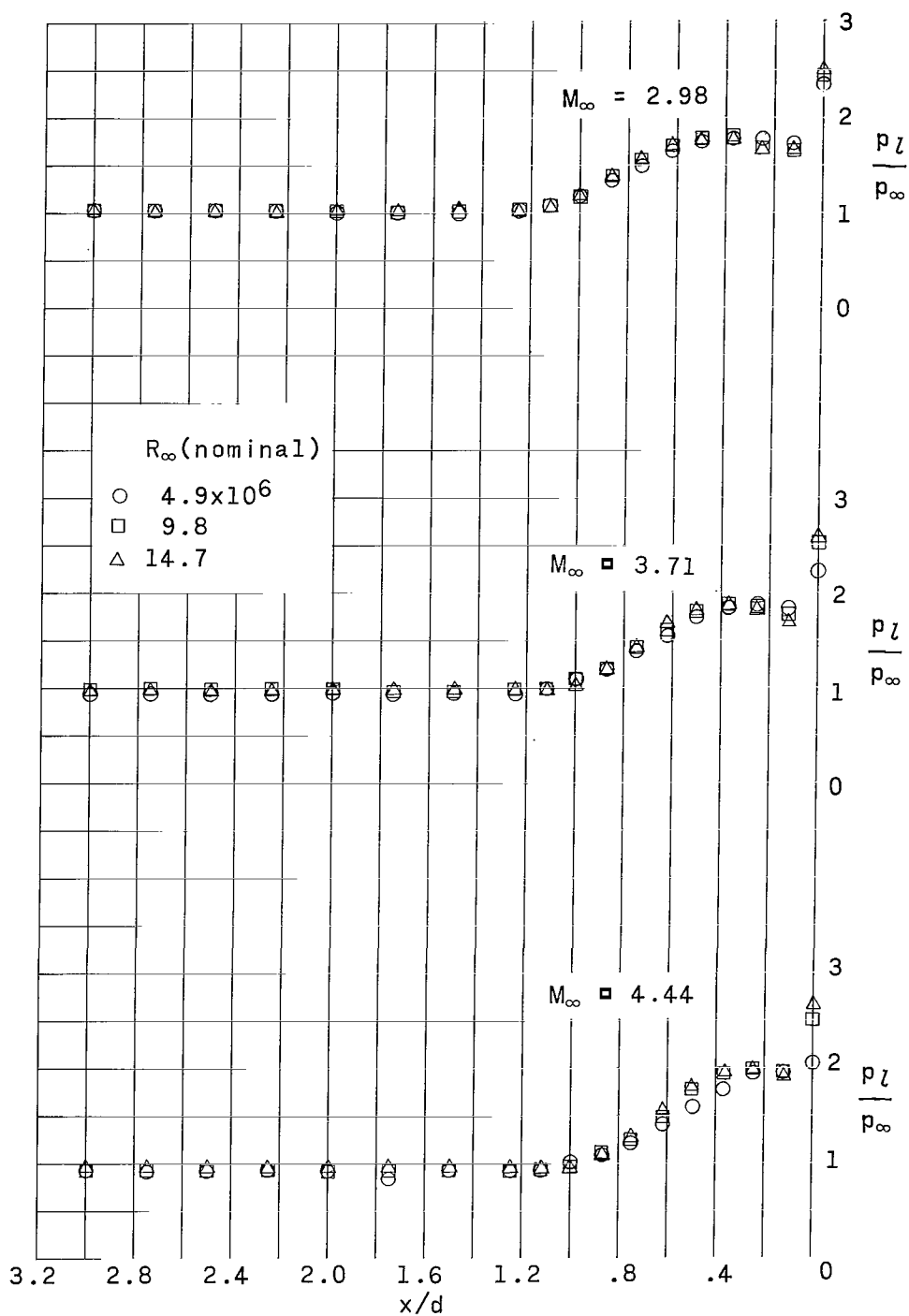
(j) Model 14; $\Lambda = 30^\circ$; $d = 8.89$ cm; $h = 25.40$ cm.

Figure 12.- Concluded.



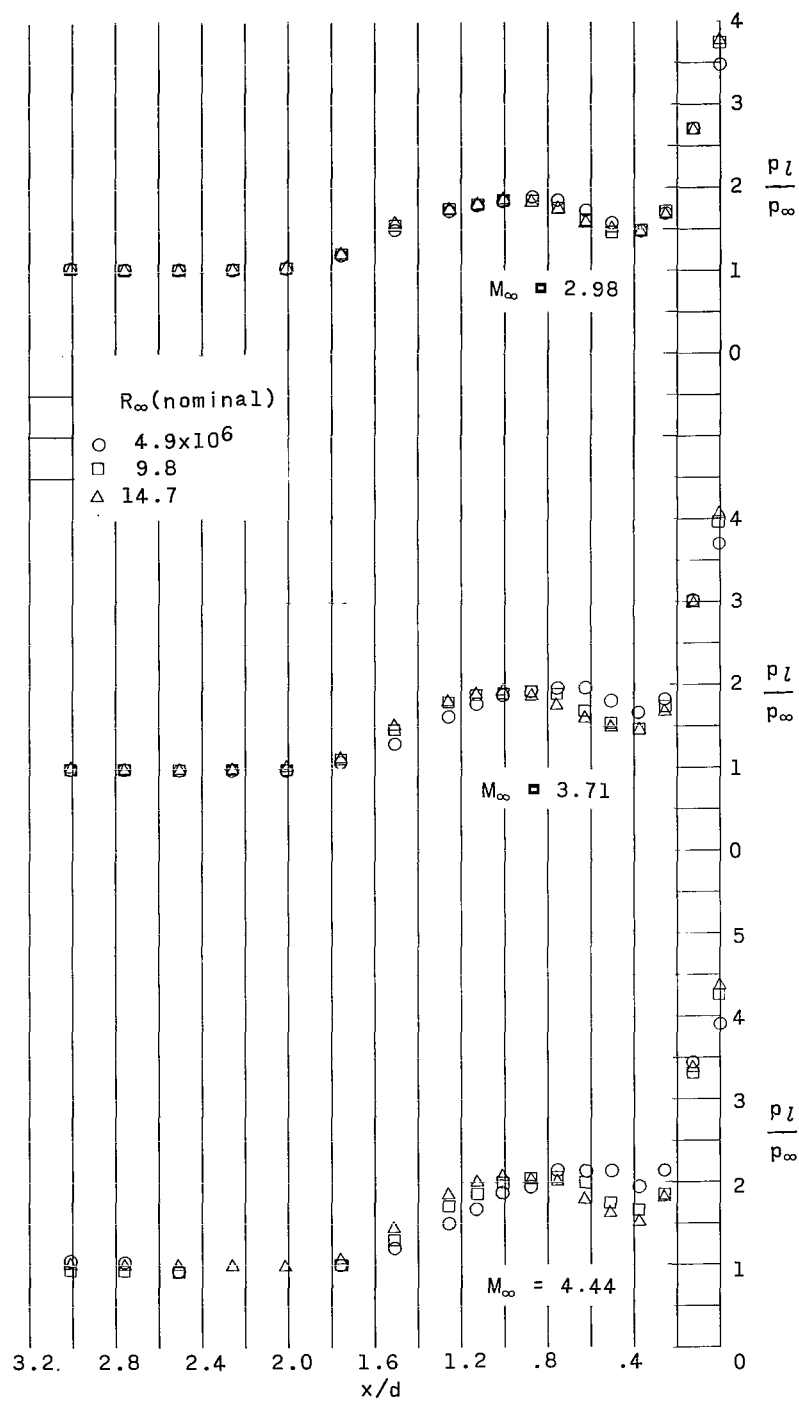
(a) Model 2; $d = 1.91$ cm; $\Lambda = 12.9^\circ$.

Figure 13.- Effect of Reynolds number on the pressure distribution upstream of models. $h = 25.40$ cm.



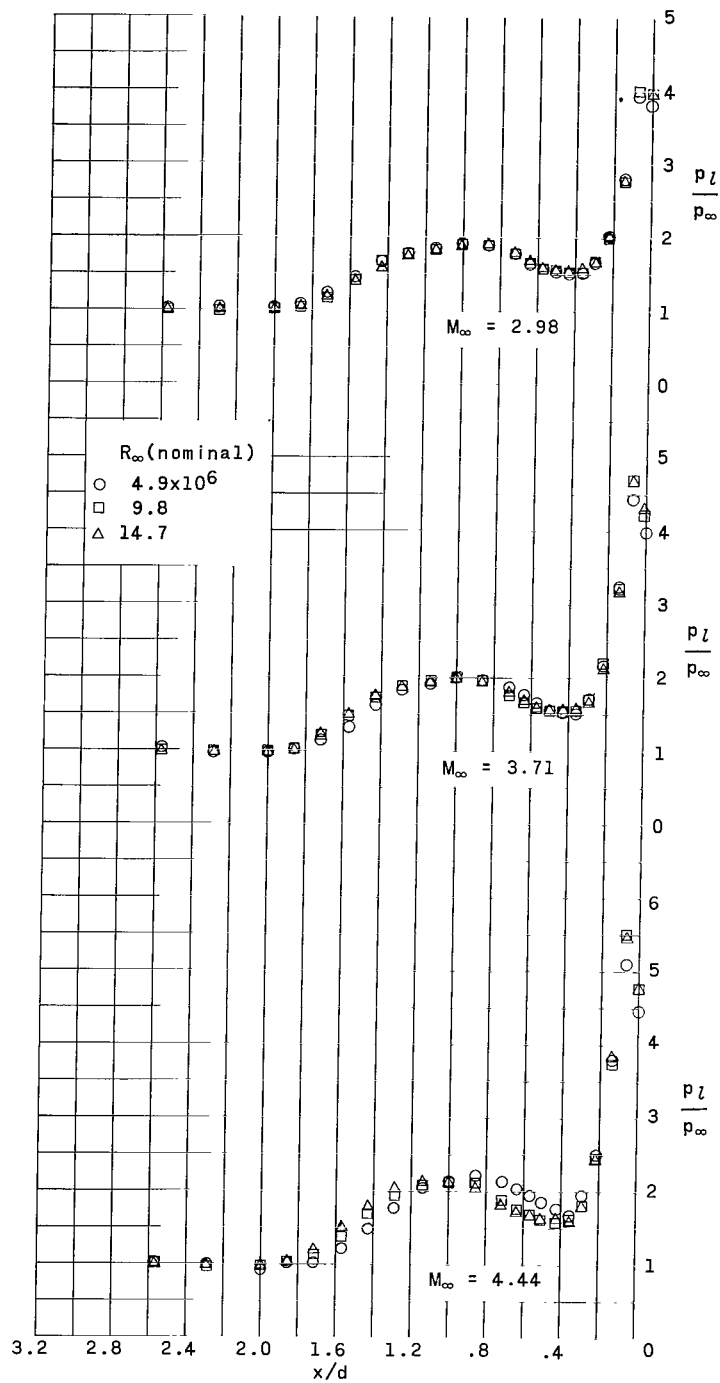
(b) Model 7; $d = 5.08$ cm; $\Lambda = 30^\circ$.

Figure 13.- Continued.



(c) Model 9; $d = 5.08$ cm; $\Lambda = 12.9^\circ$.

Figure 13.- Continued.



(d) Model 13; $d = 8.89$ cm; $\Lambda = 12.9^\circ$.

Figure 13.- Concluded.

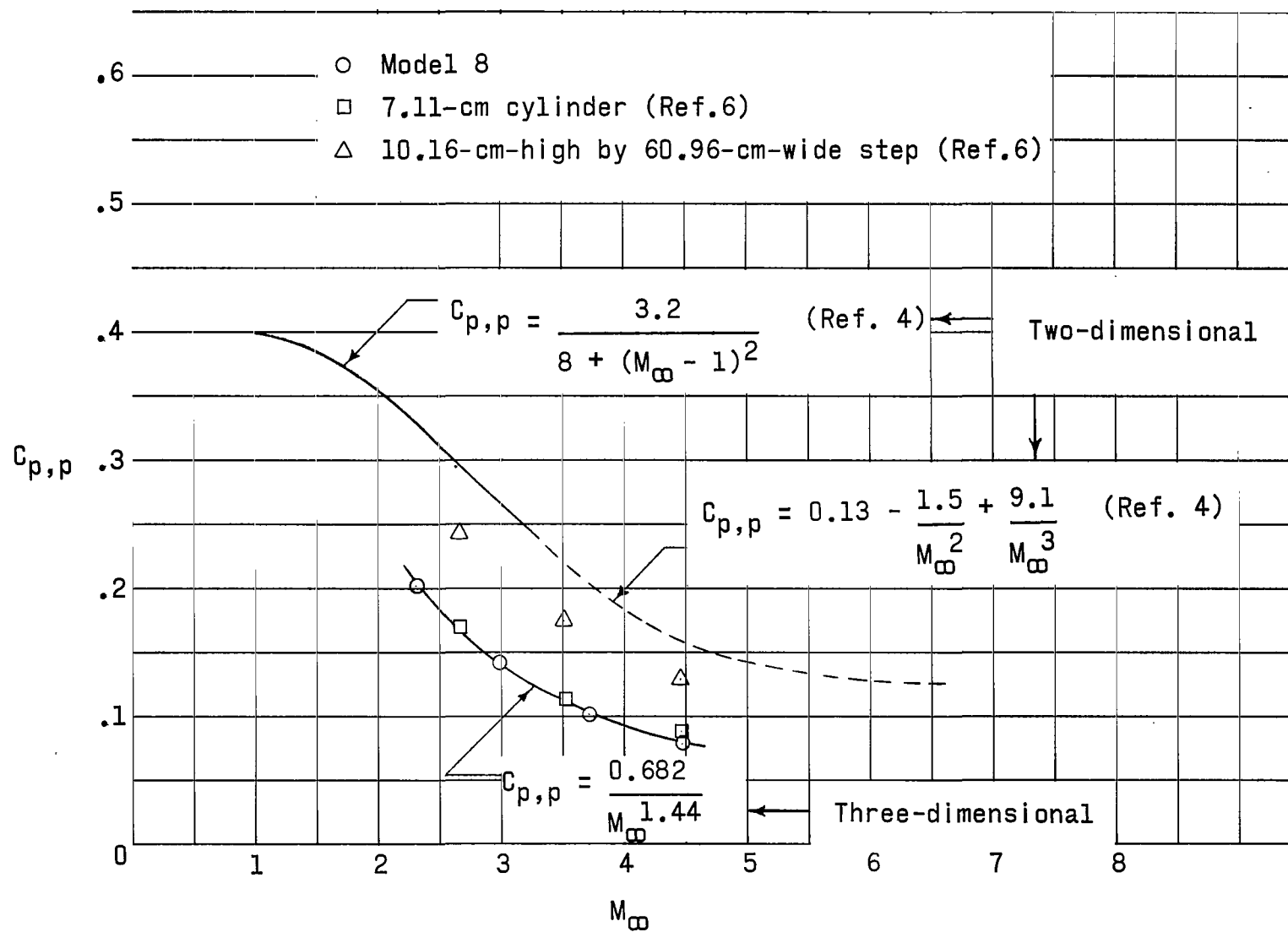


Figure 14.- Variation of first peak pressure coefficient with Mach number.

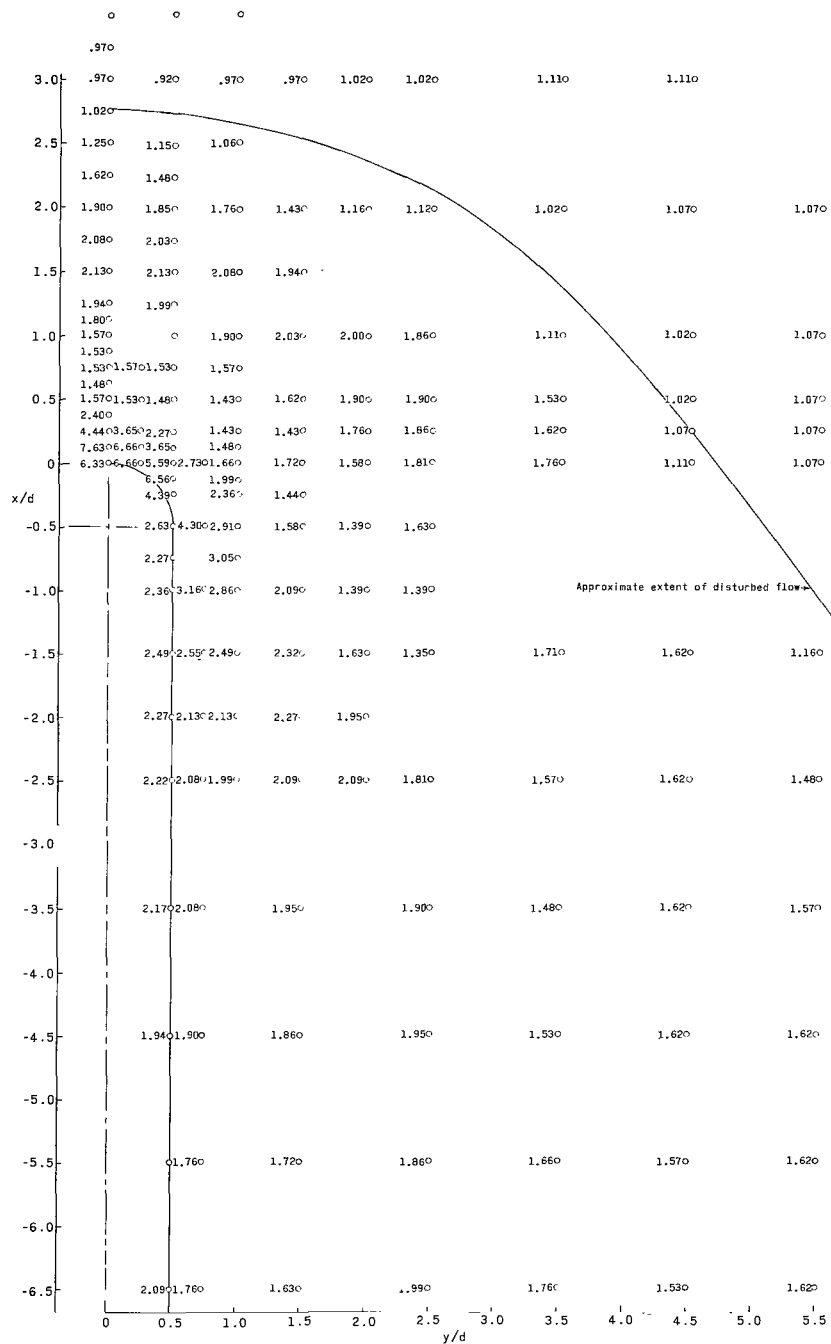


Figure 15.- Pressure distribution (p_t/p_∞) in the vicinity of model 8. $d = 5.08$ cm; $h = 25.40$ cm; $\Lambda = 0^\circ$; $M_\infty = 4.44$; $R_\infty = 9.5 \times 10^6$.

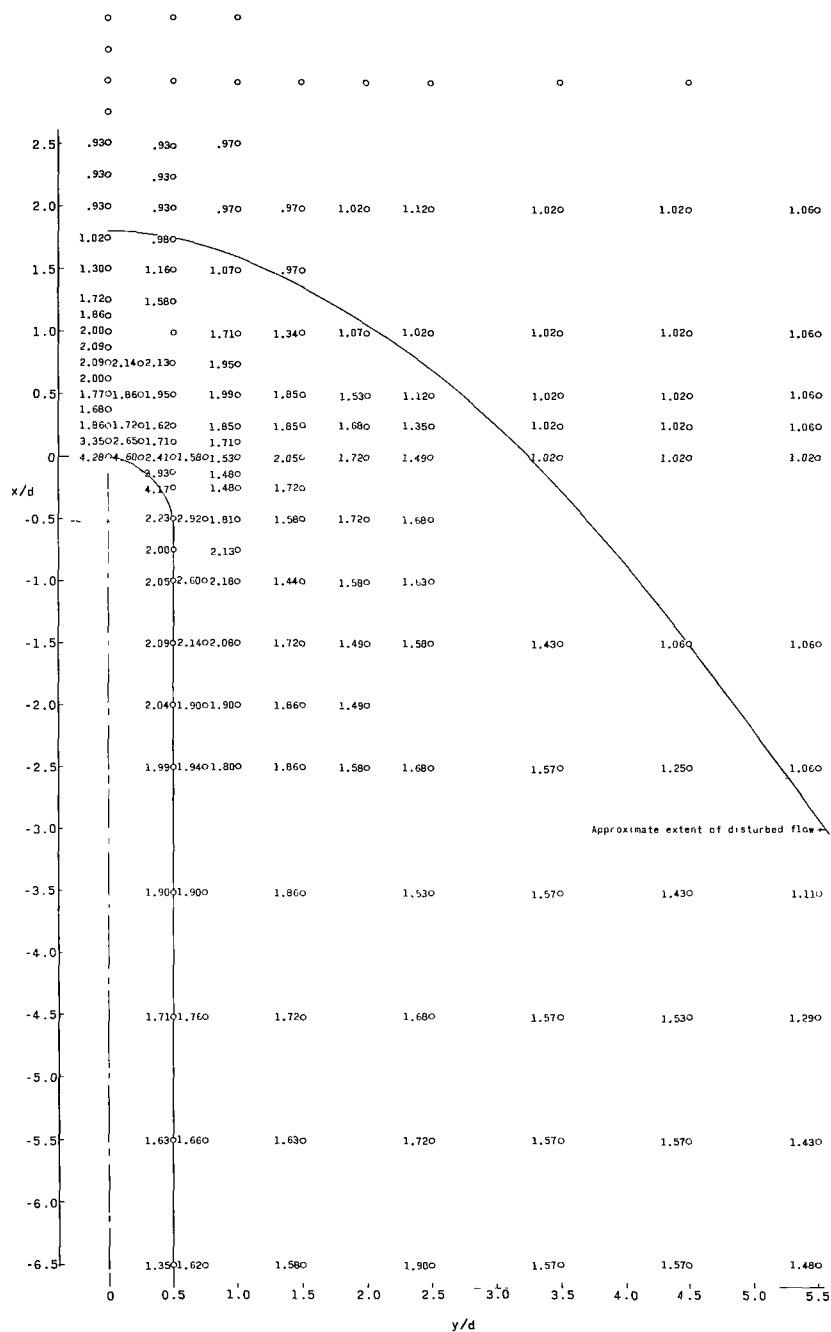


Figure 16.- Pressure distribution (p_1/p_∞) in the vicinity of model 9. $d = 5.08$ cm; $h = 25.40$ cm; $\Lambda = 12.9^\circ$; $M_\infty = 4.44$; $R_\infty = 9.5 \times 10^6$.

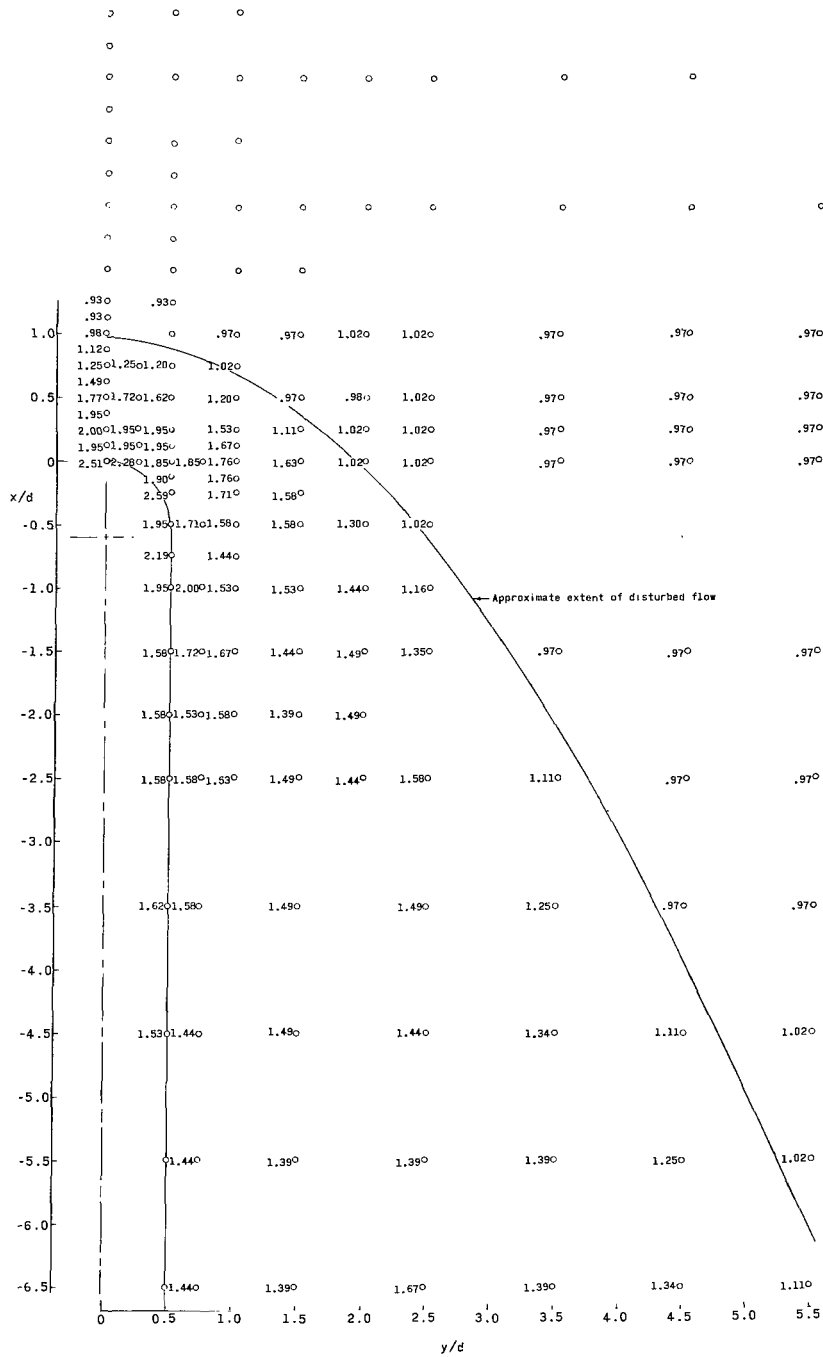


Figure 17.- Pressure distribution (p_t/p_∞) in the vicinity of model 7. $d = 5.08$ cm; $h = 25.40$ cm; $\Lambda = 30^\circ$; $M_\infty = 4.44$; $R_\infty = 9.5 \times 10^6$.

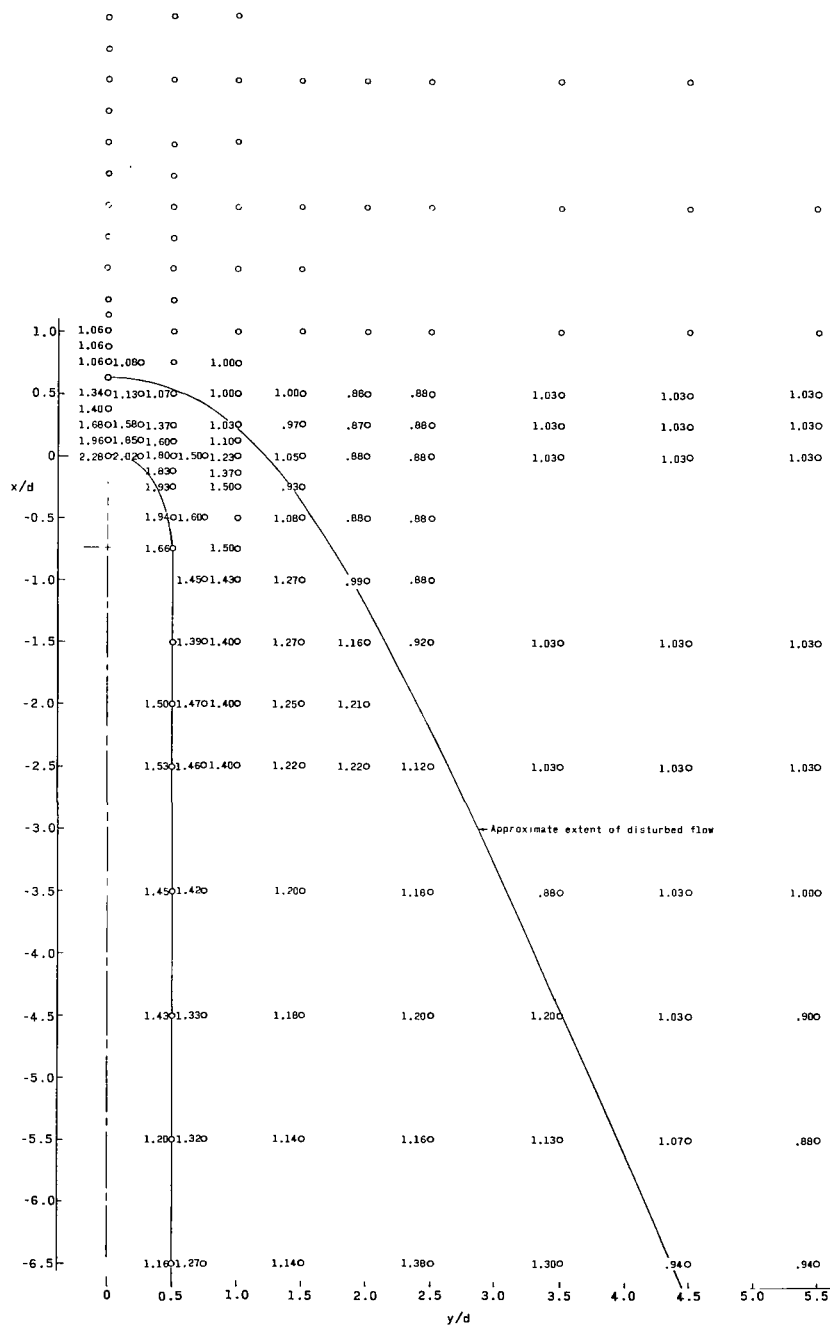


Figure 18.- Pressure distribution (p_t/p_∞) in the vicinity of model 10. $d = 5.08$ cm; $h = 25.40$ cm; $\Lambda = 45^\circ$; $M_\infty = 4.44$; $R_\infty = 9.5 \times 10^6$.

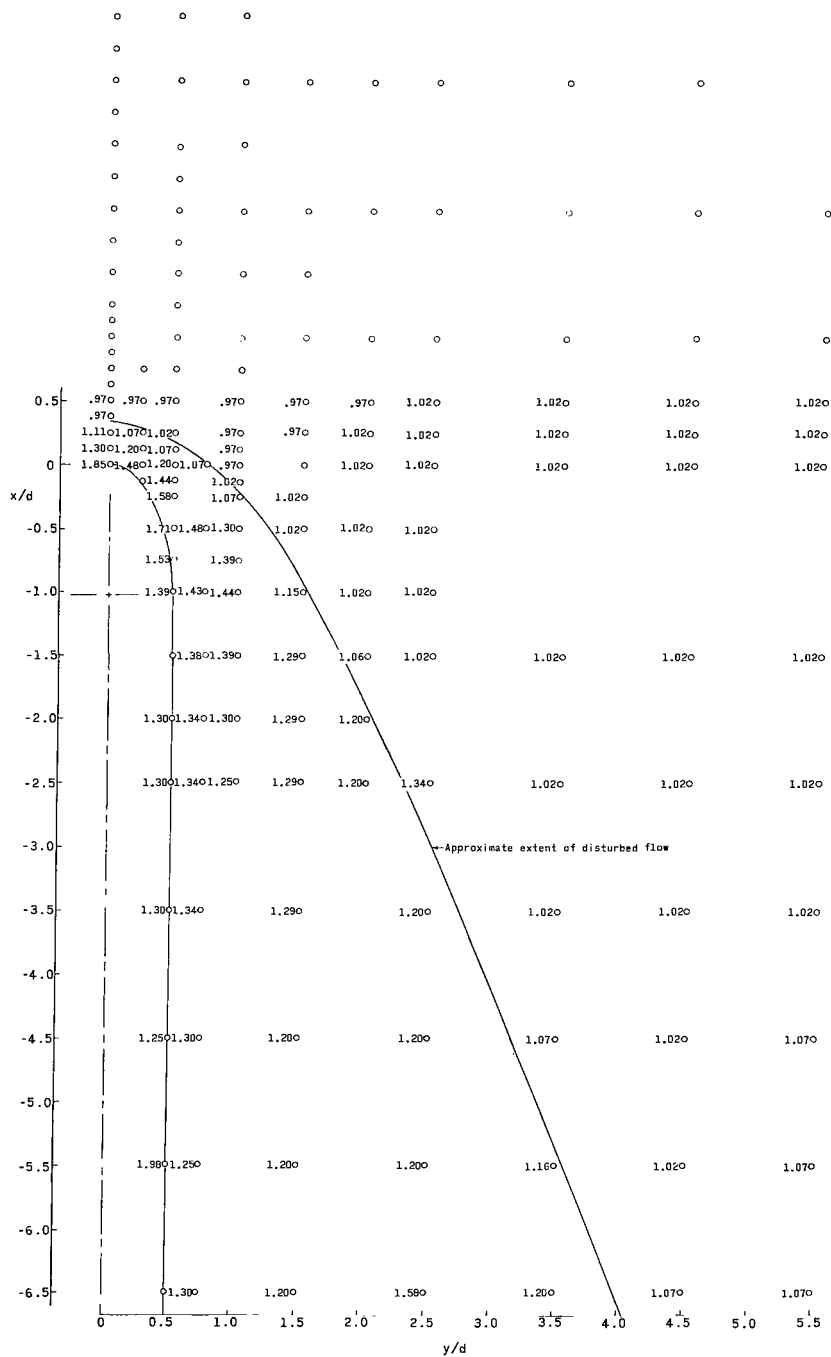


Figure 19.- Pressure distribution (p_t/p_∞) in the vicinity of model 11. $d = 5.08$ cm; $h = 25.40$ cm; $\Lambda = 60^\circ$; $M_\infty = 4.44$; $R_\infty = 9.5 \times 10^6$.

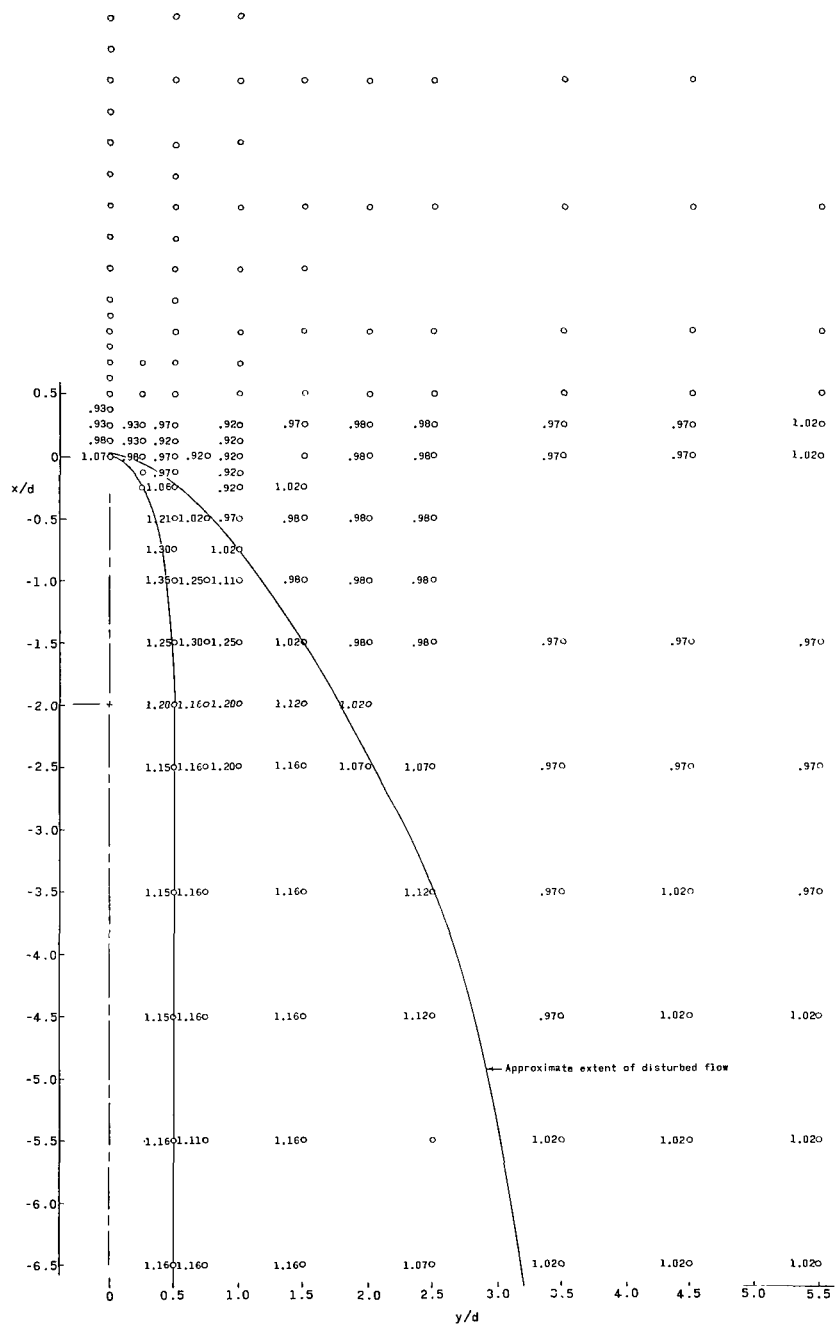


Figure 20.- Pressure distribution (p_t/p_∞) in the vicinity of model 12. $d = 5.08$ cm; $h = 15.24$ cm; $\Lambda = 75^\circ$; $M_\infty = 4.44$; $R_\infty = 9.4 \times 10^6$.

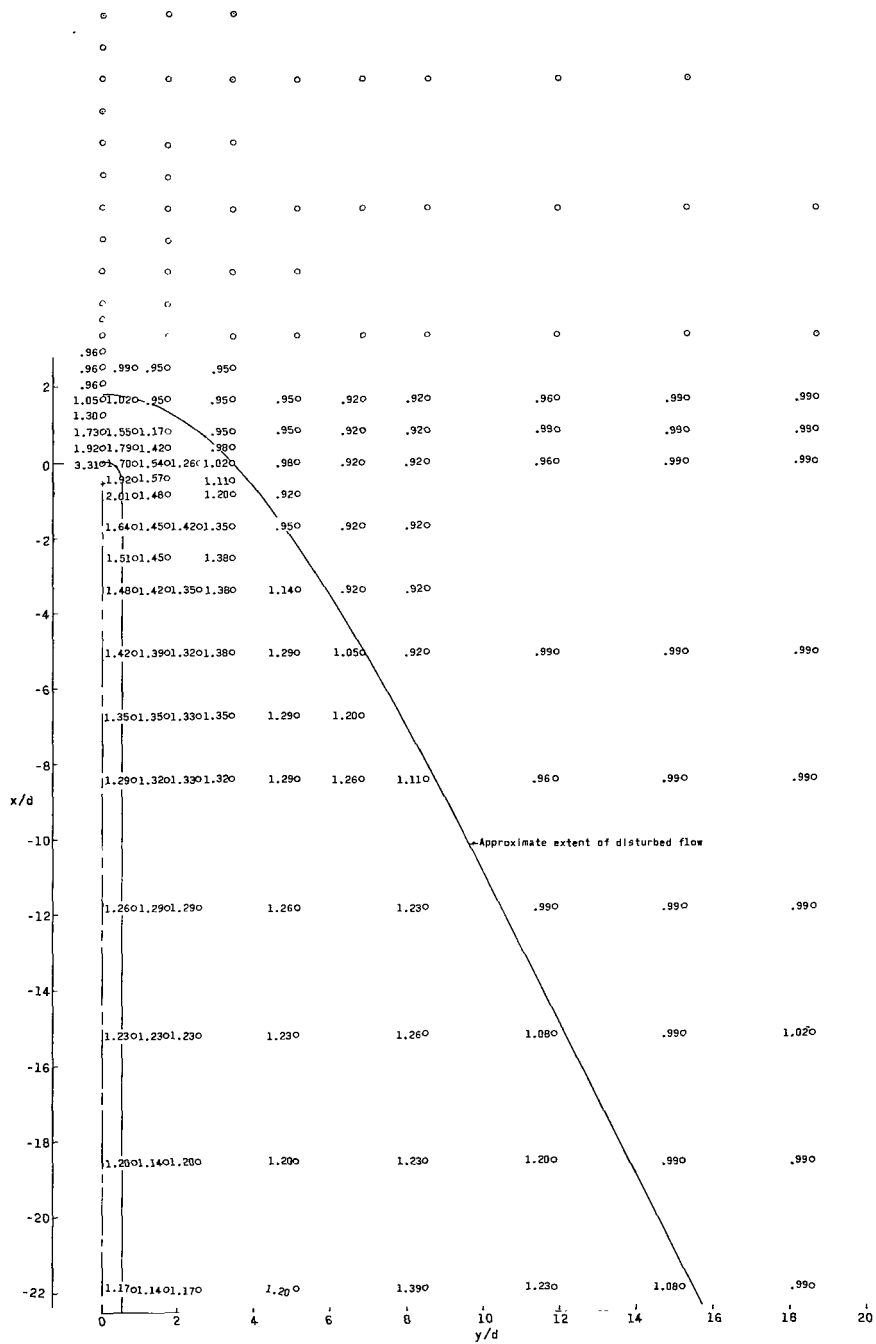


Figure 21.- Pressure distribution (p_t/p_∞) in the vicinity of model 1. $d = 1.47$ cm; $h = 25.40$ cm; $\Lambda = 12.9^\circ$; $M_\infty = 4.44$; $R_\infty = 14.2 \times 10^6$.

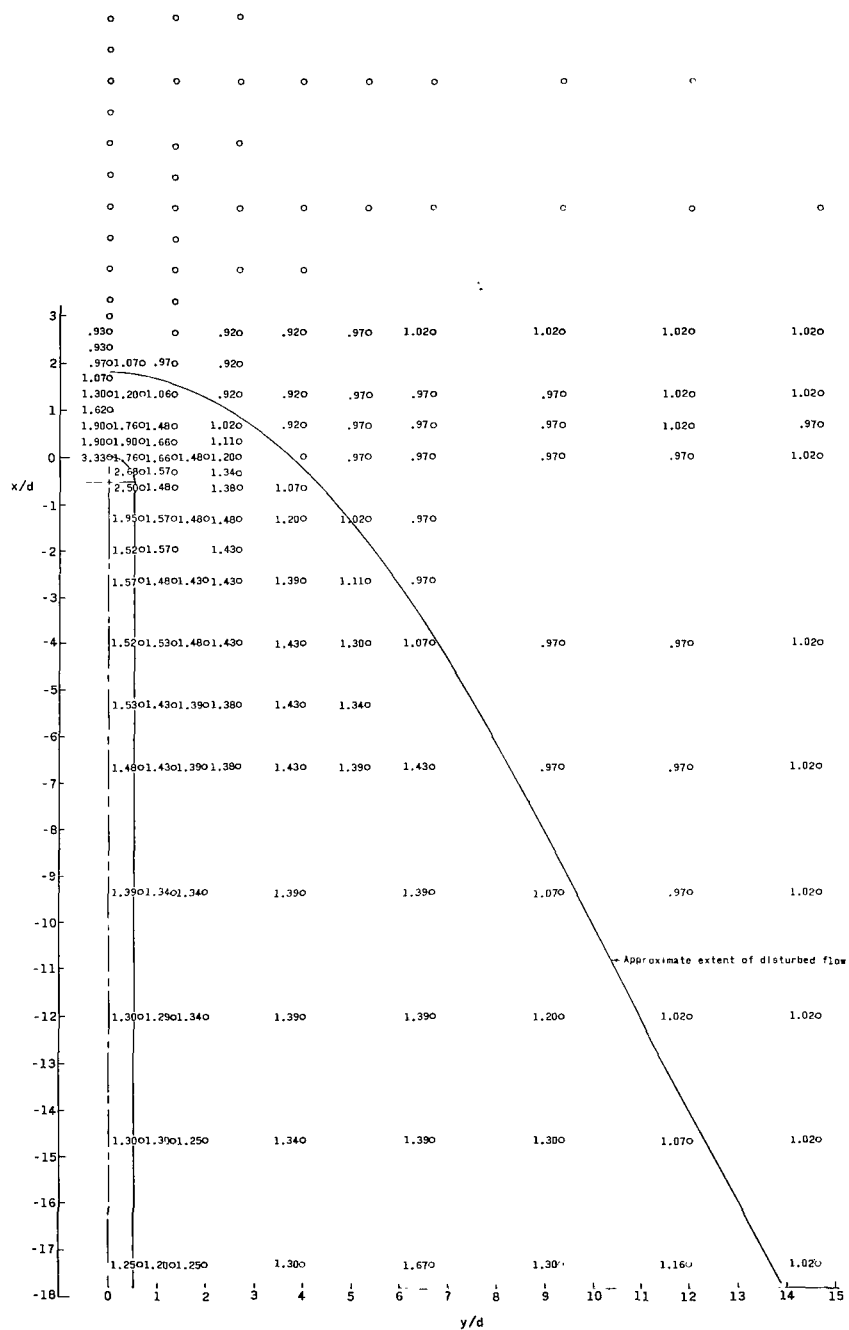


Figure 22.- Pressure distribution (p_t/p_∞) in the vicinity of model 2. $d = 1.91$ cm; $h = 25.40$ cm; $\Lambda = 12.9^\circ$; $M_\infty = 4.44$; $R_\infty = 9.5 \times 10^6$.

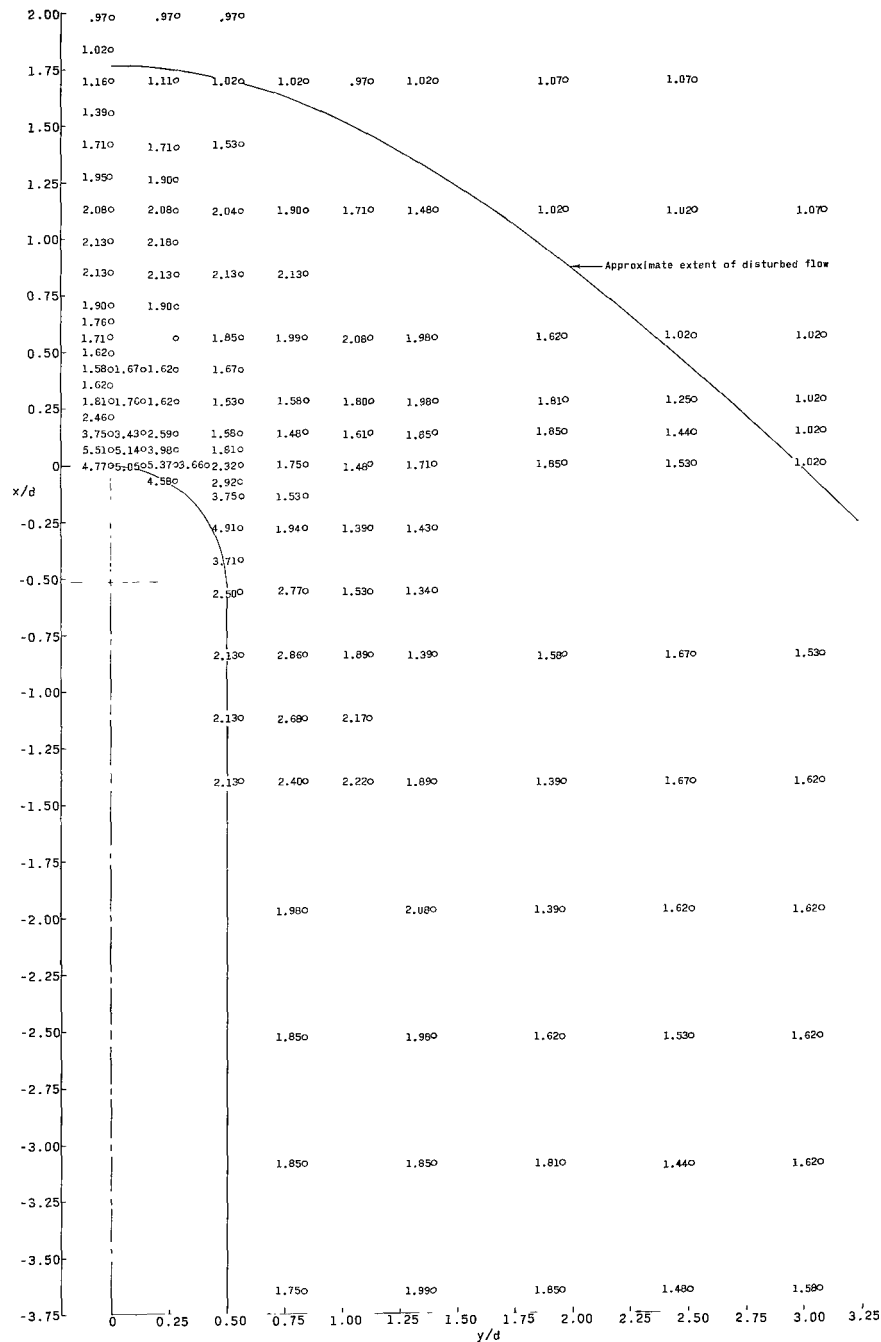


Figure 23.- Pressure distribution (p_t/p_∞) in the vicinity of model 13. $d = 8.89$ cm; $h = 25.40$ cm; $\Lambda = 12.9^\circ$; $M_\infty = 4.44$; $R_\infty = 9.5 \times 10^6$.

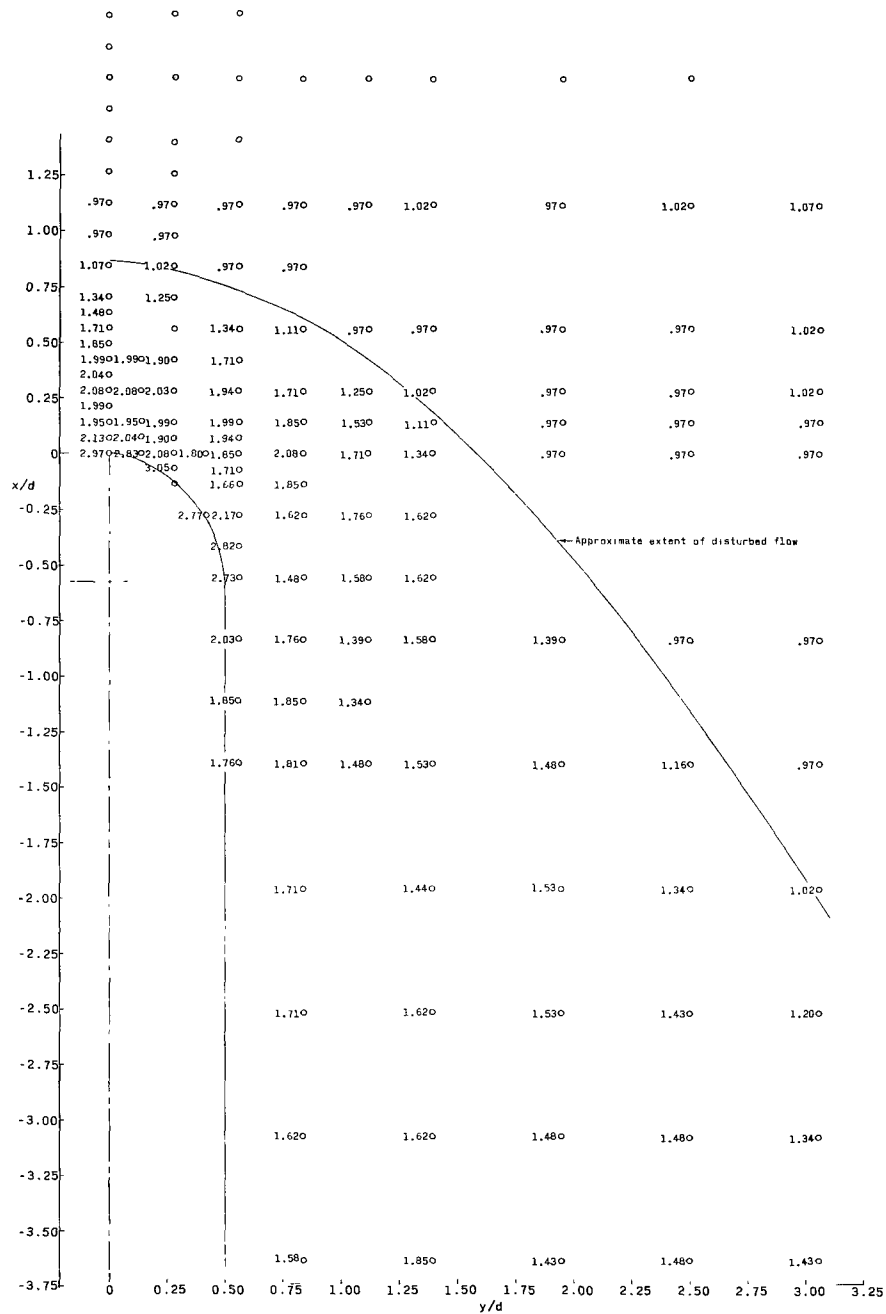


Figure 24.- Pressure distribution (p_t/p_∞) in the vicinity of model 14. $d = 8.89$ cm; $h = 25.40$ cm; $\Lambda = 30^\circ$; $M_\infty = 4.44$; $R_\infty = 9.5 \times 10^6$.

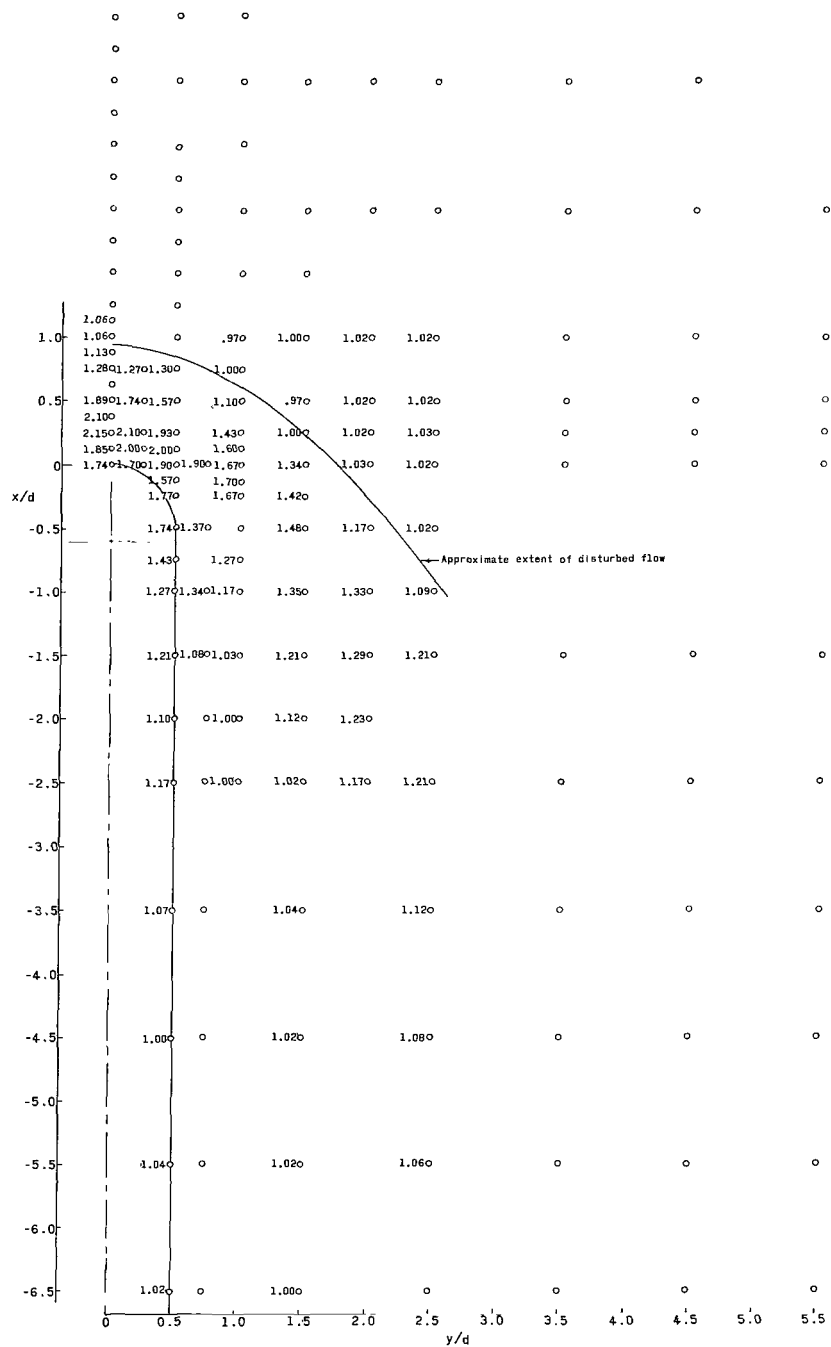


Figure 25.- Pressure distribution (p_t/p_∞) in the vicinity of model 3. $d = 5.08$ cm; $h = 2.54$ cm; $\Lambda = 30^\circ$; $M_\infty = 4.44$; $R_\infty = 9.5 \times 10^6$.

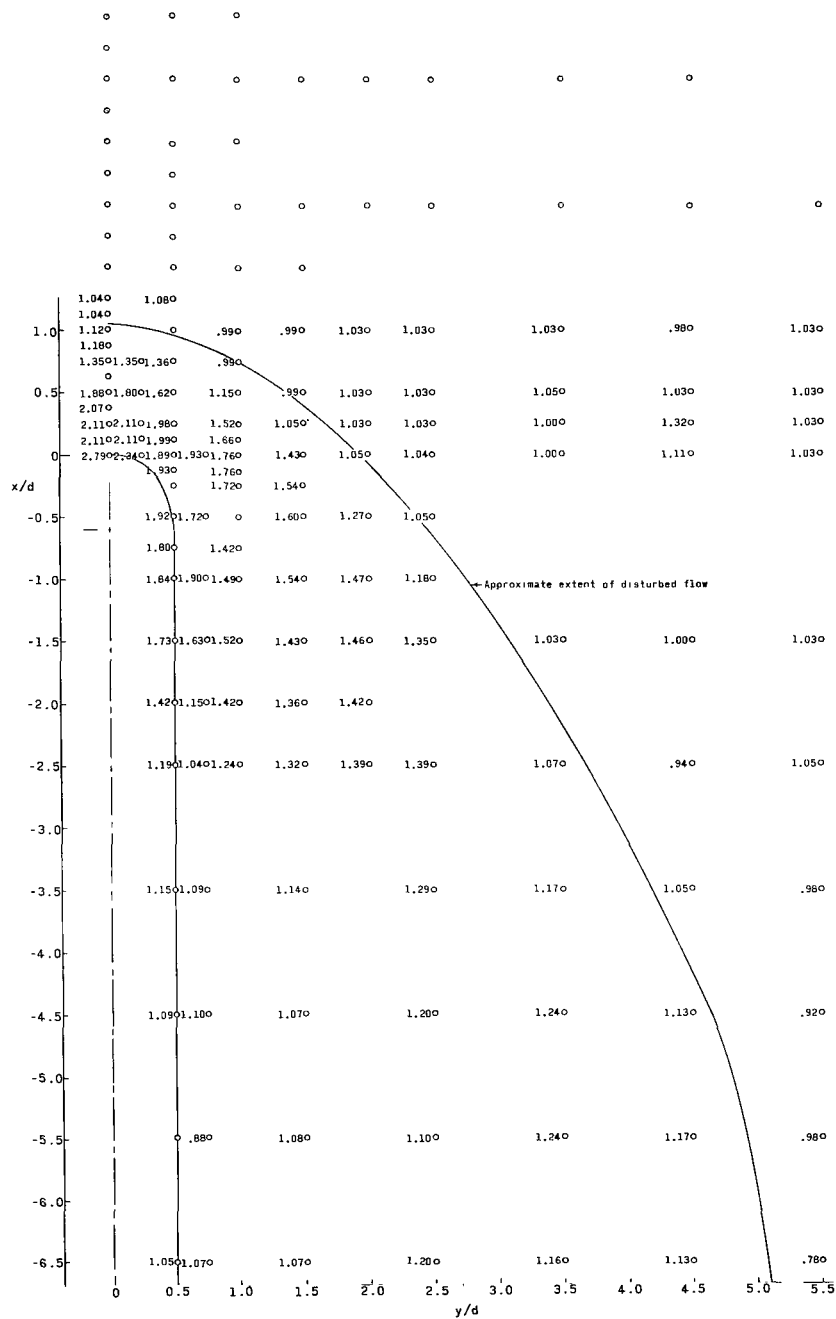


Figure 26.- Pressure distribution (p_t/p_∞) in the vicinity of model 4. $d = 5.08$ cm; $h = 5.08$ cm; $\Lambda = 30^\circ$; $M_\infty = 4.44$; $R_\infty = 9.5 \times 10^6$.

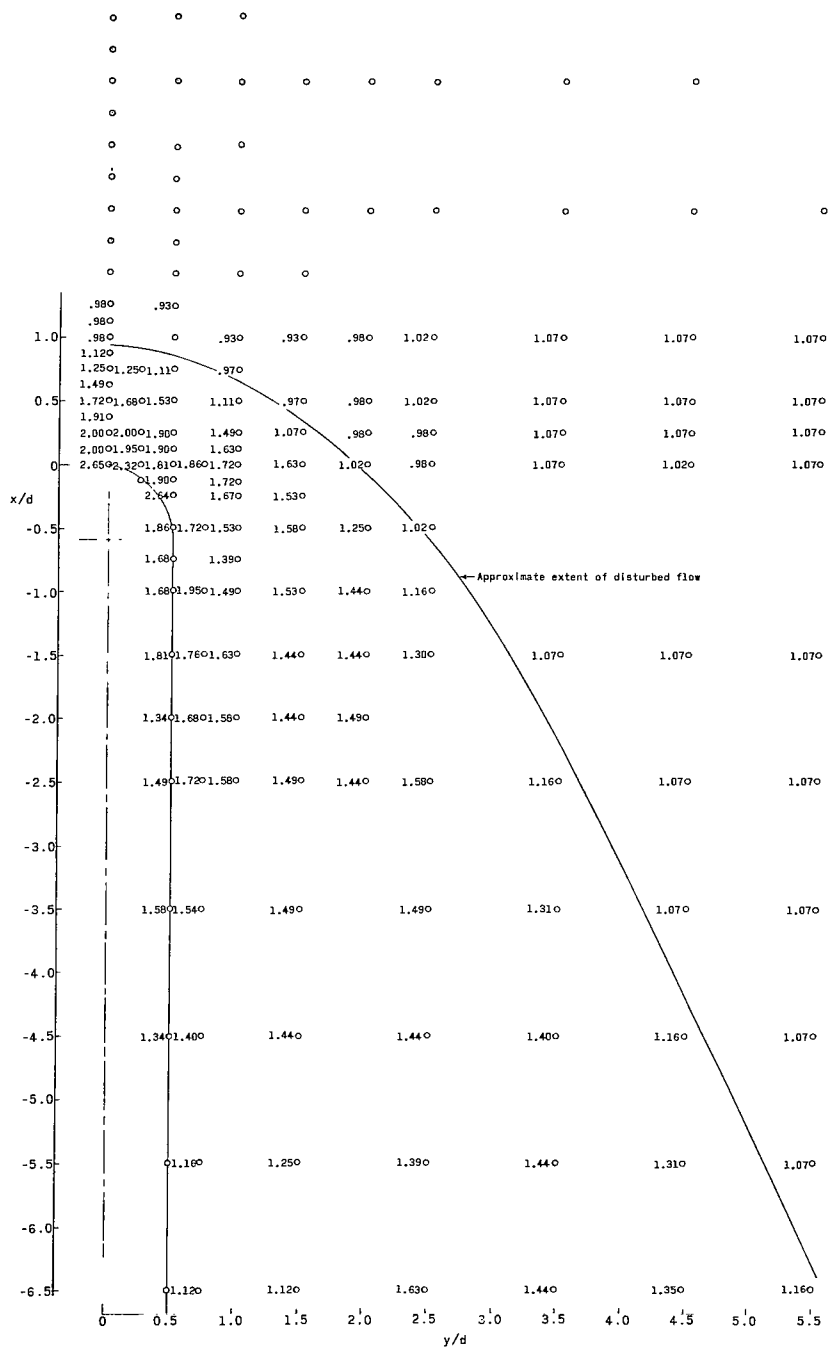


Figure 27.- Pressure distribution (p_t/p_∞) in the vicinity of model 5. $d = 5.08$ cm; $h = 10.16$ cm; $\Lambda = 30^\circ$; $M_\infty = 4.44$; $R_\infty = 9.5 \times 10^6$.

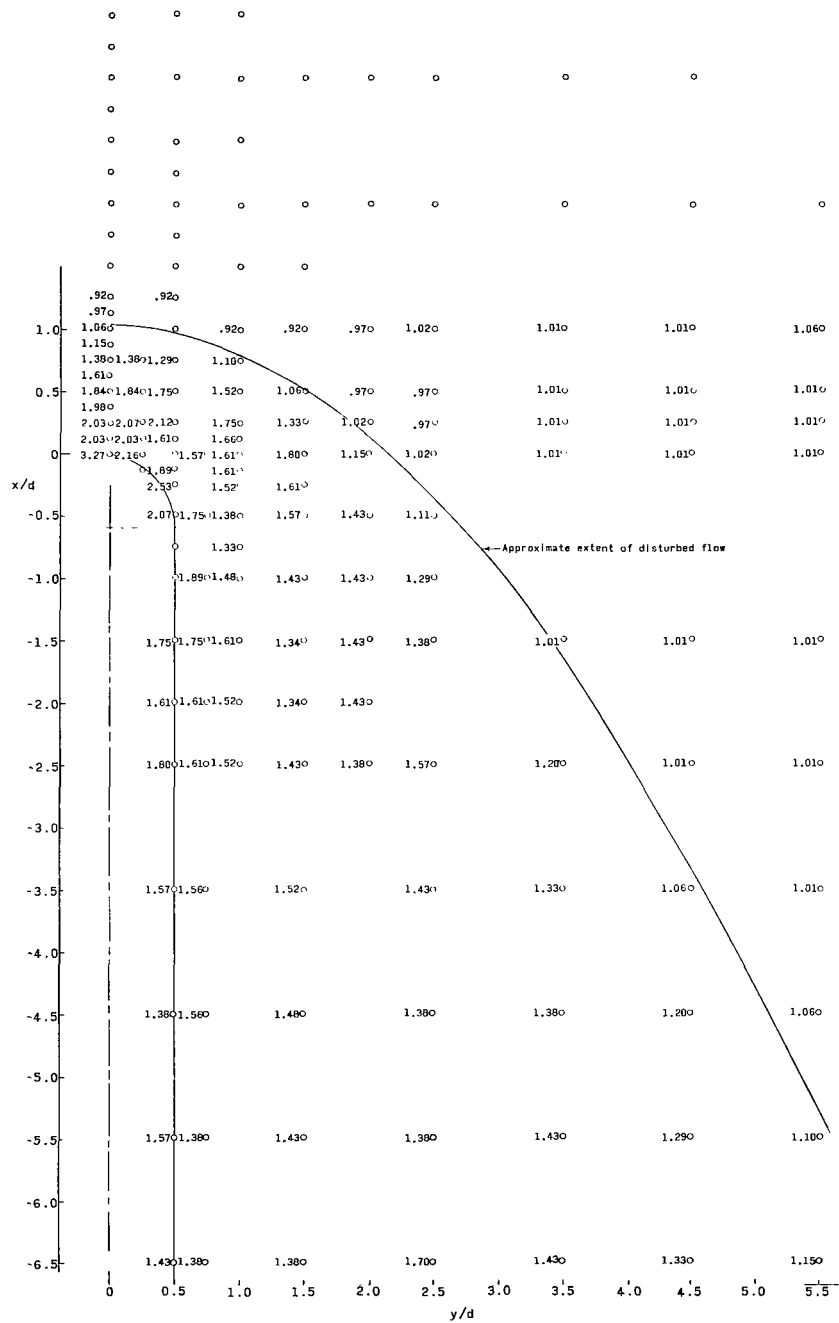
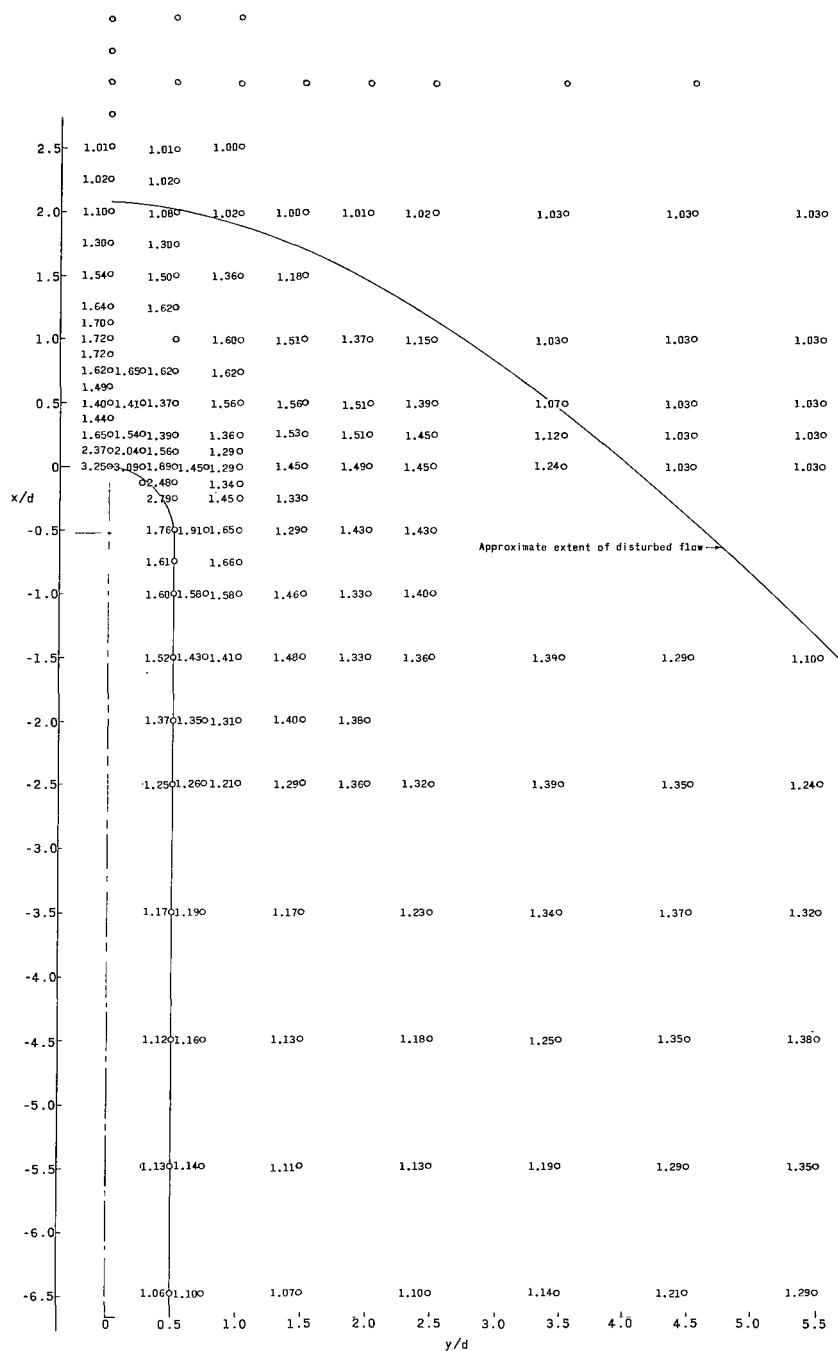
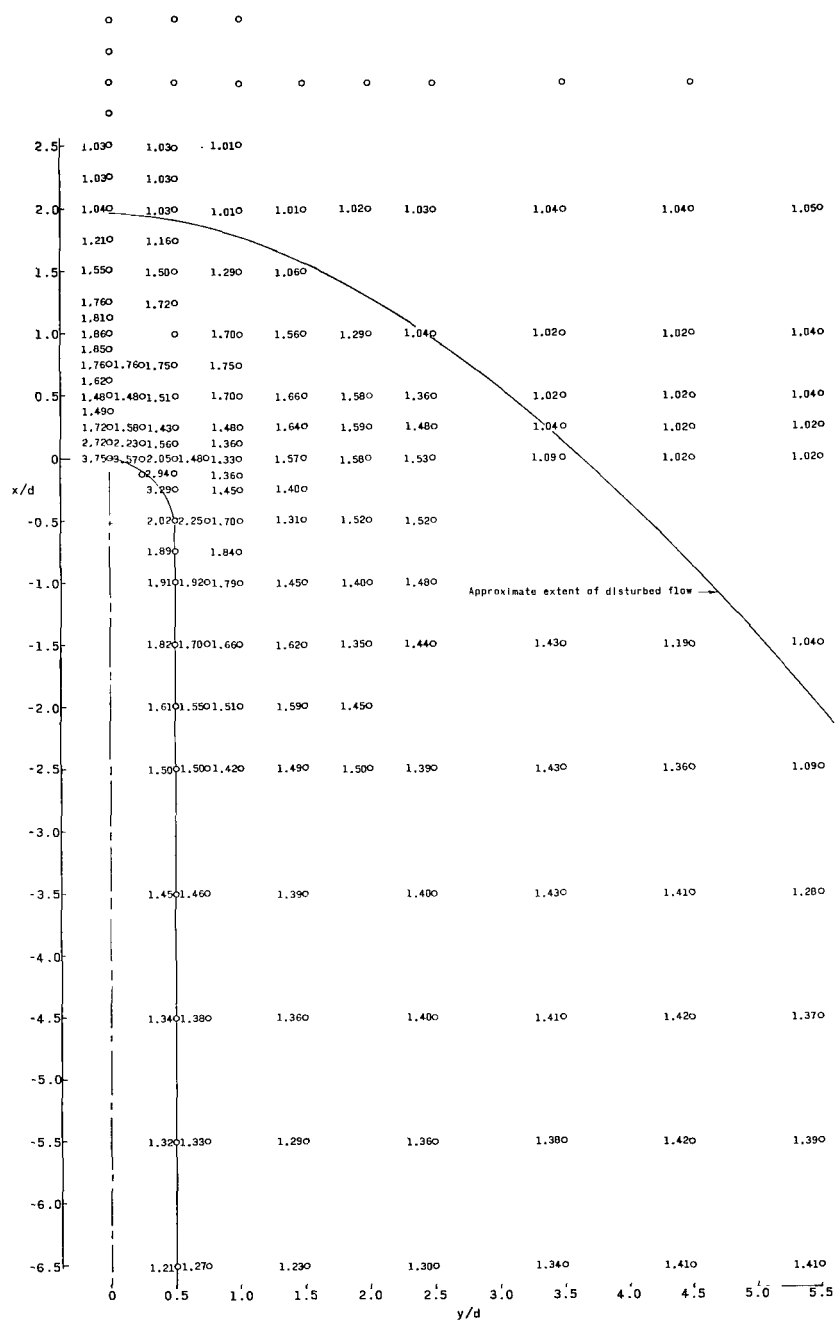


Figure 28.- Pressure distribution (p_t/p_∞) in the vicinity of model 6. $d = 5.08$ cm; $h = 15.24$ cm; $\Lambda = 30^\circ$; $M_\infty = 4.44$; $R_\infty = 9.5 \times 10^6$.



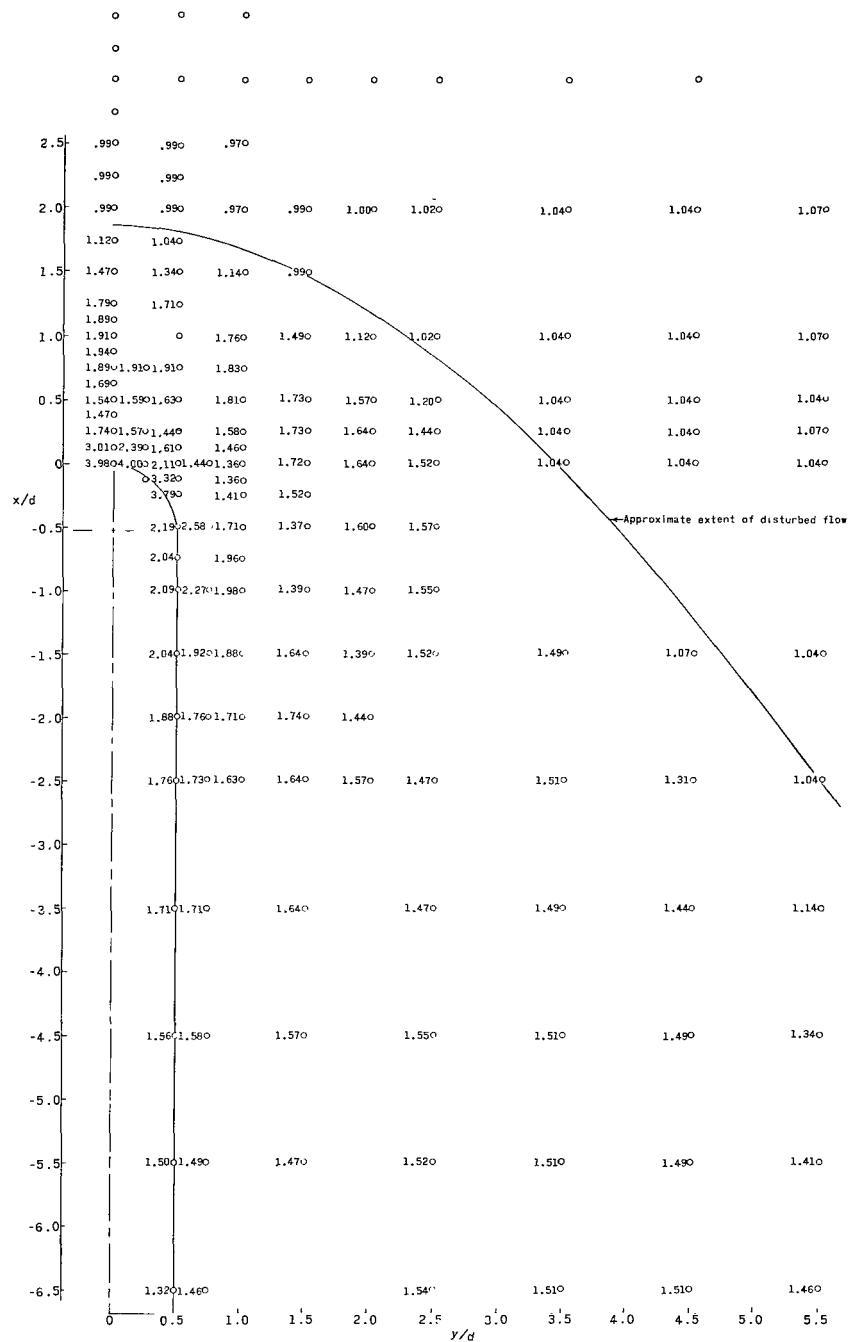
(a) $M_{\infty} = 2.30$.

Figure 29.- Pressure distribution (p_t/p_{∞}) in the vicinity of model 9 for various Mach numbers. $d = 5.08$ cm; $h = 25.40$ cm; $\Lambda = 12.9^\circ$; $R_{\infty} \approx 9.8 \times 10^6$.



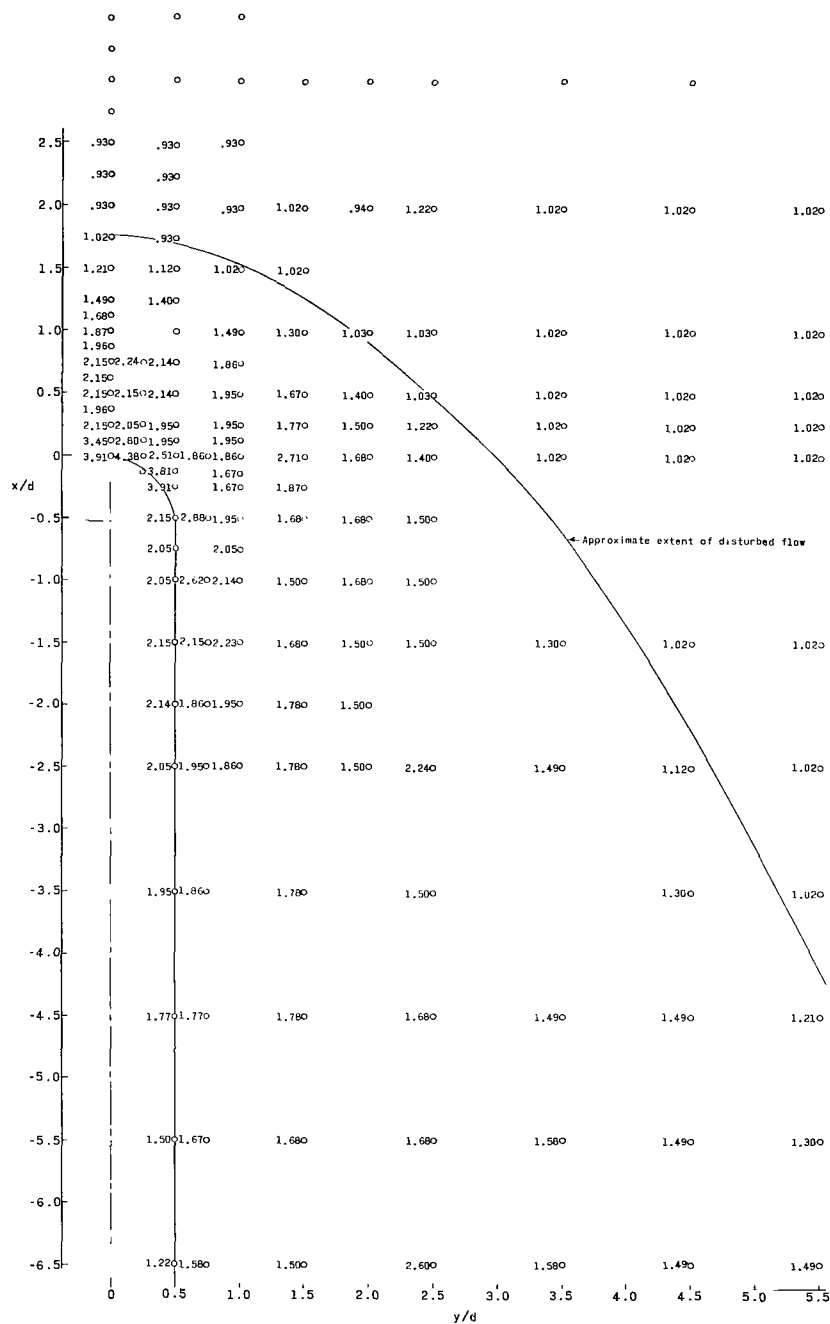
(b) $M_{\infty} = 2.98$.

Figure 29.- Continued.



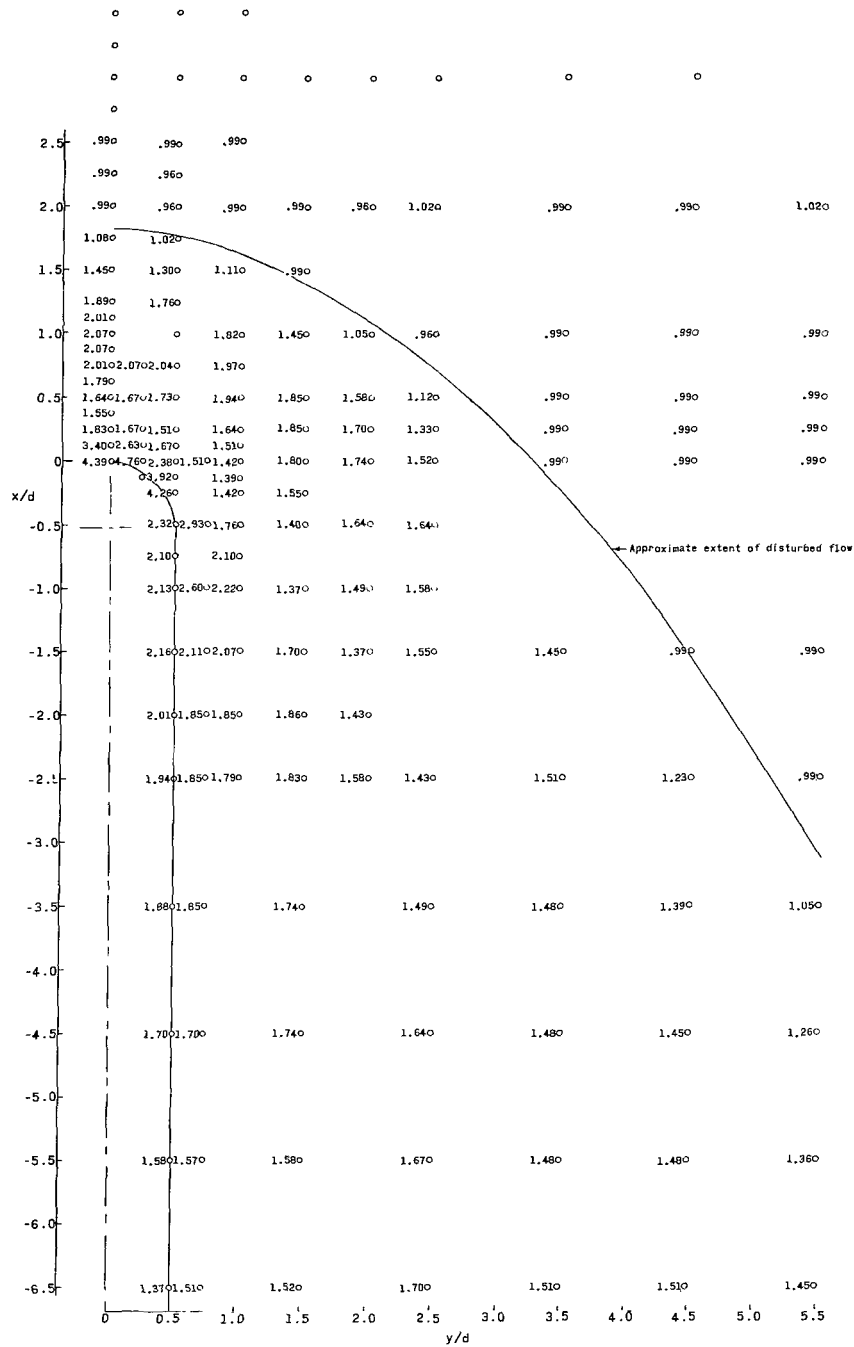
(c) $M_{\infty} = 3.71$.

Figure 29.- Concluded.



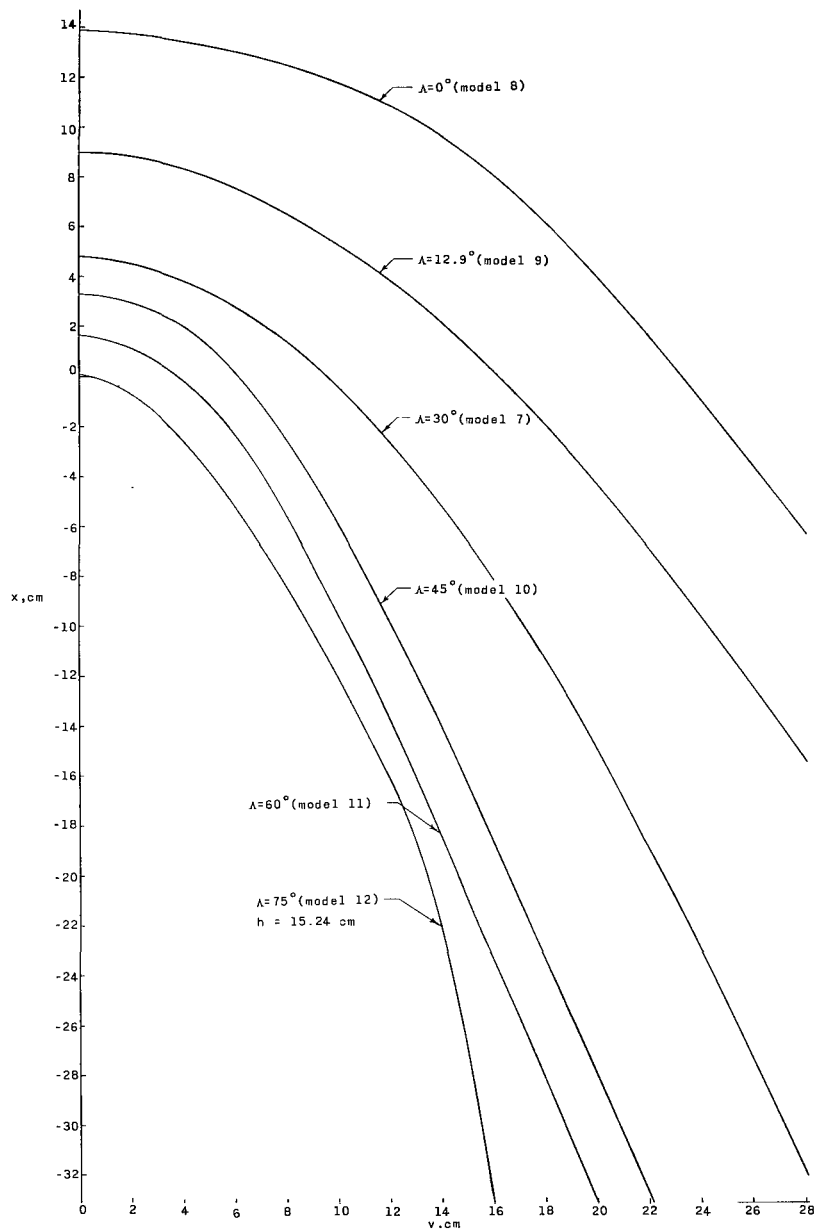
(a) $R_\infty = 4.7 \times 10^6$.

Figure 30.- Pressure distribution (p_t/p_∞) in the vicinity of model 9 for various Reynolds numbers. $d = 5.08$ cm; $h = 25.40$ cm; $\Lambda = 12.9^\circ$; $M_\infty = 4.44$.



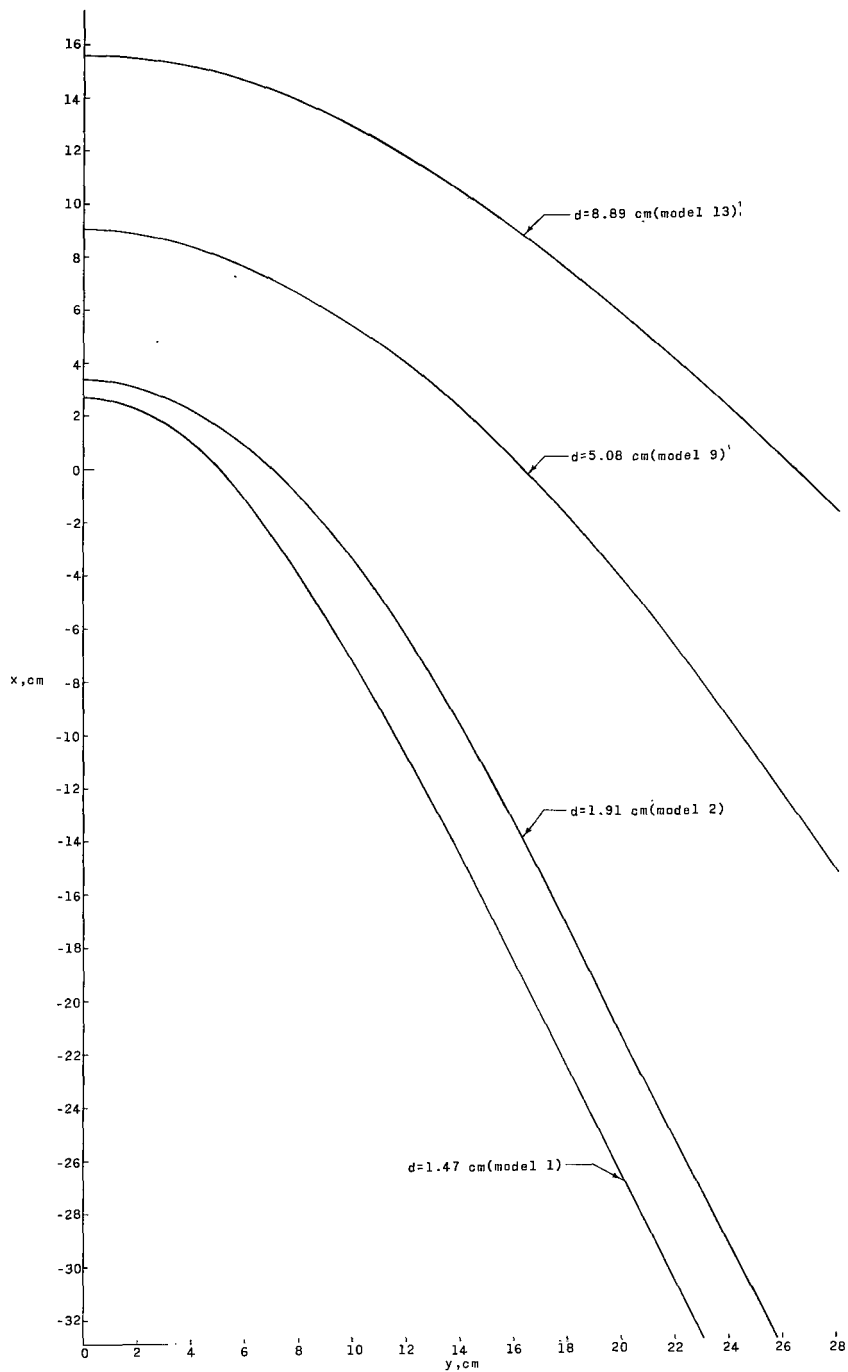
(b) $R_{\infty} = 14.2 \times 10^6$.

Figure 30. Concluded.



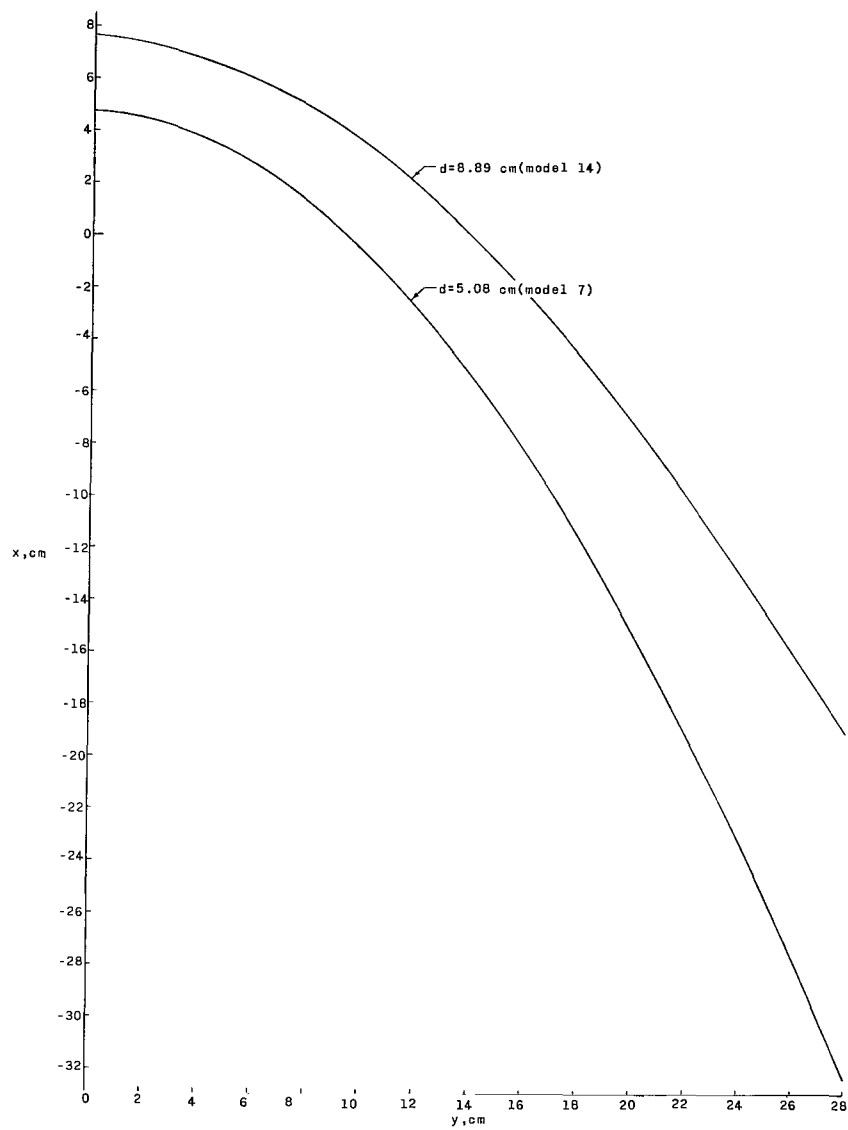
(a) Variation with sweep for $d = 5.08$ cm.

Figure 31.- Comparison of the extent of disturbed flow for various models. $M_\infty \approx 4.44$; $R_\infty \approx 9.8 \times 10^6$; $h = 25.40$ cm except for model 12.



(b) Variation with diameter for $\Lambda = 12.9^\circ$.

Figure 31.- Continued.



(c) Variation with diameter for $\Lambda \approx 30^\circ$.

Figure 31.- Concluded.

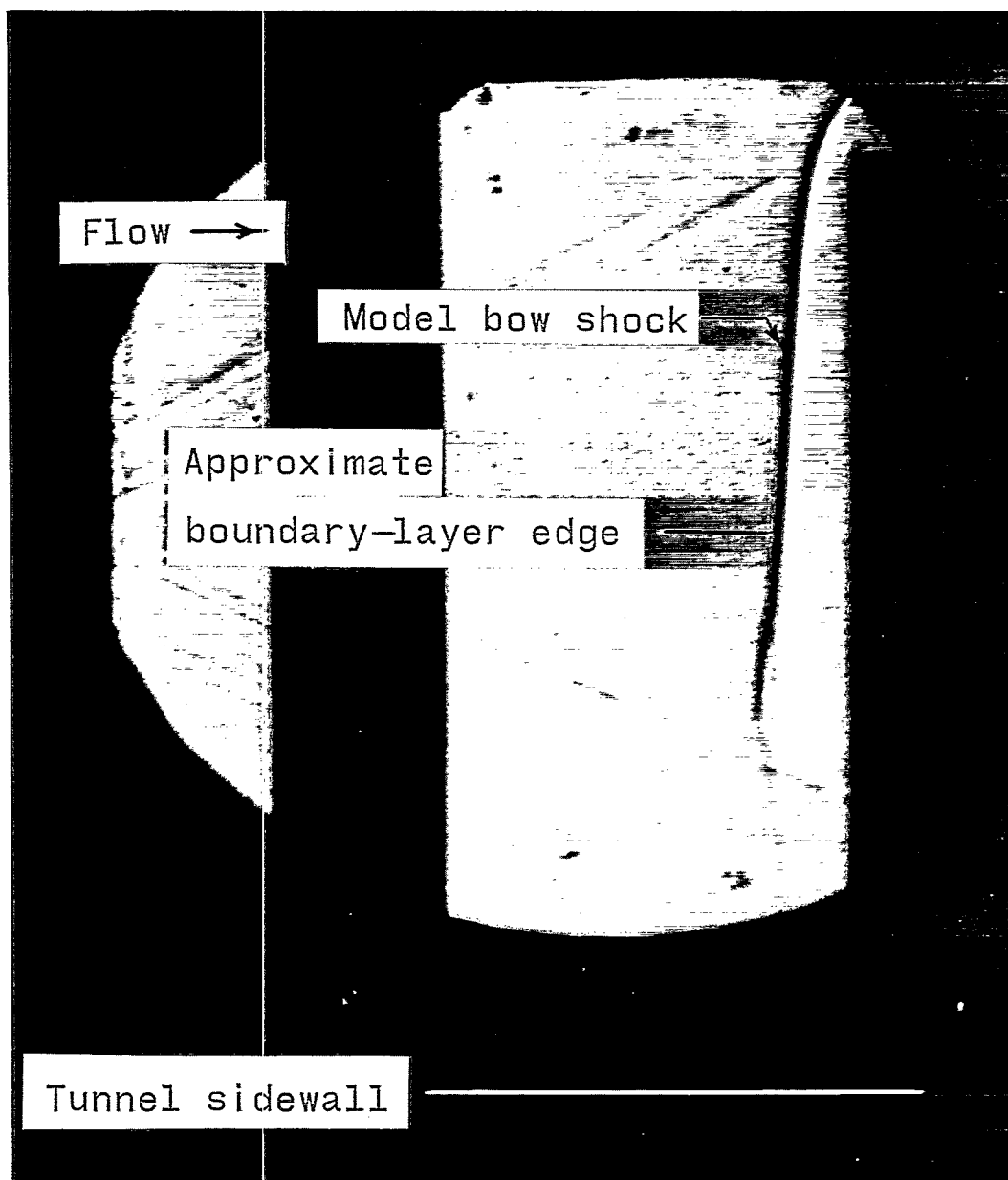


Figure 32.- Shadowgraph of the interaction region for model 8. $M_{\infty} = 2.98$; $R_{\infty} \approx 9.8 \times 10^6$.

L-66-7625



Tunnel
sidewall

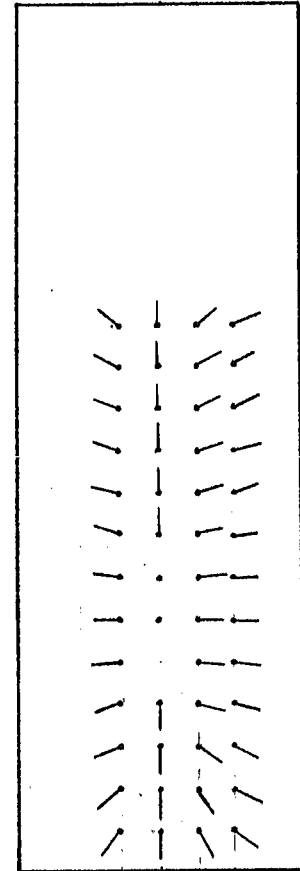
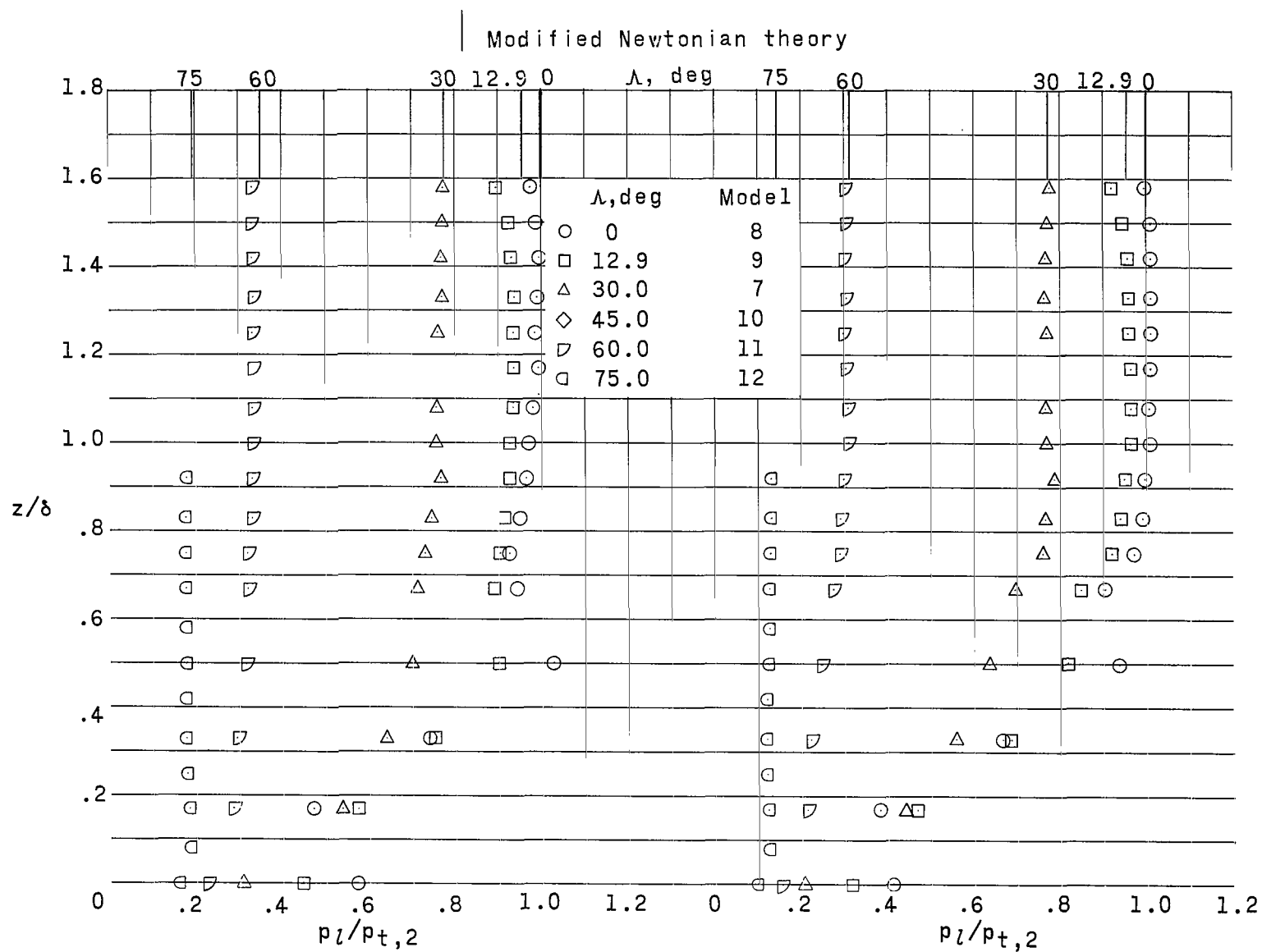
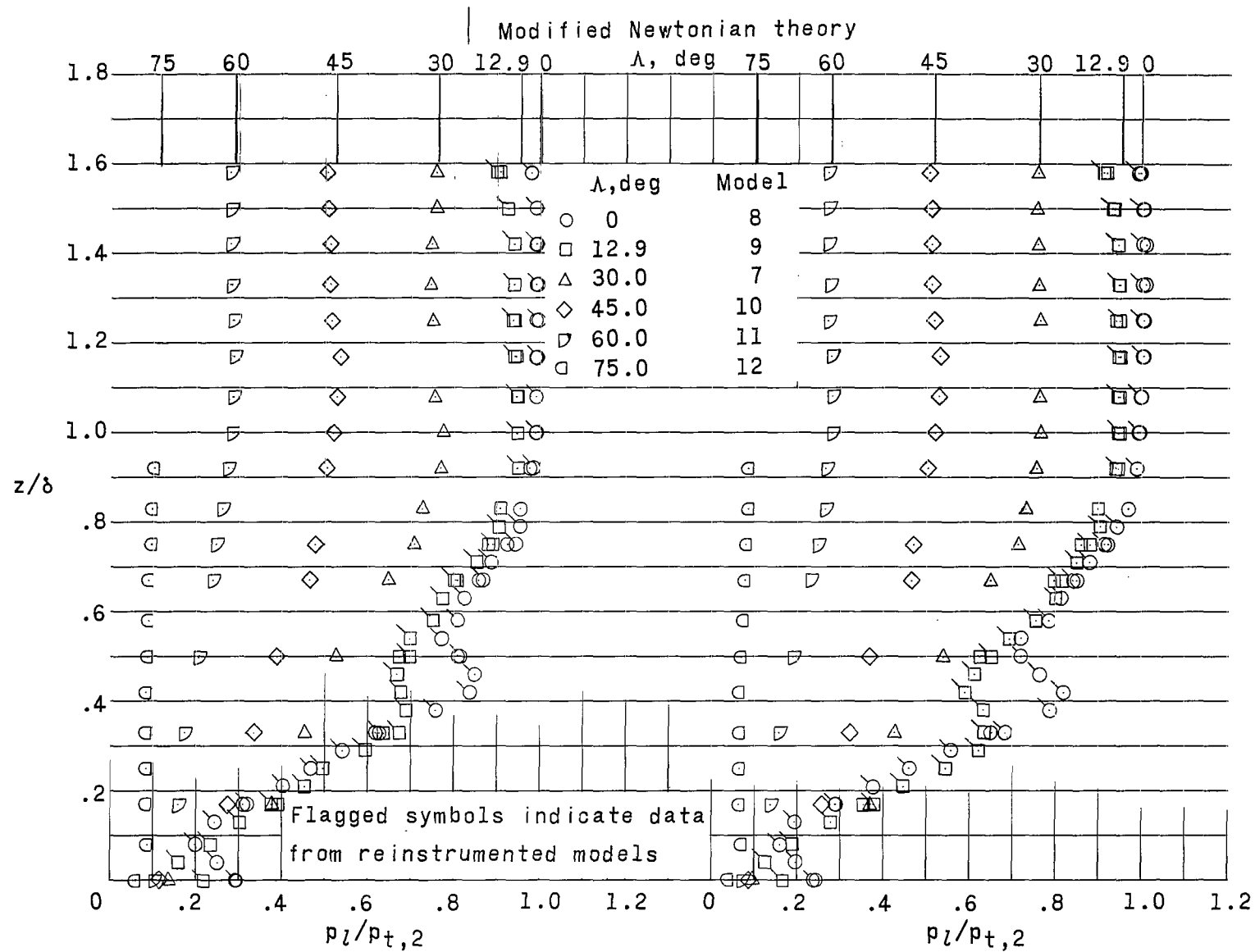


Figure 33.- Tuft study on model 13. $M_{\infty} = 3.71$; $R_{\infty} \approx 9.8 \times 10^6$.

L-66-7626

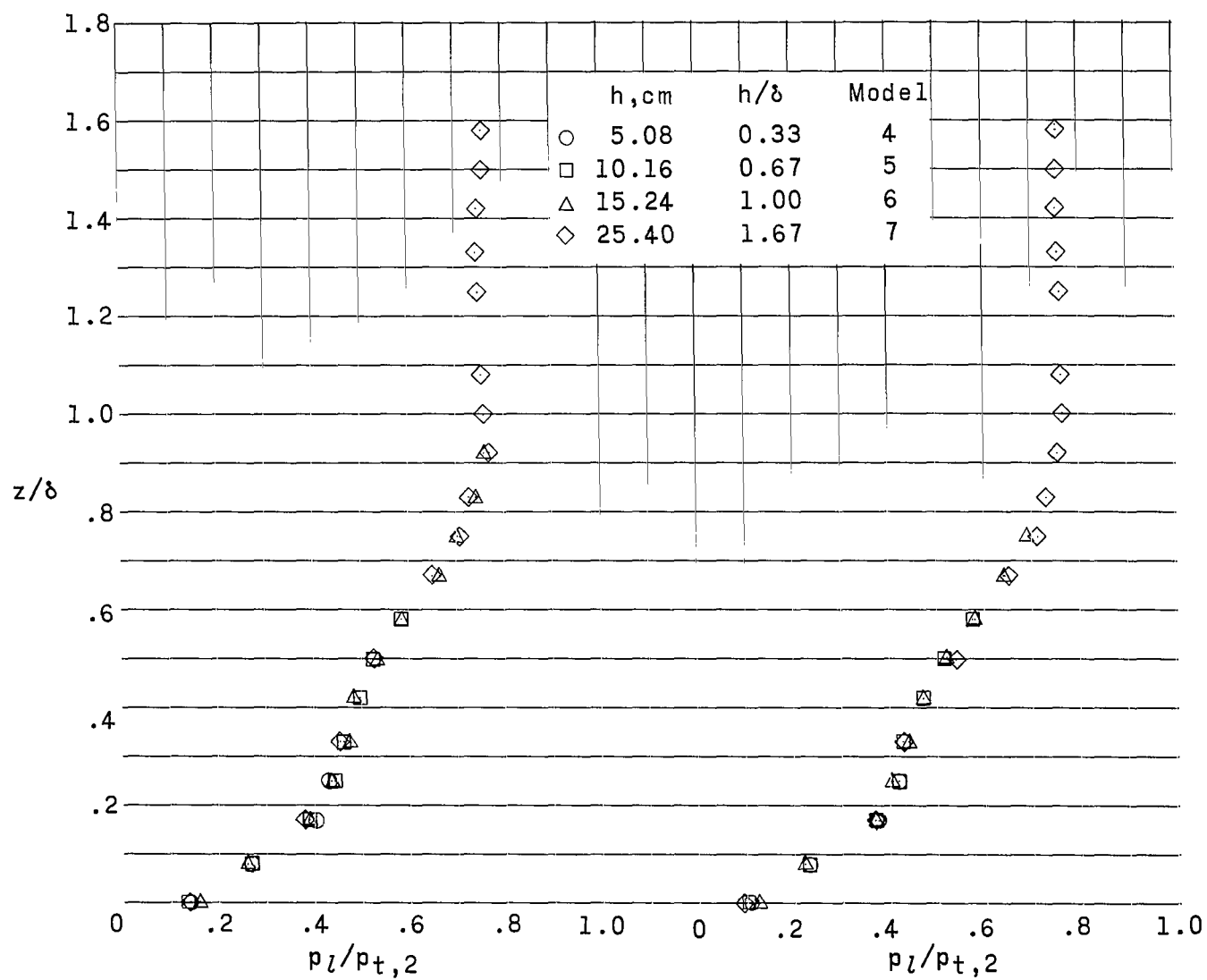
(a) $M_\infty = 2.30$.(b) $M_\infty = 2.98$.Figure 34.- Effect of sweep on the model stagnation line pressure distribution. $R_\infty \approx 9.8 \times 10^6$; $d = 5.08$ cm.



(c) $M_\infty = 3.71$.

(d) $M_\infty = 4.44$.

Figure 34.- Concluded.

(a) $M_\infty = 3.71$.(b) $M_\infty = 4.44$.Figure 35.- Effect of model height on the model stagnation line pressure distribution. $\Lambda = 30^\circ$; $d = 5.08$ cm; $R_\infty \approx 9.8 \times 10^6$.

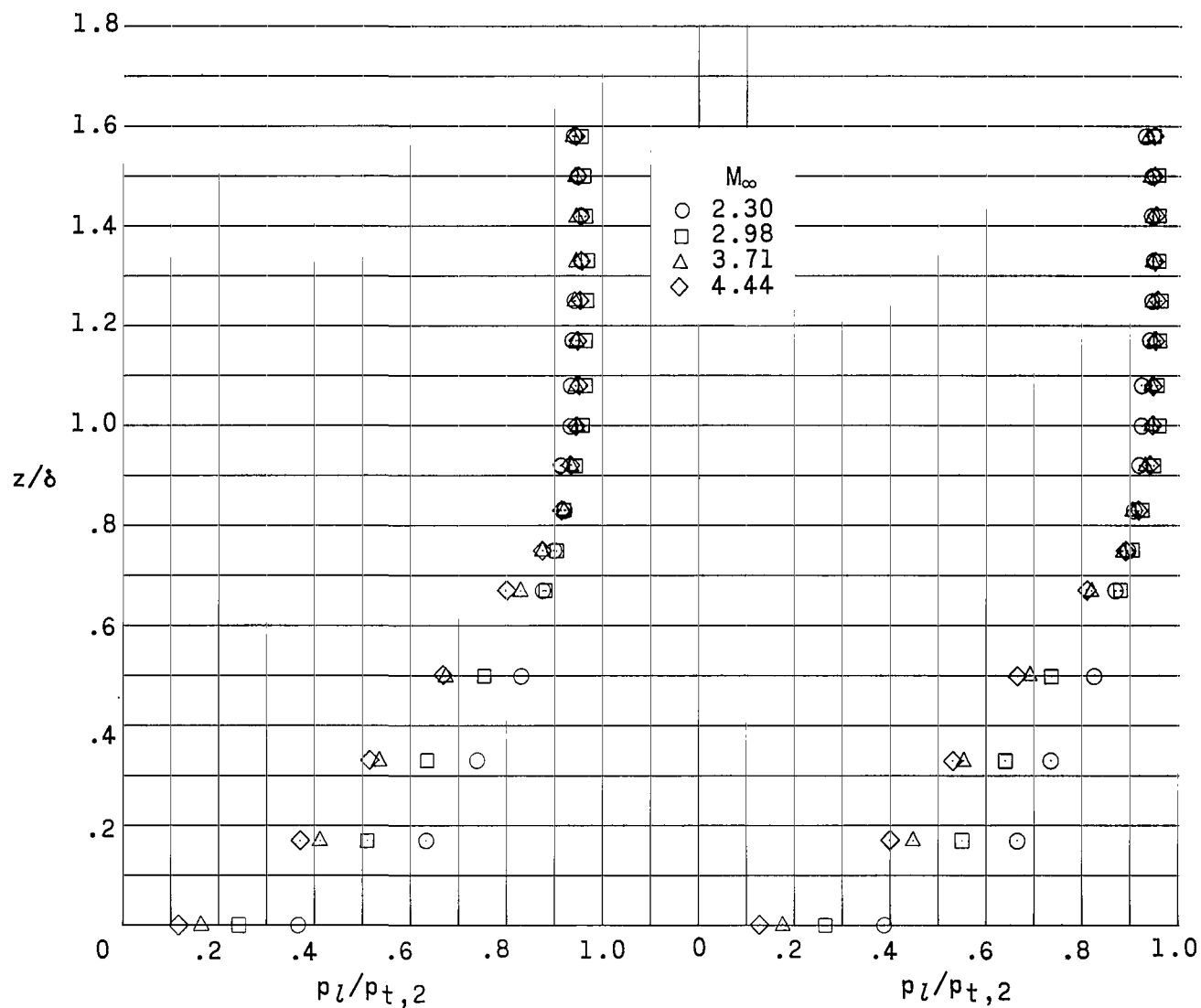


Figure 36.- Effect of Mach number on the model stagnation line pressure distribution. $\Lambda = 12.9^\circ$; $h = 25.40$ cm; $R_\infty \approx 9.8 \times 10^6$.

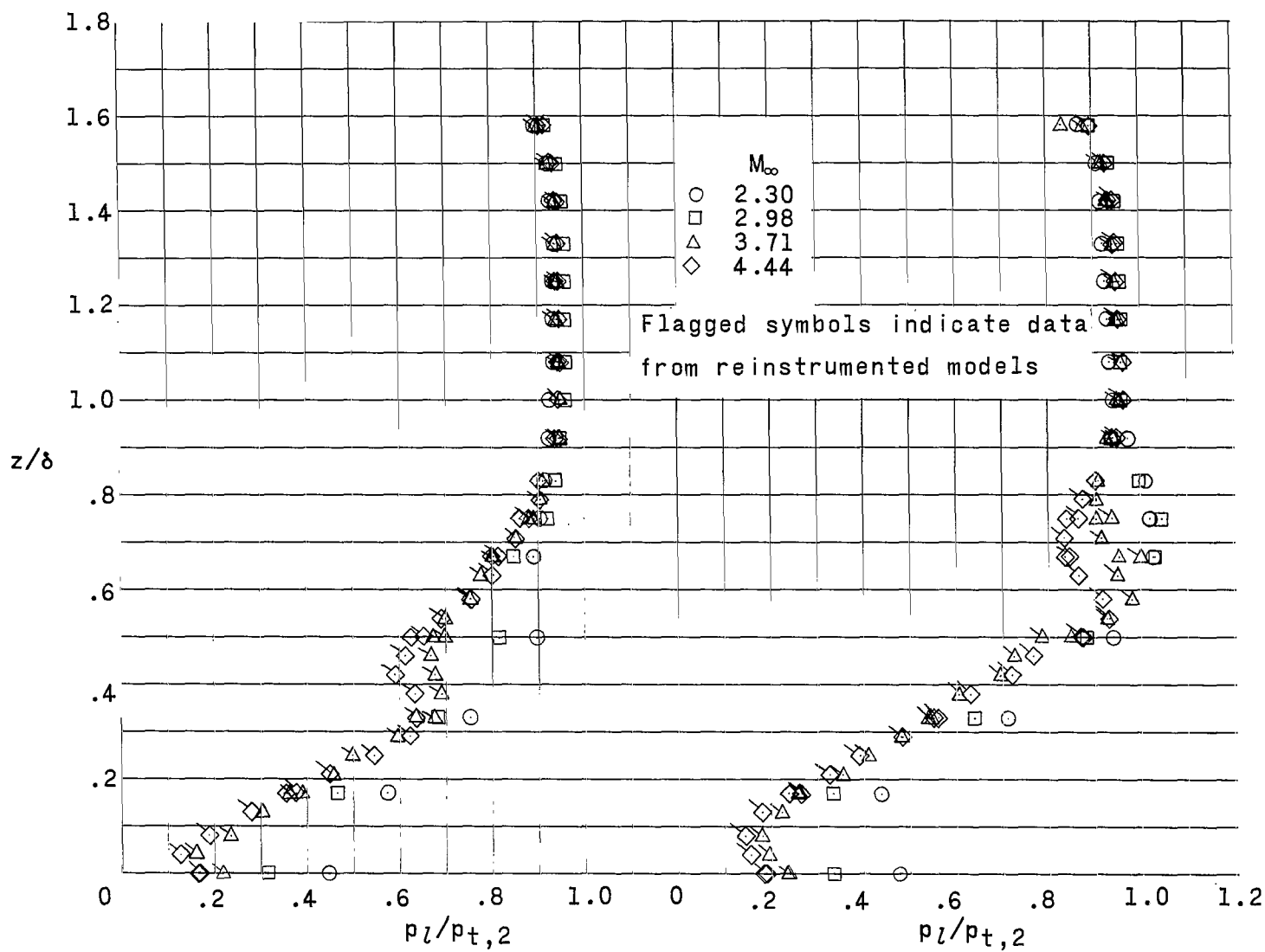


Figure 36.- Concluded.

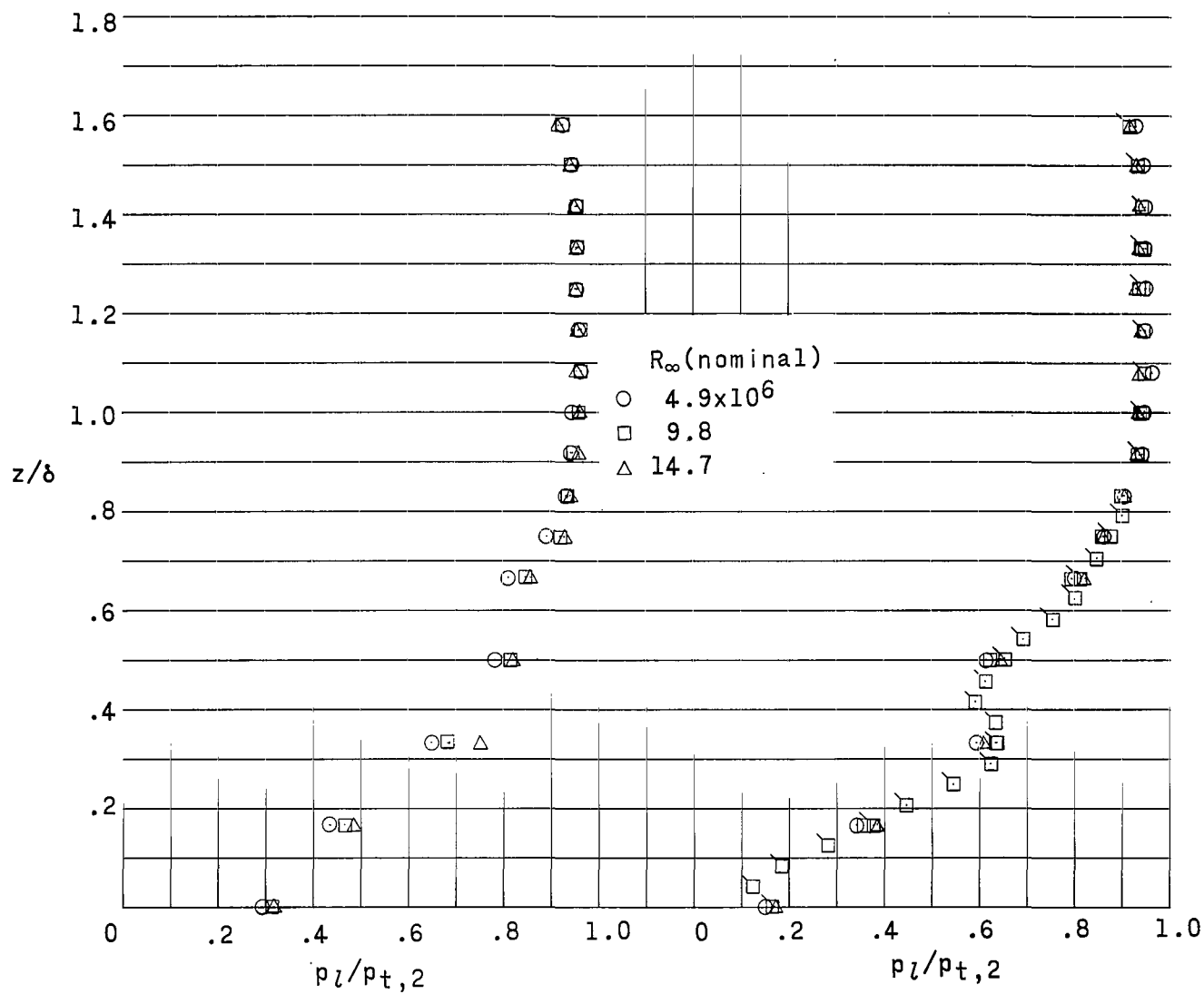
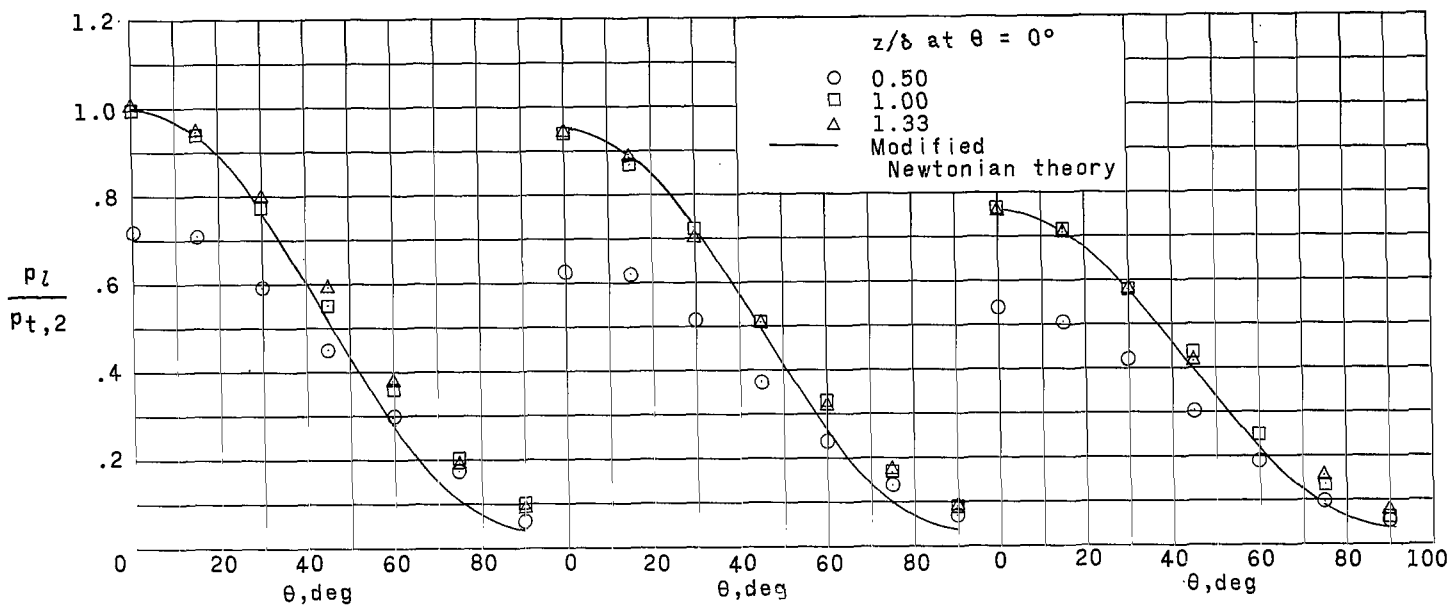
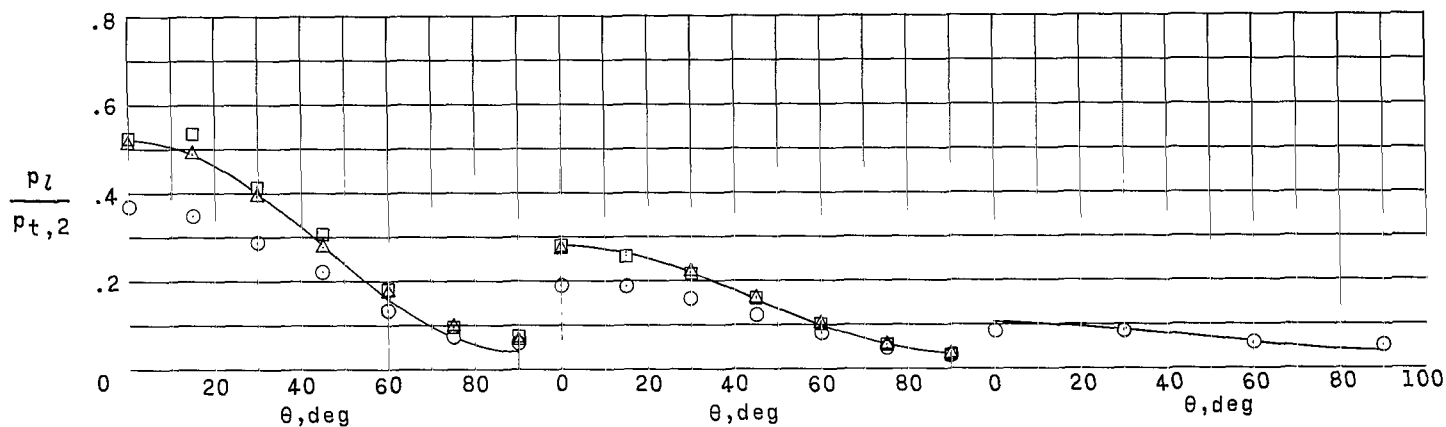
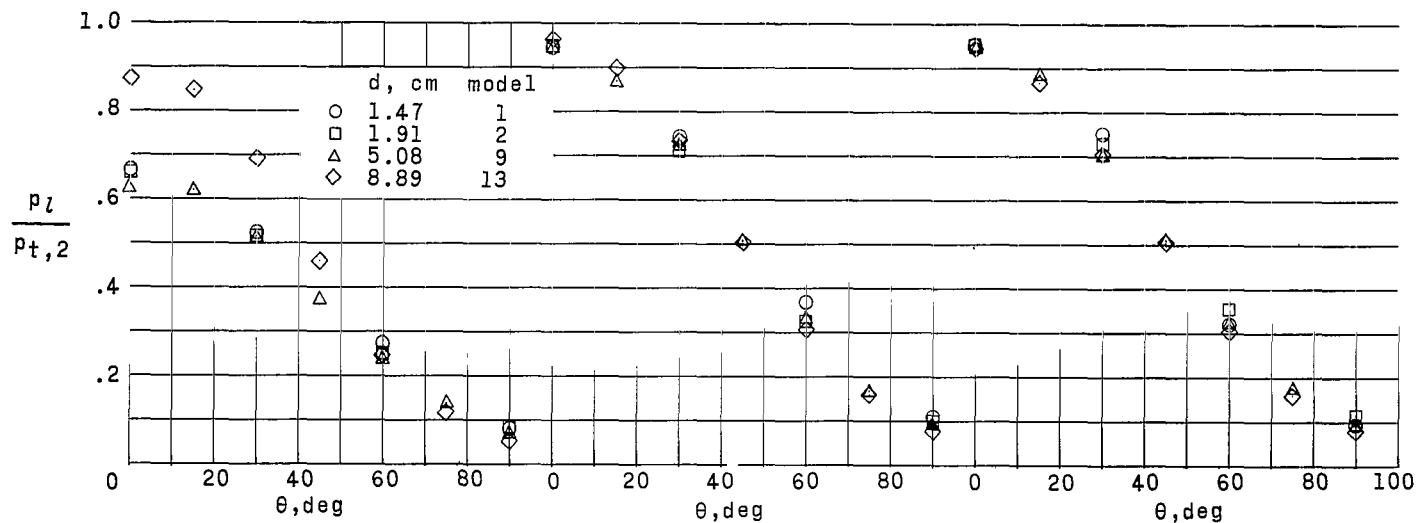


Figure 37.- Effect of Reynolds number on the stagnation line pressure distribution of model 9. $\Lambda = 12.9^\circ$; $d = 5.08$ cm; $h = 25.40$ cm; flagged symbols indicate data from reinstrumented models.

(a) Model 8; $\Lambda = 0^\circ$; $h = 25.40$ cm.(b) Model 9; $\Lambda = 12.9^\circ$; $h = 25.40$ cm.(c) Model 7; $\Lambda = 30^\circ$; $h = 25.40$ cm.(d) Model 10; $\Lambda = 45^\circ$; $h = 25.40$ cm.(e) Model 11; $\Lambda = 60^\circ$; $h = 25.40$ cm.(f) Model 12; $\Lambda = 75^\circ$; $h = 15.24$ cm.Figure 38.- Pressure distributions around the model leading edge for various values of sweep. $d = 5.08$ cm; $M_\infty = 4.44$; $R_\infty \approx 9.8 \times 10^6$.

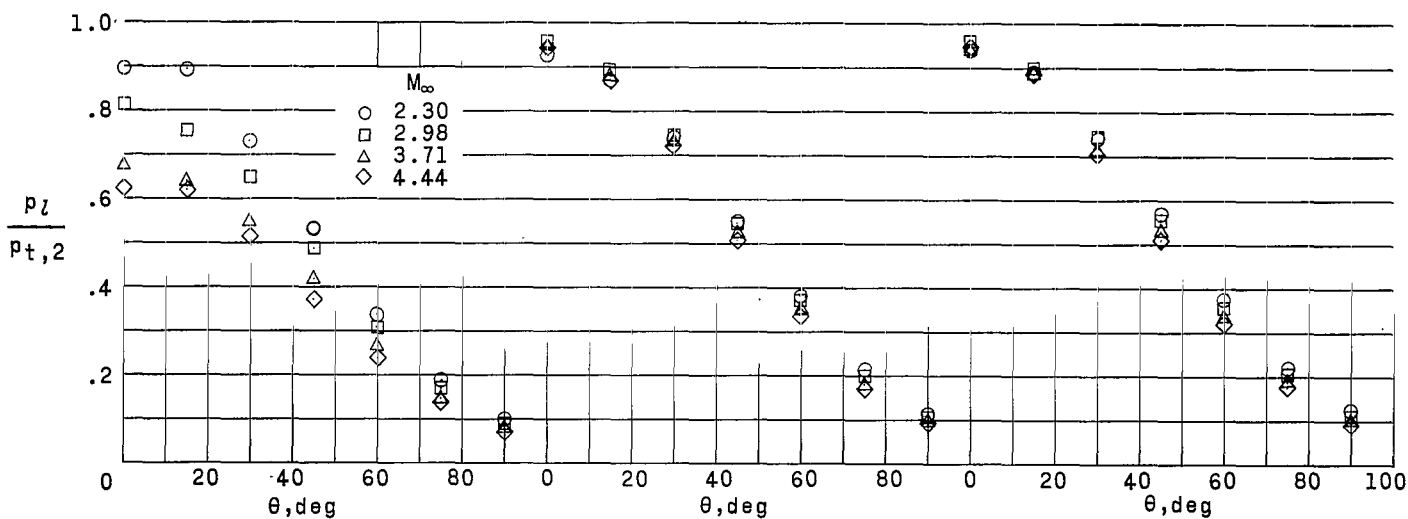


(a) $z/\delta = 0.5$ at $\theta = 0^\circ$.

(b) $z/\delta = 1.00$ at $\theta = 0^\circ$.

(c) $z/\delta = 1.33$ at $\theta = 0^\circ$.

Figure 39.- Effect of diameter on the pressure distribution around the model leading edge. $\Lambda = 12.9^\circ$; $h = 25.40$ cm; $R_\infty \approx 9.8 \times 10^6$; $M_\infty = 4.44$.



(a) $z/\delta = 0.5$ at $\theta = 0^\circ$.

(b) $z/\delta = 1.00$ at $\theta = 0^\circ$.

(c) $z/\delta = 1.33$ at $\theta = 0^\circ$.

Figure 40.- Effect of Mach number on the pressure distribution around the leading edge of model 9. $\Lambda = 12.9^\circ$; $d = 5.08$ cm; $h = 25.40$ cm; $R_\infty \approx 9.8 \times 10^6$.

"The aeronautical and space activities of the United States shall be conducted so as to contribute . . . to the expansion of human knowledge of phenomena in the atmosphere and space. The Administration shall provide for the widest practicable and appropriate dissemination of information concerning its activities and the results thereof."

—NATIONAL AERONAUTICS AND SPACE ACT OF 1958

NASA SCIENTIFIC AND TECHNICAL PUBLICATIONS

TECHNICAL REPORTS: Scientific and technical information considered important, complete, and a lasting contribution to existing knowledge.

TECHNICAL NOTES: Information less broad in scope but nevertheless of importance as a contribution to existing knowledge.

TECHNICAL MEMORANDUMS: Information receiving limited distribution because of preliminary data, security classification, or other reasons.

CONTRACTOR REPORTS: Technical information generated in connection with a NASA contract or grant and released under NASA auspices.

TECHNICAL TRANSLATIONS: Information published in a foreign language considered to merit NASA distribution in English.

TECHNICAL REPRINTS: Information derived from NASA activities and initially published in the form of journal articles.

SPECIAL PUBLICATIONS: Information derived from or of value to NASA activities but not necessarily reporting the results of individual NASA-programmed scientific efforts. Publications include conference proceedings, monographs, data compilations, handbooks, sourcebooks, and special bibliographies.

Details on the availability of these publications may be obtained from:

SCIENTIFIC AND TECHNICAL INFORMATION DIVISION
NATIONAL AERONAUTICS AND SPACE ADMINISTRATION

Washington, D.C. 20546